Utah State University

DigitalCommons@USU

5-2018

Silane Modulation of Protein Conformation and Self-Assembly

Abul Bashar Mohammad Giasuddin
Utah State University

Follow this and additional works at: https://digitalcommons.usu.edu/etd

Part of the Biological Engineering Commons

Recommended Citation

SILANE MODULATION OF PROTEIN CONFORMATION AND SELF-ASSEMBLY

by

Abul Bashar Mohammad Giasuddin

A dissertation submitted in partial fulfillment
of the requirements for the degree

of

DOCTOR OF PHILOSOPHY

in

Biological Engineering

Approved:

_____
David W. Britt, Ph.D.
Major Professor

_____
Jixun Zhan, Ph.D.
Committee Member

_____
Anhong Zhou, Ph.D.
Committee Member

_____
Ling Liu, Ph.D.
Committee Member

_____
Silvana Martini, Ph.D.
Committee Member

_____
Mark R. McLellan, Ph.D.
Vice President for Research and
Dean of the School of Graduate Studies

UTAH STATE UNIVERSITY
Logan, Utah

2018

ABSTRACT

Silane modulation of protein conformation and self-assembly

by

Abul Bashar M. Giasuddin, Doctor of Philosophy

Utah State University, 2018

Major Professor: David W. Britt
Department: Biological Engineering

Proteins may self-assemble and form insoluble amyloid-type fibrils, which are responsible for diseases like Parkinson's, Huntington's, Alzheimer's, spongiform encephalopathy, and cataracts. Amyloid fibrils are comprised of highly ordered β-sheets stabilized by an extensive network of intermolecular hydrogen bonds, hydrophobic surfaces, and favorable packing of side chains. Due to this hierarchical structuring, amyloid fibrils are resistant to degradation and depolymerization. This research investigated the use of hydrophobic silane-based polymeric nanoparticles (NPs) to disrupt fibrillation of a model globular protein, β-lactoglobulin (BLG). After a comprehensive hydrolysis and condensation study of two hydrophobic silanes, 3,3,3-trifluoropropyl trimethoxy silane (3F) and n-propyltrimethoxy silane (nPM), nanoparticulate forms of these silanes were synthesized under mild aqueous conditions and assessed for

antifibrillation activity. The resulting NPs were superhydrophobic, with water contact angles on NP films exceeding 150°, suggesting that the fluoro- and methyl-moieties were accessible on the NP surfaces. Unreacted silanol groups also appeared to be present on the NP surfaces, as determined from negative zeta potential measurements and infrared spectroscopy showing OH vibrational bands. Molecular docking of the 3F monomer with BLG indicated hydrogen bonding of both CF_3 and Si-OH moieties with protein residues, suggesting that an incomplete condensation during NP formation is important for binding protein, leaving residual silanol groups accessible on the NP surface, in proximity to fluoro groups.

Under conditions selected to induce BLG fibrillation, the 3F NPs successfully inhibited fibril formation, resulting in the formation of protein-silane particles rather than self-assembling into fibrils. Infrared spectroscopy indicated that in the presence of 3F, the BLG secondary structure was significantly altered. In contrast, the non-fluorinated nPM NPs failed to inhibit fibrillation under the same conditions, supporting the molecular docking studies.

The fluoro-silane NPs were further investigated as nano-drug delivery systems. Quercetin and curcumin, two natural compounds exhibiting anti-amyloid activity, were successfully loaded into the NPs during the sol-gel synthesis. Rapid and sustained release profiles were observed for both compounds, supporting applications of 3F NPs as both active agents and drug delivery systems. The generality of the 3F protein-conformation

modulating activity was further demonstrated against synthetic spider silk protein, with the goal of tuning the protein secondary structure to enhance silk fiber properties.

An array of analytical tools, including optical density, dynamic light scattering, atomic force microscopy, scanning electron microscopy, infrared spectroscopy, fluorescence spectroscopy, and molecular modeling were employed in these studies to characterize the NPs and assess their mode of interaction with BLG and synthetic spider silk. From this research, the hydrolysis and condensation pathways of trifunctional hydrophobic silane monomers were characterized and optimized, and a new facile one-step and environmentally friendly method for synthesizing superhydrophobic silica NPs was developed. Applications of the resulting NPs in modulating protein secondary structure, inhibiting protein self-assembly, and as carriers for hydrophobic drugs were demonstrated from this research.

(209 pages)

PUBLIC ABSTRACT

Silane modulation of protein conformation and self-assembly

Abul Bashar M. Giasuddin

This research focused on development of nanoparticle-based therapeutics against amyloid fibrils. Amyloid fibrils are associated with various diseases such as Parkinson's, Huntington's, mad cow disease, Alzheimer's, and cataracts. Amyloid fibrils develop when proteins change their shape from a native form to a pathogenic "misfolded" form. The misfolded proteins have the ability to recruit more native proteins into the pathogenic forms, which self-assemble into amyloid fibrils that are hallmarks of the various protein-misfolding diseases listed above. Amyloid fibrils are highly resistant to degradation, which may contribute to the symptoms of amyloid diseases. Synthetic drugs, natural compounds, and antibodies are widely explored for potential to stop pathogenic protein assembly or to promote fibril degradation and clearance, but to date have had little success in relieving symptoms in clinical trials. In this research, I have synthesized fluorine-containing silica nanoparticles (NPs), and tested their fibril-inhibiting activity against amyloid fibrils formed by a non-pathogenic protein, β-lactoglobulin (BLG). These fluoro-silica NPs prevented BLG amyloid formation, whereas non-fluorinated nanoparticle analogs did not inhibit fibrillation under the same reaction conditions. The fluoro-silica NPs interacted with the BLG protein in a manner that prevented the protein

from adopting a form that could self-assemble into fibrils. Additional applications of the

NPs were explored as small-molecule drug-delivery systems; such that multiple

functionalities could be introduced into a single nano-therapeutic.

<div style="text-align: right;">Abul Bashar Mohammad Giasuddin</div>

ACKNOWLEDGMENTS

CONTENTS

LIST OF TABLES

LIST OF FIGURES

ACRONYMS

Word, name, or phrase	Notation
1,1,1,3,3,3-Hexafluoro-2-propanol	HFIP
3-aminopropyltriethoxysilane	APTS
3-glycidoxypropyltrimethoxysilane	GPTS
3,3,3-Trifluoropropyl trimethoxy silane	3F
Analysis of variance	ANOVA
Atomic force Microscopy	AFM
Attenuated total reflectance	ATR
Cetyltrimethylammonium bromide	CTAB
Dynamic light scattering	DLS
Ethanol	ETOH
Fourier transform infrared spectroscopy	FTIR
Hen egg-white lysozyme	HEWL
Hydrodynamic radius	R_h
Hydrolyzed 3F	H3F
Hydrolyzed nPM	HnPM
Hydrophobic silica nanoparticles	HSN
Isoelectric point	IEP
Lysozyme	LYS
Mesoporous silica particles	MSP
n-Isopropylacrylamide	NIPAM
n-Propyltrimethoxy silane	nPM
Nanoparticles	NPs
Nuclear magnetic resonance	NMR
Phosphate-buffered saline	PBS
Recombinant spider silk protein	rSSP
Scanning Electron Microscopy	SEM
Sodium dodecyl sulfate	SDS
Spider silk protein	SSP
Superhydrophobic silica nanoparticles	SHSN
Tetraalkoxysilanes	TAOS

Tetraalkylammoniumhydroxides	TAAOH
Tetraethyl orthosilicate	TEOS
Tetrafluoroethylene	TFE
Thioflavin T	ThT
β-Lactoglobulin	BLG

CHAPTER 1

AMYLOIDOSIS DISEASE, SILANE-INDUCED PROTEIN CONFORMATION

CHANGE AND SELF-ASSEMBLY

1.1 Background and literature

1.1.1 Protein and its folding mechanism

Proteins are among the most complex and diverse bio-macromolecules, comprised of 20 amino acid residues linked into linear chains by peptide bonds. Proteins have four layers of structure, which hierarchically define the protein folding process. The linear sequence of amino acids forms the primary structure of the protein. An extended linear chain, however, is energetically unfavorable, and the polypeptide will explore conformations that reduce the net free energy and solvent exposure. Hydrophobic amino acids sequester to minimize contact with aqueous solvents, and a random coil type structure can be expected as a result. However, the primary structure of a protein pre-determines the types of interactions that will be favored as the chain undergoes random fluctuations, thus directing the folding of the polypeptide and resulting in the formation of secondary structure elements such as α-helices and β-sheets.

The α-helix is a common protein secondary structure motif and is a coiled or spiral conformation in which hydrogen bonds are formed between backbone carbonyl (C=O) and amine groups (N-H) that are separated by a distance of four residues. Backbone hydrogen bonds also stabilize another type of secondary structure in proteins, called the β-sheet. In β-sheet motifs, a planar structure is stabilized as hydrogen bonds are formed at regular intervals between residues as the peptide chain folds upon itself in a

lamellar pattern. The β-sheet is defined by the lamellar folds in the backbone; each fold is termed a β-strand, and neighboring strands are connected laterally by at least two or three backbone hydrogen bonds resulting in a pleated sheet. The β-strand is typically 3 to 10 amino acids long with the backbone arranged in a linear, extended conformation. β-sheets are termed either *parallel* or *anti-parallel*, depending on whether the β-strands are oriented in the same backbone (C to N : C to N) direction, or opposite directions (C to N : N to C). These structures are of key importance in protein-misfolding diseases, where pathogenic protein isoforms that are rich in β-sheets recruit native isoforms by inducing a net transition from α-helix to β-sheet. In these proteins, the β-sheets exhibit a propensity to inter-molecularly self-assemble into fibrils and amyloid plaques. Experimentally, the switch in protein conformation is easily triggered by a number of factors such as heat, low pH, H-bond disrupting solvents, and interactions with surfaces and nanoparticles (NPs). β-sheet assembly is also a key process in formation of non-pathogenic protein macro-structures, such as collagen and spider silk fibers.

While β-sheets are necessary for inter-protein assembly into fibrils, there are many β-sheet-rich proteins that do not assemble into fibrils. This is due in part to the protein tertiary structure, where α-helices and β-sheets are arranged in a stable three-dimensional structure that defines the native state. The tertiary structure of protein involves global interactions arising from hydrogen bonds, ionic bonds, hydrophobic interactions, and disulfide bonds. In contrast to the secondary structural motifs involving

H-bonding between backbone amide groups, these interactions occur between the side (R) groups of the amino acids, holding the secondary structures in defined arrangements that form the tertiary structure. These interactions may be physical bonds, such as H-bonds and salt bridges, or covalent bonds in the case of disulfide bonds between cysteine residues in close proximity.

The final level of protein structure is the quaternary structure, which is the assembly of multiple individual polypeptide or protein chains into a multi-subunit protein. Intermolecular interactions hold the substituent polypeptide or protein chains into a functional geometry, often stabilized by disulfide bonds. Protein quaternary structure is grouped into the two major categories of "fibrous" and "globular". Globular proteins may contain helical, pleated or random chain structures, and are relatively spherical in shape. Some examples of globular proteins are hemoglobin, myoglobin, insulin, and egg albumin. Collagen, silk, and keratin are common examples of fibrous protein structures. Amyloid fibrils are examples of fibrous structures associated with disease. In both native and pathogenic cases, quaternary structure is a supramolecular geometry that emerges from the hierarchical assembly of building blocks following defined rules for assembly.

During protein synthesis, the disordered polypeptide arranges into the ordered native state through the process of protein folding. Most proteins spontaneously fold into a specific conformation, driven by the hydrophobic effect and stabilized through chemical bonds and physical interactions that form secondary, tertiary and quaternary

protein structures. Proteins known as chaperones may also guide the folding of newly synthesized proteins into the correct geometry corresponding to the functional conformation. Chaperones are also involved in the re-folding of proteins following heat shock or other stress.

The correct folding of a protein is essential to function, whether structural, enzymatic, signaling, or transport. The unfolded or denatured state of a protein is considered to be an ensemble of structures ranging from fully disordered random coils, to relatively well-defined molten globule conformations. (1) The molten globule state is distinct from the globular quaternary structure. A schematic of unfolded and folded protein structures is shown in Figure 1-1.

Folded protein

Unfolded protein
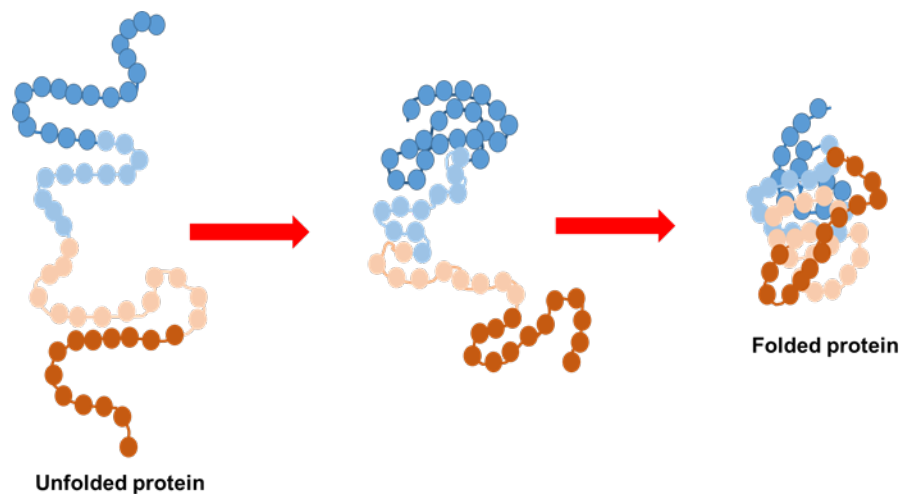
Figure 1-1. Schematic of protein folding. (Adapted from (2))

Generally, a globular protein folds in such a way that it contains a hydrophobic core surrounded by a hydrophilic outer layer. This promotes the formation of a dense, compact structure. The exposure of hydrophobic residues to a polar solvent such as water is energetically unfavorable as it results in water adopting an organized "ice-like" layer or clathrate around these residues. (3) The entropic penalty for these water molecules favors protein folding to sequester hydrophobic residues together in the protein interior, which is free from solvent. This is known as the "hydrophobic interaction", and it is primarily driven by an entropy gain as organized water molecules are liberated from the hydrophobic residues during the folding process. Hydrogen bonds, Van der Waals interactions, and salt bridges stabilize the secondary, tertiary, and quaternary levels of structure that, in concert, stabilize the net structure. In this manner, weak forces act together to contribute toward a stable and functional protein conformation.

Protein folding is reversible, and metastable conformations may also be adopted during folding or unfolding. (4) To spontaneously adopt the folded or native state, a protein folding pathway must be a thermodynamically favorable process. Energy diagrams identify the most stable form or minimum energy condition of a protein. (5) Under physiological conditions, the native or folded state of a protein contains lower free energy compared to the unfolded state. (6) The free energy difference, ΔG, which is defined as $\Delta H-T\Delta S$ (ΔH and ΔS are the enthalpic and the entropic changes, respectively), can be used to explain this phenomenon. To reach a stable folded state, a favorable

enthalpy change arising from numerous interactions (hydrophobic, electrostatic, hydrogen bonding) drives the reaction. This is, however, opposed by the entropy decrease associated with the folded state, because it requires a large number of unstructured conformations to be turned into a single ordered structure to achieve this state. The net entropy change, however, is favorable as entropically unfavorable water clathrates surrounding exposed hydrophobic residues are liberated as disordered bulk water upon folding of the protein.

In this manner, the system overcomes the penalty associated with the polypeptide chain conformational entropy decrease to reach its folded state. The role of the solvent in protein folding and unfolding is important and will be revisited in the discussion of the influence of solvents, such as fluoroalcohols, on protein secondary structure. As proteins vary widely in size, structure, and function, the enthalpy and entropy changes associated with denaturation vary respectively; nevertheless, the free energy changes of most proteins are generally confined to a narrow range (5-15 kcal/mol). (7) The contribution of these individual interactions to the total free energy change can be estimated using highly sensitive calorimetric methods. As these energy values are relatively low, minor changes in solution pH, ionic strength, and temperature can lead to protein destabilization and the adoption of meta-stable conformations such as the molten globule state, as depicted in the energy diagram Figure 1-2.
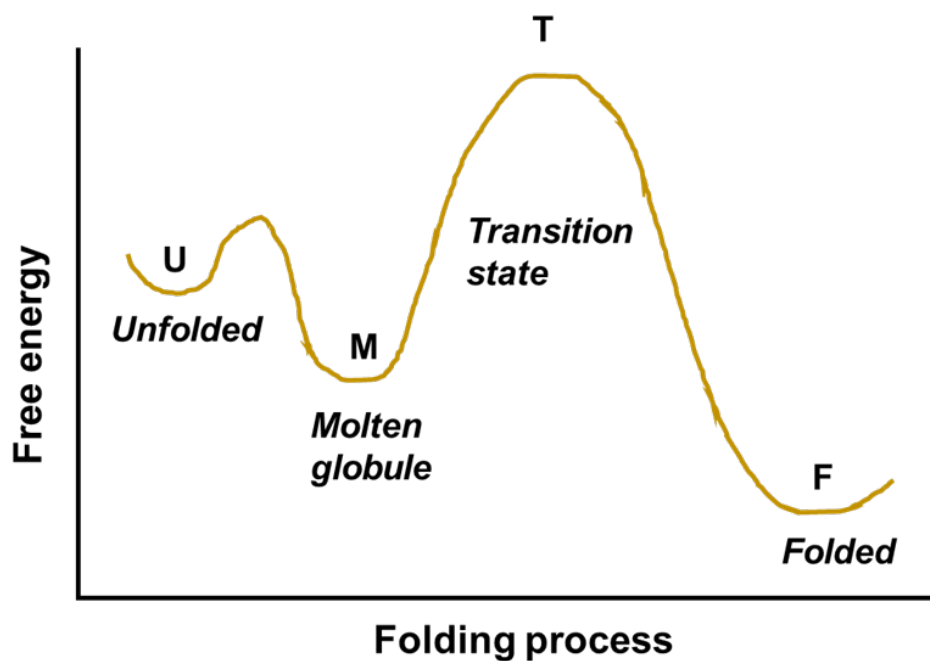
Figure 1-2. Energy diagram of protein folding. (Adapted from (5))

The perturbed structure may further denature, refold, or under certain conditions, self-assemble into supramolecular structures such as amyloid fibrils.

The early view of the protein folding was based on kinetics models, which were derived from simple or multiple exponential time decays of optical properties paralleling changes in protein structures upon initiation of folding. More extensive work was then carried out to identify stable intermediates, corresponding to molten globule states, now known to define the pathways of folding, as depicted in Figure 1-3. The molten globule has most of the secondary structure of the native state and in some cases even native-like positions of the α-helices and β-strands. It is less compact than the native structure, and

the proper packing interactions in the interior of the protein are not formed. Also, loops and other elements of surface structure remain largely unfolded, adopting conformations distinct from the native folded structure.
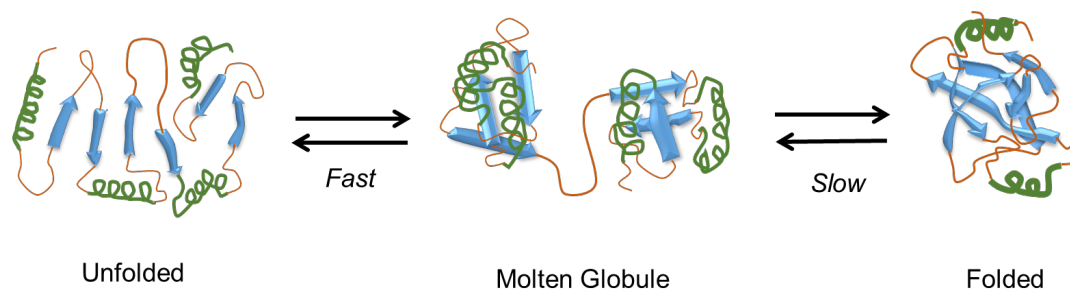
Figure 1-3. Molten globule state of protein.

The molten globule is not viewed as a single structural entity but as an ensemble of related structures that are rapidly inter-converting. It is a major challenge to conceive a single mechanism, which would satisfactorily explain (as well as predict) the folding of all proteins. From empirical studies and computational predictions, a number of models have been developed to describe the pathways and intermediates associated with protein folding, which have led to three classical mechanisms of protein folding that are illustrated in Figure 1-4. (8)
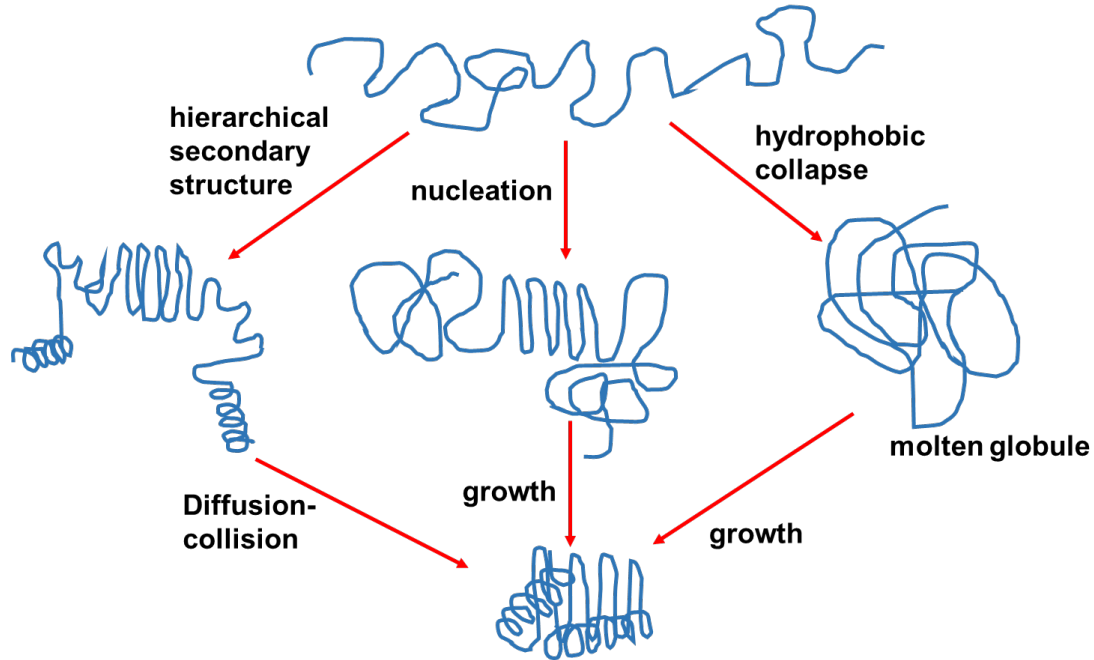
Figure 1-4. Schematic of protein folding mechanism. (Adapted from (8))

Nucleation-growth model: This model proposes the initial formation of a local element of secondary structure from which a tertiary structure propagates rapidly. This pathway ignores the possible transition through any molten globule intermediates, which are often experimentally observed during the protein folding process.

The hydrophobic collapse model: According to this model, during the folding process, hydrophobic amino acids collapse and form a compact structure by excluding water. Unlike the nucleation-growth model, this model describes the formation of molten globule intermediates that arise from the collapse of the hydrophobic amino acids prior to reaching the native conformation. However, a non-specific hydrophobic collapse process

that results in a highly stable intermediate may significantly impede reorganization of the polypeptide into the final native state.

The hierarchical model: This model describes a stepwise process where all of the secondary structural elements such as helices, turns, and sheets are first folded to yield a hierarchy of stabilized secondary structures, which have fewer degrees of spatial freedom as they explore intramolecular interactions that lead to the native folded state of the protein.

1.1.2 Amyloid, self-assembly, and conformational disease

The ability of proteins to fold into a defined and functional conformation is one of the most fundamental processes in biology. However, several diseases arise from the misfolding, or partial unfolding, of proteins, which have implications beyond a mere loss of functionality, as the misfolded proteins may self-assemble and aggregate into a quaternary structure identified by insoluble plaques. In Alzheimer's disease (AD), the amyloid hypothesis links neurodegeneration and diminished cognition to the amyloid plaques comprised of $\alpha\beta_{42}$ proteins. Thus, therapeutics that target plaques have been widely explored, but with limited clinical trial success. Due to these poor clinical trial outcomes of therapeutics designed to clear amyloid from patients, the central hypothesis that symptoms are a direct result of plaque formation is coming under increasing scrutiny. (9) Trials exploring early administration of amyloid inhibitors for patients at risk for AD

may provide additional insight into the relation between amyloid fibrils and disease symptoms.

Specific intermolecular interactions between hydrophobic residues forming structural subunits in partially folded or unfolded intermediates prime the formation of amyloid plaques and fibers, as a loop in the protein chain is converted to a β-strand. (10) For example, in spongiform encephalopathies, cellular prion PrP^c converts to the pathogenic isoform PrP^{sc} with an associated decrease of α-helical content (from 42 % to 30 %) and increase in β-sheet structure (from 3 % to 43 %). (11, 12) The pathogenesis arising from the assembly of β-sheet structures into amyloid is contrasted with the assembly of native proteins rich in β-sheet, such as spider silk proteins where the strength and water solubility of the bio-fiber produced from protein depends on the crystallinity of β-sheet structure. (13) Thus, from a fundamental assessment of protein hierarchical assembly, external agents that promote fibrillation are also of significant interest.

Although certain conditions allow the supramolecular assemblies of β-sheet rich proteins to be reversed, in most cases the aggregation process is irreversible. Genetic defects and mutation can destabilize the native state of the protein and eventually promote the aggregation of the protein. Adverse cellular and physiological factors and post-translational processes also can promote aggregation of protein. (14)

Among the cellular conditions, elevated temperature is a key element in protein aggregation. (7) Heat can disrupt the hydrogen bonds that dictate folding, while changing

the pH of the protein's environment can affect ionic bonds, and reducing agents can cleave any disulfide bonds stabilizing the tertiary and quaternary structures. Oxidative stress has also been shown to contribute to the pathogenesis of many protein aggregation processes. (15) Additional determining factors are ionic strength, chaotropic agents, co-solutes, and the presence or absence of various molecular chaperones.

A wide number of experimental conditions may induce amyloid, and in most instances the misfolded proteins form fibrils that have a commonality of being rich in β-sheet conformations. In-vivo, the organized oligomerization of misfolded protein into β-sheet rich conformations can lead to the production of the characteristic amyloid plaque, which is described as extracellular, fibrillar protein deposits associated with diseases in humans. (16) Clearly not all proteins rich in β-sheet conformations spontaneously self-assemble into supramolecular structures. This level of assembly is generally strictly controlled, as in the case of proteins involved in structural roles, such as collagen fibers. The β-sheet assembly in pathogenic proteins presents a challenging problem that can be addressed by understanding the intermediates, such as the molten globule, involved in the transition from a non-pathogenic isoform to a pathogenic one. Figure 1-5 shows a schematic of amyloid fibril formation that describes fibrillation pathways involving the molten globule intermediate. (17)
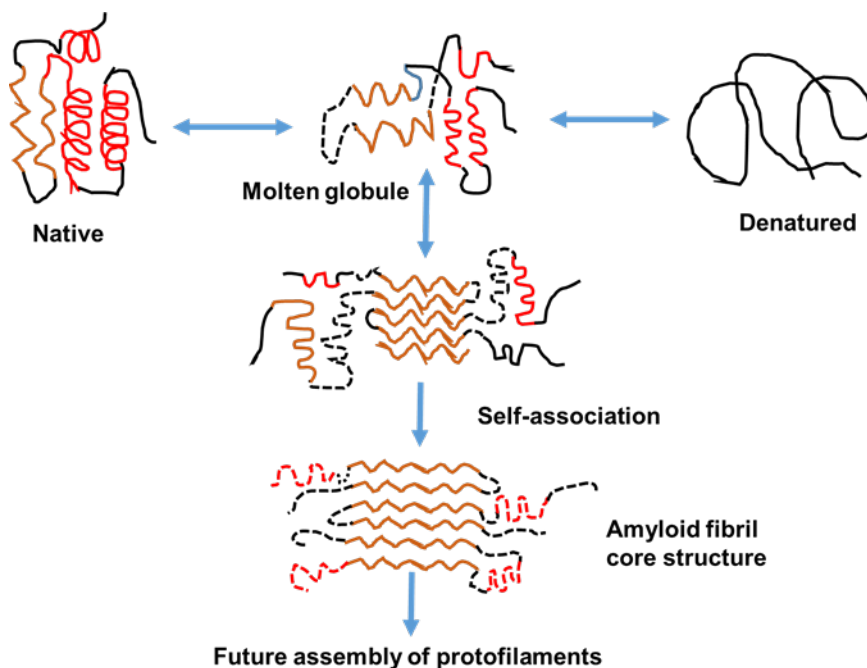
Figure 1-5. Schematic of amyloid fibril formation. (Adapted from (17))

Amyloid-based diseases involve recruitment and self-assembly of proteins into insoluble fibrils and plaques, leading to a variety of pathologies, including Alzheimer's, Parkinson's, cataracts, dialysis-related amyloidosis, and type II diabetes in humans, and spongiform encephalopathy in cattle, sheep, and elk. (18) Figure 1-6 presents a schematic of different amyloidosis diseases and their protein aggregation and misfolding patterns.
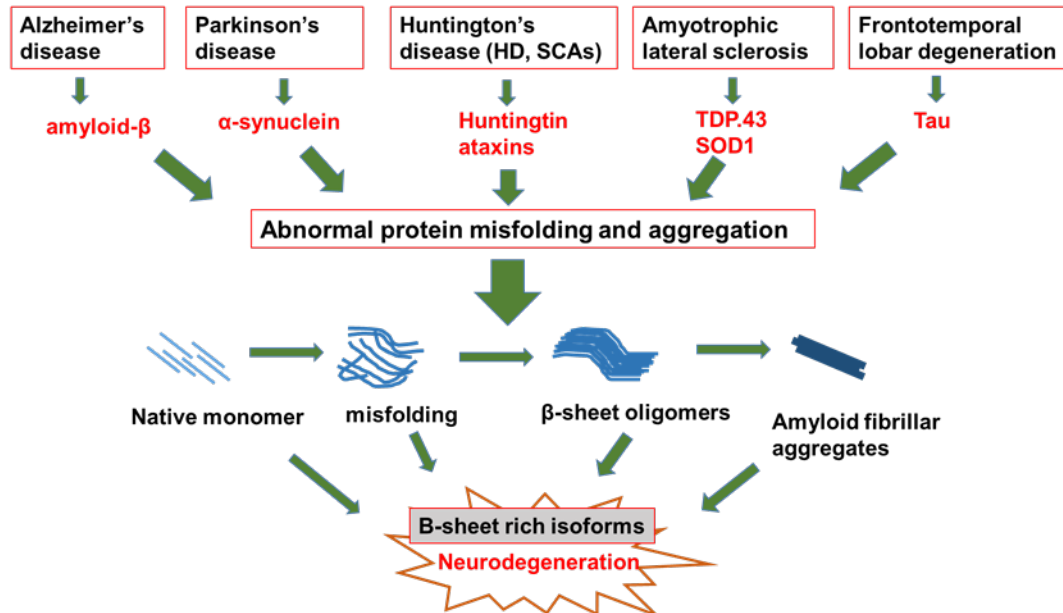
Figure 1-6. Schematic of amyloidosis diseases with the corresponding proteins and their abnormal transformational changes. (Adapted from (18))

1.1.3 Solvent, surface, and nanoparticle-induced protein conformations

Currently no therapeutic is available to prevent or treat amyloidosis diseases. Several therapeutics have shown success in-vitro and in animal models, but have failed to halt disease progression or reduce symptoms in clinical trials (16). Proposed amyloid aggregation or fibrillation inhibitors can be categorized in three groups: 1) protein / peptides, 2) small molecules / colloid, and 3) organic / inorganic NPs. An overview of compounds exhibiting anti-fibrillation activity is compiled in Table 1-1.

Table 1-1. Overview of compounds that exhibit fibril inhibition activities.

Protein type	Fibril inhibitor	References
$\alpha\beta_{13\text{-}28}$	Solanezumab (monoclonal antibody)	19
$BACE_1$	Veruvecestat (beta-secretase inhibitor)	20
HEWL	Myricetin (flavonoid)	21
$A\beta_{1\text{-}42}$	Aducanumab (monoclonal antibody)	22
BLG	Folic acid (B-vitamin)	23
$\alpha\beta_{2M}$	SDS (anionic surfactant)	24
BLG	Au NPs	25
BLG	Fe^{3+}	26
$\alpha\beta_{1\text{-}42}$	Histidine coated Au NPs	27
Human Insulin	Carbon dots	28
$\alpha\beta_{1\text{-}42}$	Tabersonine (terpene indole alkaloid)	29

In many of the studies it has been noted that polymeric and inorganic NPs have been reported to accelerate or promote the protein fibrillation. Fibrillation promoters are listed in Table 1-2.

Table 1-2. Overview of compounds that have been reported to exhibit fibril promoting activities.

Protein type	Fibril promoter	References
HSA	Cu^{2+}	30
$\alpha\beta$ peptide	(PEI-P) conjugates	31
$\alpha\beta_{42}$	TiO_2	32
Human β_2m	NIPAM / BAM NPs	33
Amyloid β	Polystyrene NPs	34

Alcohols have been widely characterized for their roles in inducing protein secondary structures. (35) Alcohol co-solvents are widely used to denature proteins and to stabilize induced secondary structures in peptides. The ability of aliphatic alcohols to denature proteins increases with their effective methylene chain length (i.e. pentanol > butanol > propanol > isopropanol). (36) Among the alcohols, fluoro-substituted alcohols such as TFE (2,2,2-trifluoroethanol) and HFIP (hexafluoro-2-propanol) have been found to be more effective co-solvents for evoking structural changes in protein and peptides compared to aliphatic-alcohols. (37) HFIP and TFE partially denature protein native structures and induce α-helices in numerous proteins and their fragments. This secondary structure selective activity leads to their investigation as solvents for transforming proteins into molten globule intermediates, stabilizing induced intermediates, or dissolving aggregates. As discussed earlier, the thermodynamics of protein folding and stability hinges on the properties of the water solvent. Disruption of organized "ice-like" water on a protein surface by a co-solvent, such as a fluoroalcohol, increases the water entropy, but also will reduce the enthalpy associated with these surface bound water molecules. This in turn may promote the adoption of new secondary structural motifs, in particular, α-helices. Table 1-3 presents those proteins whose conformations have been investigated against fluoro-alcohols.

Table 1-3. Overview of fluoro-alcohol-protein studies investigating secondary structure changes in proteins and peptides. (Adapted from Y. Peng Ph.D. thesis, Utah State University, 2011. (53))

Protein type	Inducer fluoro-alcohol	References
Silk model peptide	HFIP	38
Octapeptide	HFIP, TFE	39
Alzheimer's beta-peptide	HFIP	40
N^α-acylated heptapeptide amide	HFIP	41
Islet amyloid polypeptide	HFIP, TFE	42
22-residue peptide of macroglobulin	HFIP, TFE	43
Papain	HFIP, TFE	44
Succinylated Con A	HFIP, TFE	45
Pea lectin	HFIP	46
β-lactoglobulin	HFIP, TFE	47
Tau protein	TFE	48
Bovine serum albumin	TFE	49
Barstar	HFIP, TFE	50
Cytochrome c	HFIP	51
Acylphosphatase	TFE	52

HFIP, and TFE at higher concentrations, are able to dissolve protein aggregates. However, at lower concentrations these fluoro-alcohols may actually promote β-sheet structures and form amyloid fibril in several models. (54) It has been reported that α-chymotrypsin, an all β-sheet protein, aggregated into amyloid-like structures in the presence of TFE, where the maximal amount of fibrillar aggregation was formed at 35 % (v/v) TFE. (55) As the TFE concentration was increased to above 40 % (v/v), the aggregation propensity was reduced. When HFIP was used, β-sheet conformations were

maintained in 3 % or below HFIP-water mixtures (v/v), while the formation of α-helices was observed when HFIP content was increased over 20 %. (54, 56)

During the interaction with a polypeptide, HFIP and TFE can each simultaneously act as a proton donor and acceptor due to the presence of highly electronegative fluorine and alcohol groups. The fluorine acts as a hydrogen acceptor and forms H-bonds with the proton donor groups on the protein. The fluoro-alcohol hydroxyl group is a very strong proton donor and selectively binds with the protein backbone carbonyl group. (37) Through this fluoro-alcohol-peptide interaction, the solvent exposure of the backbone amide is reduced and intra-polypeptide hydrogen bonding of the amide group is favored, which increases the helical propensities.

The hydrophobic properties of alcohols are very influential to their activities on polypeptide structures. The longer chain aliphatic *n*-alcohols, such as propanol or butanol are much more potent than methanol. (37) The presence of $-CF_3$ in HFIP and TFE makes both the fluoro-alcohols highly efficient inducers on the structural transitions of protein. The presence of hydrocarbon groups and multiple fluorine atoms increases the hydrophobicity of the fluoro-alcohol, which can play a vital role in denaturing protein secondary structures and inducing the formation of helical structures. (37, 58) HFIP and TFE both have a high tendency to self-aggregate to form micelle-like assemblies in aqueous solution. Aggregation of HFIP and TFE in water produce clusters with a Stokes

radius of about 24 Å, and 6 Å, respectively and these clusters further reduce solvent polarity around the protein. (59-62)

The electronegativity of fluorine in alcohols increases the polarization of the terminal hydroxyl groups, which consequently leads to enhanced H-bond donor activity (62, 63), resulting in the enhanced effects of HFIP and TFE, as compared to analogous organic alcohols. Thus, the fluoro-alcohols interact with protein both as hydrogen bond donors and acceptors, whose bindings are further stabilized by hydrophobic interactions. HFIP has a higher inducing capacity on protein secondary structures compared to TFE, due to its stronger hydrophobicity – greater H-donor and H-acceptor activities associated with incorporation of multiple F atoms – which also promotes the higher tendency of HFIP to aggregate into nano-structures that may form multi-valent interactions with proteins.

Although HFIP and TFE are model compounds for inducing protein structural transitions, both are highly corrosive, toxic, and flammable. These properties preclude their use as therapeutic agents for amyloid diseases, as well as limit bioprocessing applications to promote protein-based fiber assembly. Alternatively, polymerizable silanes analogous to HFIP and TFE could be applied to produce therapeutic polymers, NPs, or protein-silane hybrids that exhibit favorable properties associated with HFIP and TFE, without the negative aspects. For example, hydrophobic alkoxysilanes are widely used as coupling agents to modify surfaces, forming porous gels, and to construct NPs.

Protein encapsulation in porous sol-gel glasses has been widely used in heterogeneous bio-catalysis applications and in the development of solid state optical and electrochemical biosensors. (64-64) Sol-gel glass encapsulation has been demonstrated to retain the activity of a wide variety of enzymes.

Recently, hydrolyzable hydrophobic fluoro-silanes analogous to TFE or HFIP have been studied for their protein structure inducing ability at acidic pH. (53, 67) These studies showed that 3,3,3-trifluoropropyl trimethoxy silane (3F), which is analogous in structure to TFE and nPM (n-propyltrimethoxy silane) – a non-fluorinated analog of 3F – are both strong protein secondary structure inducers that are also polymerizable. Circular dichroism analysis of protein structure in the presence of hydrolyzed 3F and nPM (H3F, HnPM, respectively) demonstrated the conversion of β-sheet structures into α-helices. (67) These findings lead to the central hypothesis of this research.

1.1.4 Hypothesis

Polymeric nanoparticles (NPs) of hydrophobic alkoxy- and fluoro- silanes induce defined changes in the secondary structures of protein, which depending on the NP concentrations and surface properties, can be used to inhibit or promote protein fibrillation in aqueous media.

1.2 Objectives

Building on earlier works (53, 67), which demonstrated that at low pH, hydrolyzed nPM and 3F induced β-sheet to α-helices, this work aims to identify underlying mechanisms and expand applicability. The key objectives of this research are to:

1. Understand the hydrolysis and condensation behavior of 3F and nPM in aqueous solution catalyzed at select acidic pH values.

2. Characterize the physical and chemical properties of the polymeric particles as they develop during the condensation process.

3. Determine whether fluorinated and methylated polymeric nanoparticles, like their hydrolyzed precursor monomers, inhibit amyloid fibrillation of a model protein.

4. Assess the types of conformational changes in the model protein during the inhibition process.

5. Model the interaction between polymeric NPs and protein using Molecular Docking models of protein with hydrolyzed silane monomers.

6. Develop superhydrophobic NPs from the hydrolyzed 3F and nPM, following conventional condensation methods, and determine the efficiency of these NPs as amyloid inhibitor and as carriers for hydrophobic drug molecules.

7. Determine the modulating ability of 3F and nPM against the secondary structures of spider silk proteins.

1.3 Research methods overview

The experimental approach to addressing the objectives and answering the central hypothesis is outlined in the research flow chart in Figure 1-7. A variety of complementary techniques and instruments are applied to address the hypothesis and questions associated with hydrophobic silane assembly to form nanoparticles that modify protein secondary structures, and propensity to assembly into supramolecular architectures, such as fibrils and sheets.
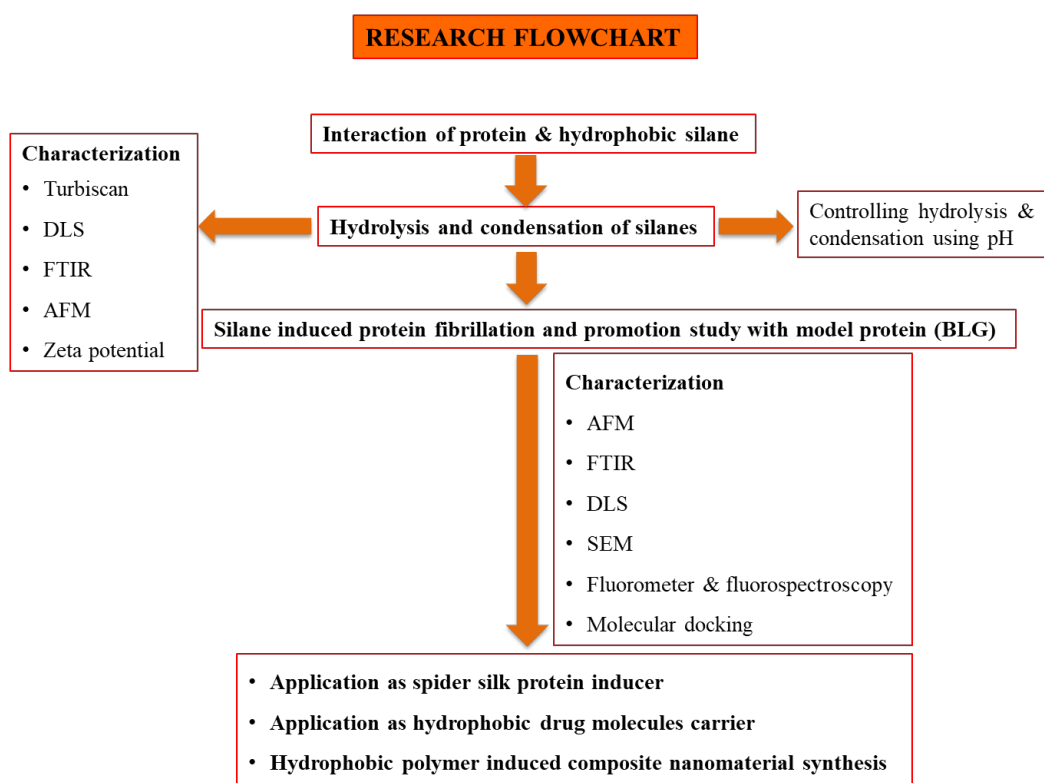
Figure 1-7. Research flow chart illustrating the major directions and methods.

1.4 References

1. Uversky, V. N. *Protein Sci.* **2002***, 11*, 739.

2. Teodoro, M.; Phillips, G. N. Jr.; Kavraki, L. E. *The Journal of Computational Biology* **2003**, *10*, 617.

3. Creighton, T. E., Proteins: structures and molecular properties, Second edition, 1992.

4. Whitford, D., Proteins: structure and function, First edition, 2005.

5. Branden, C.; Tooze, J., Introduction to protein structure, Second edition. 2000.

6. Dobson, C. M.; Sali, A.; Karplus, M. *Angew. Chem. Int. Ed. Eng.* **1998**, *37*, 868.

7. Joseph, P.; Zbilut, J. P., Thomas Scheibel, Protein folding-misfolding: some current concepts of protein chemistry, First edition, 2006.

8. Fersht, A. R.; Daggett, V. *Cell* **2002**, *108*, 573.

9. Yiannopoulou, K. G.; Papageorgiou, S. G. *Ther. Adv. Neurol. Disord.* 2013, *6*, 19.

10. Fink, A. L. *Folding Des.* **1998**, *3*, R9−R23.

11. Zhang, H.; Kaneko, K.; Nguyen, J. T.; Livshits, T. L.; Baldwin, M. A.; Cohen, F. E.; James, T. L.; Prusiner, S. B. *J. Mol. Biol.* **1995**, *250*, 514.

12. Pan, K. M.; Baldwin, M.; Nguyen, J.; Gasset, M.; Serban, A.; Groth, D.; Mehlhorn, I.; Huang, Z.; Fletterick, R. J.; Cohen, F. E.; Prusiner, S. B. *Proc. Natl. Acad. Sci. U.S.A.* **1993**, *90*, 10962.

13. Romer, L.; Scheibel, T. *Prion* **2008**, *2*, 154.

14. Gaestel, M. Molecular chaperones in health and disease, First edition, 2006.

15. Chen, X; Guo, C; Kong, J. *Neural. Regen. Res*. **2012**, *15*, 376.

16. Knowles, T. P. J.; Vendruscolo, C. M. *Nat. Rev. Mol. Cell Biol.* **2014**, *15*, 384

17. Selkoe, D. J. *Nature* **2003**, *426*, 900.

18. Di Carlo, M.; Picone, P.; Carrotta, R.; Giacomazza, D.; Biagio, S. Alzheimer's disease and type 2 diabetes: different pathologies and same features. In: Zimering M, editor. Topics in the prevention, treatment and complications of type 2 diabetes. Croatia: INTECH Open Access Publisher; 2011.

19. Imbimbo, B. P.; Ottonello, S.; Frisardi, V.; Solfrizzi, V.; Greco, A.; Seripa, D.; Pilotto, A.; Panza, F. *Expert Rev. Clin. Immunol.* **2012**, *8*, 135.

20. Kennedy, M. E.; Stamford, A. W.; Chen, X.; Cox, K.; Cumming, J. N.; Dockendorf, M. F.; Egan, M.; Ereshefsky, L.; Hodgson, R. A.; Hyde, L. A.; Jhee, S.; Kleijn, H. J.; Kuvelkar, R.; Li, W.; Mattson, B. A.; Mei, H.; Palcza, J.; Scott, J. D.; Tanen, M.; Troyer, M. D.; Tseng, J. L.; Stone, J. A.; Parker, E. M.; Forman, M. S. *Sci. Transl. Med.* **2016**, *8*, 1.

21. J. He, Y.; Wang, A. K.; Chang, L.; Xu, N.; Wang, X.; Chong, H.; Li, B.; Zhang, G. W.; Song, Y. *J. Agric. Food Chem.* **2014**, *62*, 9442.

22. Sevigny, J.; Chiao, P.; Bussiere, T.; Weinreb, P.; Williams, L.; Maier, M.; Dunstan, R.; Salloway, S.; Chen, T.; Ling, Y.; O'Gorman, J.; Qian, F.; Arastu, M.; Li, M.; Chollate, S.; Brennan, M. S.; Quinyero-Monzon, O.; Scannevin, R. H.; Arnold, H. M.; Engber, T.; Rhodes, K.; Ferrero, J.; Hang, Y.; Mikulskis, A.; Grimm, J.; Hock, C.; Nitch, R. M.; Sandrock, A. *Nature* **2016**, *537*, 50.

23. Ma, B.; Wen, Li, Zhu, X.; Liu, G.; Zhang, F.; Wu,F.; Jiang, X.; Xie, J. *European Journal of Biomedical Research* **2017**, *1*, 22

24. Khan, J. M.; Qadeer, A.; Chaturvedi, S. K.; Ahmad, E.; Rehman, S. A.; Gourinath, S.; Khan, R. H. *PLoS One* **2012**, *7*, e29694.

25. Sardar, S.; Pal S.; Maity, S.; Chakraborty, J.; Halder, U. C. *Int. J. Biol. Macromol.* **2014**, *69*, 137.

26. Guzzi, R.; Rizzuti, B.; Labate, C.; Zappone, B.; De Santo, M. P. *Biomacromolecules* **2015***, 16*, 1794.

27. Palmal, S.; Jana, N. R.; Jana, N. R. *J. Phys. Chem.* **2014***, 118*, 21630

28. Li, S.; Wang, L.; Chusuei, C. C.; Suarez, V. M.; Blackwelder, P. L.; Micic, M.; Orbulescu, J.; Leblanc, R. M. *Chem. Mater.* **2015**, *27*, 1764

29. Kai, T.; Zhang, L.; Wang, X.; Jing, A.; Zhao, B.; Yu, X.; Zheng, J.; Zhou, F. *ACS Chem. Neurosci.* **2015**, *6*, 879.

30. Zappone,B.; De Santo, M. P.; Labate, C.; Guzzi, R. *Soft Matter* **2013**, *9*, 2412.

31. Zhu, L.; Song, Y.; Cheng, P. N.; Moore, J. S. *J. Am. Chem. Soc.* **2015**, *137*, 8062.

32. Wu, W. H.; Sun, X.; Yu, Y. P.; Hu, J.; Zhao, L.; Liu, Q.; Zhao, Y. F.; Li, Y. M. *Biochem. Biophys. Res. Commun.* **2008**, *373*, 315.

33. Linse, S.; Cabaleiro-Lago, C.; Xue, W.; Lynch, I.; Lindman, S.; Thulin, E.; Radford, S. E.; Dawson, K. A. *Proc. Natl. Acad. Sci. U.S.A.* **2007**, *104*, 8691.

34. Cabaleiro-Lago, C.; Quinlan-Pluck F.; Lynch, I.; Dawson, K.; Linse, S. *ACS Chem. Neurosci.* **2010**, *1*, 279.

35. Dwyer, D. S.; Bradley, R. J. *Cell Mol. Life Sci.* **2000**, *57* (2), 265.

36. Bull, H. B.; Breese, K. *Biopolymers* **1978**, *17* (9), 2121.

37. Buck, M. *Q. Rev. Biophys.* **1998**, *31* (3), 297.

38. Suzuki, Y.; Gerig, J. T.; Asakura, T. *Macromolecules* **2010**, *43*, 2364.

39. Maekawa, H.; Toniolo, C.; Moretto, A.; Broxterman, Q. B.; Ge, N. H. *J. Phys. Chem. B* **2006**, *110* (12), 5834.

40. Nichols, M. R.; Moss, M. A.; Reed, D. K.; Cratic-McDaniei, S.; Hoh, J. H.; Rosenberry, T. L. *J. Biol. Chem.* **2005**, *280* (4), 2471.

41. Crisma, M.; Saviano, M.; Moretto, A.; Broxterman, Q. B.; Kaptein, B.; Toniolo, C. *J. Am. Chem. Soc.* **2007**, *129* (50), 15471.

42. Higham, C. E.; Jaikaran, E.; Fraser, P. E., Gross, M.; Clark, A. *FEBS Lett.* **2000**, *470* (1), 55.

43. Yamaguchi, K.; Naiki, H.; Goto, Y. *J. Mol. Biol.* **2006**, *363* (1), 279.

44. Naeem, A.; Khan, K. A.; Khan, R. H. *Arch. Biochem. Biophys.* **2004**, 432 (1), 79.

45. Fatima, S.; Ahmad, B.; Khan, R. H. *Arch. Biochem. Biophys.* **2006**, 454 (2), 170.

46. Naseem, F; Khan, R. H. *Biochimica Et Biophysica Acta-General Subjects* **2005**, *1723* (1-3), 192.

47. Hirota, N.; Mizuno, K.; Goto, Y. *Protein Sci.* **1997**, *6*, 416.

48. Kunjithapatham, R.; Oliva, F. Y.; Doshi, U.; Perez, M.; Avila, J.; Munoz, V. *Biochemistry* **2005**, *44* (1), 149.

49. Sen, P; Ahmad, B; Rabbani, G; Khan, R. H. *Int. J. Biol. Macromol* **2010**, *46* (2), 250.

50. Sekhar, A.; Udgaonkar, J. B. *Biochemistry* **2011**, *50*, 805.

51. Konno, T.; Iwashita, J.; Nagayama, K. *Protein Sci.* **2000**, *9* (3), 564.

52. Chiti, F.; Webster, P; Taddei, N; Clark, A.; Stefani, M.; Ramponi, G.; Dobson, C. M. *Proc. Natl. Acad. Sci. USA* **1999**, *96* (7), 3590.

53. Peng Y. (Thesis: Utah State University, **2011**)

54. Khan, M. V.; Rabbani, G.; Ahmad, E.; Khan, R. H. *Int. J. Biol. Macromol.* **2014**, *70*, 606.

55. Yamaguchi, K.; Naiki, H.; Goto, Y. *J. Mol. Biol.* **2006**, *363* (1), 279.

56. Vieira, E. P.; Hermel, H.; Mohwald, H. *Biochim. Biophys. Acta* **2003**, *1645*, 6.

57. Dyer, R. B.; Maness, S. J.; Franzen, S.; Fesinmeyer, R. M.; Olsen, K. A.; Andersen, N. H. *Biochemistry* **2005**, *44* (30), 10406.

58. Rajan, R.; Balaram, P. *Int. J. Pept. Protein Res.* **1996**, *48* (4), 328.

59. Gast, K.; Siemer, A.; Zirwer, D.; Damaschun, G. *Eur. Biophys. J.* **2001**, *30* (4), 273.

60. Berkessel, A.; Adrio, J. A.; Huettenhain, D.; Neudorfl, J. M. *J. Am. Chem. Soc.* **2006**, *128* (26), 8421.

61. Munoz, M. A.; Galan, M.; Carmona, C.; Balon, M. *Chem. Phys. Lett.* **2005**, *401* (1-3), 109.

62. Hong, D. P.; Hoshino, M.; Kuboi, R.; Goto, Y. *J. Am. Chem. Soc.* **1999**, *121* (37), 8427

63. Kuprin, S.; Graslund, A.; Ehrenberg, A.; Koch, M. H. J. *Biophys. Res. Commun.* **1995**, *217* (3), 1151.

64. Bhatia, R. B.; Brinker, C. J. *Chem. Mater.* **2000**, *12*, 2434.

65. Dave, B. C.; Dunn, B.; Valentine, J. S.; Zink, J. I. *Anal. Chem.* **1994**, *66*, 1120.

66. Eggers, D.K.; Calabretta, P. J.; Chancellor, M. C.; Torres, C.; Abel, Jr. G.R.; Neihaus, C., Birtwhistle, N. J.; Khouderchah, N. M.; Zemede, G. H. *J. Funct. Biomater.* **2012**, *3*, 514.

67. Peng, Y.; Turner, N. W.; Britt D.W. *Colloids Surface B* **2014**, *119*, 6.

CHAPTER 2

HYDROLYSIS AND CONDENSATION OF HYDROPHOBIC SILANES IN

AQUEOUS SOLUTION

2.1 Abstract

The hydrolysis and condensation pathways of 3,3,3-trifluoropropyl trimethoxy

silane (3F) and n-propyltrimethoxy silane (nPM) were investigated over an acidic pH

range, to identify conditions yielding stable hydrolyzed silane monomers to be tested for

protein conformation-inducing activity, as both hydrolyzed monomer and when

condensed into nanoparticles (NPs). The reaction kinetics were assessed through turbidity

measurements and dynamic light scattering (DLS) in aqueous solutions at pH 1.7, 2.0,

2.5, and 3.0. Prior to hydrolysis, 3F and nPM are insoluble in water and form a lens at the

bottom of the aqueous solution for 3F, and on the top of the solution for nPM. As the

silanes underwent hydrolysis, they became soluble in the aqueous phase at a rate that

increased with decreasing pH, with the fluorine-based silane (3F) exhibiting slower rates

compared to the non-fluorinated structural analog (nPM). DLS analysis revealed that at

pH 1.7 and 25°C, NP growth from the hydrolyzed nPM and 3F silane precursors at 0.4 M

was detected at 80 min and 175 min, respectively, and rapid growth / aggregation resulted

in NPs >1 μm after 160 min for nPM, and 375 min for 3F. AFM analysis of these NPs

confirmed the NP sizes observed in the DLS study. ATR-FTIR was employed to monitor

the chemical composition during the hydrolysis and condensation, as vibration bands for Si-OH and Si-O-Si bonds appeared, respectively. Zeta potential characterization revealed that at pH 1.7 and 3.0, both nPM and 3F polymeric NPs had negative surface charges. The negative surface charges on the NPs were attributed to the presence of surface accessible Si-OH groups, despite an overall hydrophobic character, as measured by water contact angle. The presence of hydrophobic and silanol moieties implies an amphipathic surface character on these NPs, which, based on prior analyses of silane monomer interactions with proteins, make these NPs potential candidates against protein conformational diseases.

2.2 Introduction

Functional di- and tri-alkoxysilanes (e.g. silanes with two and three reactive leaving groups, respectively) are used for various applications such as adhesion promoters and cross-linkers between a polymer matrix and inorganic solids, as resin precursors, as agents to modify surface properties, and to form porous matrices to capture and encapsulate biological molecules. (1) Alkoxysilanes react slowly, compared to the corresponding chlorosilanes, and are preferred over chlorosilanes for the reactions involving biological molecules, because they liberate organoalcohols, compared to the hydrochloric acid released by chlorosilanes during hydrolysis. The hydrolysis and condensation reaction rates of alkoxysilane decrease with the bulkiness of the alkoxy-

leaving group. Methoxy and ethoxy moieties are the two most common leaving groups, and during the hydrolysis, they are liberated as methanol and ethanol, respectively. The hydrophobicity of these groups render the silane insoluble in aqueous solution, unless a polar functional group is also present; the n-propyl chain of nPM and tri-fluoro moieties of 3F prevent solubilization of these monomers until hydrolysis begins. Alkoxysilane undergoes serial hydrolysis of the alkoxy leaving groups, rendering the silane reactive through the resulting silanol (Si-OH) functionalities. Silanol reactivity enables silanes to be anchored to oxidized surfaces, as well as other silanes bearing alkoxy or hydroxyl groups. Silicon is tetravalent, thus a tri-alkoxysilane contains an additional moiety, R', which may impart functionality to the silane, such as ability to interact with an organic matrix or influence biological molecule binding by modifying the surface energy and hence the interfacial adhesion behavior. This R' moiety can have a range of functionalities, such as epoxy, acrylate, amino, fluoro etc., as well as simple alkyl or aryl groups. A confluent layer of silanes anchored to an oxidized surface may dramatically change the interfacial energy, depending on the R' group chemistry. For fluoro and alkyl-silane coatings, the R' moieties render the surface hydrophobic.

While hydrolyzed silanes readily condense to form silanol (Si-O-Si) bonds with free hydroxyl groups on material surfaces, biomolecules such as proteins, and with other hydrolyzed silanes; they also readily form physical bonds, such as acid-base interactions, hydrogen bonds, dipole-dipole interactions, and van der Waals interactions. (2) Tri-

alkoxy silanes with their R' moiety having hydrophobic functionality can also interact through hydrophobic interactions, which, in the case of alkyl chains, imparts a strong amphiphilic character to the silanes that drives silane self-assembly on surfaces. The hydrolyzed silane monomer is generally regarded as an intermediate to forming a condensed silane product, in the form of a thin film, nanoparticle, or matrix. However, for certain silanes, the hydrolyzed monomer is of interest as a biologically active small molecule. For trifunctional silanes where the R' group is a short chain alkyl- or fluoro-group, the resulting hydrolyzed silane monomer has been shown to interact with proteins and induce conformational changes that exceed the conformation-inducing activities of organo- and fluoro-alcohols. (3) The general applications of tri-alkoxysilane depend on the hydrolysis of the $\equiv$SiOR' groups to produce silanols, which ultimately condense to siloxanes and polysiloxanes. However, partially hydrolyzed and partially condensed tri-alkoxysilanes containing silanols and organosiloxanols can exhibit unique properties to be applied as therapeutics, due to their polymeric nanoparticulate nature. (4)

Most studies on the hydrolysis and condensation kinetics of alkoxysilanes were performed in either organic or organic and aqueous mixed solvents. (5-15) The general reaction steps in the hydrolysis and condensation of tri-alkoxysilanes can be written as:

$$R'Si(OR)_3 + nH_2O \longrightarrow R'Si(OR)_{3-n}(OH)_n + nROH \qquad \text{Hydrolysis}$$

$$R'Si\text{-}OR + HO\text{-}SiR' \longrightarrow R'Si\text{-}O\text{-}SiR' + ROH \qquad \text{Condensation}$$

$$R'Si\text{-}OH + HO\text{-}SiR' \longrightarrow R'Si\text{-}O\text{-}SiR' + H_2O \qquad \text{Condensation}$$
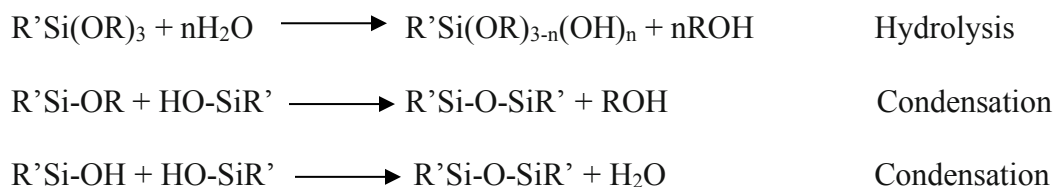
For the effective biological applications of hydrolyzed or partially condensed silanes, the hydrolysis and condensation must be performed in aqueous, biologically relevant solutions. Moreover, for the biological applications of these silane compounds, a nontoxic solvent is essential. The key factors on which this hydrolysis and condensation process in aqueous solution depends are pH, type of R' functionality, size and type of alkoxy group, catalyst, and the concentration of the silanes in the solutions. (6) Two types of catalysts are used for the hydrolysis and condensation of alkoxysilanes, namely acid and base, with distinct pathways and kinetics observed for each. Of particular relevance to NP formation, the condensation process is favored in basic solutions.
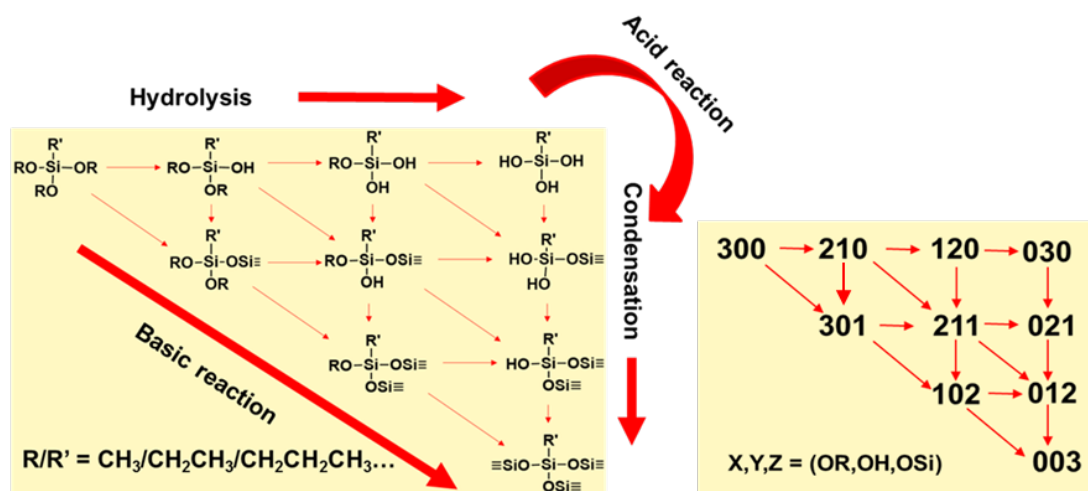
Figure 2-1. Schematic of the reaction scheme of hydrolysis and condensation kinetics of tri-alkoxysilanes at acidic and basic conditions in aqueous media, along with a numerical reaction scheme. (Adapted from (7))

Figure 2-1 is a schematic of the hydrolysis and condensation pathways as they occur in either acidic or basic solutions, along with a numerical representation of the reaction scheme. For acidic pH, hydrolysis is favored over condensation, while in basic pH, condensation occurs more readily than hydrolysis. Acid catalysis favors hydrolysis that follows a sequential displacement of $-O-CH_3$ with $-OH$; and when all three $-O-CH_3$ are replaced with $-OH$, the silane is in a fully hydrolyzed state, which can be achieved before condensation begins.

A previous study from our lab showed that hydrolyzed 3F and nPM could highly induce the secondary structures of model proteins, with the three silanols playing a major role in this conformation-inducing activity through strong H-bond donor activity. (16) It is intuitive that as more silanols are present, greater hydrogen bonding is possible, and stronger biomolecular interactions are likely. Thus, for silane-induction of protein conformation, it is desirable to maintain at least a partially hydrolyzed state and thus employ an acid catalyst.

Although several studies have been published on the hydrolysis and condensation kinetics of tri-alkoxysilanes in aqueous or aqueous-organic mixed solutions, there are no reports available on the evolution of the polymeric particles generated during the condensation of tri-alkoxysilanes following the hydrolysis step in acidic aqueous solution. It is very important to have a clear understanding of the evolution of the size of the polymeric particles during the condensation of the tri-alkoxysilanes, especially when

particles are to be used in biomolecular applications. Linear condensation products from tri-alkoxy silanes will contain silanol functionalities that are stable after condensation is complete, providing H-bond donor functionality to these polymer chains as well as NPs that result from these chains.

Various techniques and analytical tools have been used to investigate silane hydrolysis and condensation kinetics such as NMR, FTIR, Raman spectroscopy, chromatography, mass spectroscopy, and X-ray scattering. (17-33) Of these methods, ^{29}Si NMR spectroscopy has been found to be a powerful tool to follow evolution of intermediates and final products, because this spectroscopy can differentiate silicon atoms attached to different chemical groups. The limitation of this instrument is the low gyromagnetic ratio and long relaxation time, which is unsuitable for studying some rapid hydrolysis reactions in real time, like hydrolysis and condensation of di and tri-alkoxysilanes at lower pH. In situ Attenuated Total Reflectance-Fourier Transform Infrared (ATR-FTIR) spectroscopy was successfully used in quantitative analyses of hydrolysis and condensation of TEOS at lower pH, where spectra measured at different time periods showed that TEOS was first converted into ethanol and $Si(OH)_4$ and then precipitated as amorphous SiO_2. (34) Riegel et al. used Fourier Transform Raman spectra with laser excitation in the near IR during base-catalyzed sol-gel reaction of GPTS (3-glycidoxypropyltrimethoxysilane) and APTS (3-aminopropyltriethoxysilane) where Raman bands of the tri-methoxysilyl and epoxy moieties were used to monitor the kinetic

behavior of the hydrolysis and the ring cleavage as a function of temperature. (25) Pelster et al. used electrospray mass spectrometry to observe pre-nucleation reactions of silicates from an aqueous solution containing TAAOH (tetraalkylammoniumhydroxides) and TAOS (tetraalkoxysilanes). Their study showed the evolution of different silicate species occurring during the condensation process. Their time-resolved measurements were done in a stepwise hydrolysis, and subsequent condensation of silicate monomers via oligomers to form larger units. (30)

All of the above-mentioned techniques were used only to identify the hydrolyzed and condensed products, and not the evolution of condensation product size, morphology, and surface characteristics. DLS is commonly used to measure the hydrodynamic size of organic and inorganic nanoparticulates in solution. (35) Turbiscan is an advanced optical absorbance / transmission technique widely used in the food industries. Turbiscan is operated based on the turbidity in the solution caused by scattered light from foams, emulsions, or particles. (36)

Here, we have reported the hydrolysis and condensation kinetics of two hydrophobic alkyl- tri-alkoxy and fluoro- tri-alkoxy silanes in aqueous solution analyzed by DLS and Turbiscan. Evolution of the polymeric NPs during the condensation was quantitatively analyzed by DLS, and resulting particle charge and morphologies assessed using zeta potential and AFM, respectively. FTIR was employed to identify chemical groups present on the NP products.

2.3 Experimental Section

Source of chemicals

Double Distilled Deionized (DI) water was collected from Barnstead^{TM}

MegaPure^{TM} Glass Still (Thermo Scientific); Hydrochloric Acid (HCl) 1.0 N was

purchased from Ricca Chemical Company (Arlington, TX); 3,3,3-trifluoropropyl

trimethoxy silane (3F, > 95 % purity, MW= 218.3, d = 1.14 g/ml), and n-

propyltrimethoxy silane (nPM, > 95 % purity, MW= 164.3, d = 0.94 g/ml) was purchased

from Gelest, Inc. (Morrisville, PA); and Potassium Chloride (KCl) was purchased from

Thermo Fisher Scientific, NJ.

Monitoring reaction time through silane phase

Four different 0.4 M solutions were prepared for both nPM and 3F at pH 1.7, 2.0,

2.5, and 3.0 using 20 mM, 10 mM, 5 mM, and 1mM HCl solution respectively. The

hydrolysis and condensation were monitored using a Nikon COOLPIX P510 camera.

Turbiscan Analysis

Hydrolysis and condensation behavior of nPM (0.4 M) and 3F (0.4 M) at pH 1.7,

2.0, 3.0, and 4.0 were followed by measuring the transmissivity of light (850 nm) through

the samples using a Turbiscan instrument (Turbiscan Classic, MA200, L'Union, France),

and data were analyzed using Turbisoft 1.2.1. All solutions were prepared as described

above, and the pH 4.0 solution was 0.1 mM HCl. All solutions were placed in the

Turbiscan tubes to a height of 35±0.5 mm, and transmissivity was measured as a function

of time. Transmissivity was measured throughout the height of the solution in the tubes

for 12 to 96 h, and measurements were taken at 2 to 22 min intervals, depending on the

pH of the solutions, which influenced reaction rates. Data were plotted using Sigma Plot.

Dynamic Light Scattering (DLS) analysis

Evolution of polymeric NPs during nPM and 3F hydrolysis and condensation

were analyzed by DLS (DynaPro NanoStar, Wyatt Technology Corporation, Santa

Barbara, CA), with a 658 nm laser. Measurements were taken using a quartz cuvette (JC-

426, 1 µl) with 0.7 ml of nPM (0.1 M) and 3F (0.1 M) solution at pH 1.7 and 3.0. The

data was recorded as an average of ten five-second acquisitions. Hydrodynamic radius

(R_h) of polymeric NPs were obtained using Dynamic software (version 7.0.3, Wyatt

Technology Corporation, Santa Barbara, CA) where the Stokes-Einstein equation is

applied to convert the intensity auto-correlation into the particle sizes.

Atomic Force Microscopy (AFM)

AFM images were taken using a Nanoscope III Bioscope (Digital Instrument,

Inc.) in tapping mode. 100 µl samples at pH 1.7 were drop-cast on freshly cleaved mica

surfaces, allowed to sit for several minutes, and then gently washed with DI water, and

air-dried. AFM cantilevers were purchased from TED Pella Inc., CA (BS-Tap 300AL-G-

50). The tip has radius of curvature <10 nm, length 125 µm, width 30 µm, and thickness

4 µm employed with a 40 N/m force constant. Images were collected at different size

scales, scan angles, and scan rate from 1 to 2 Hz.

Fourier Transformed Infrared Spectroscopy (FTIR)

Both nPM (0.4 M) and 3F (0.4 M) solutions were prepared at pH 1.7, as described before. FTIR readings were taken using a Varian 660-IR platform with a horizontal single reflection Pike Technologies MIRacle attenuated total reflectance (ATR) unit, fitted with a ZnSe crystal. 100 µl samples of nPM or 3F were dropped on the platform for taking the readings. A method was constructed and used with Resolution Pro Version 5.1.0.822 for both nPM and 3F samples. Spectra were taken after averaging 20 scans over the range of 600 to 2000 cm^{-1}, with a resolution of 1 cm^{-1}. Prior to each reading, a blank background was acquired with the appropriate samples.

Zeta potential

Zeta potential was measured with a ZetaPlus zeta meter (Brookhaven Instruments Corporation, Holtsville, NY). 100 µl aliquots of 3F or nPM solutions at defined reaction times were added to 1 ml KCl (1 mM) in the instrument cuvette. The KCl solution was prepared at pH 1.7 and 3.0 to match the pH of the nPM and 3F solutions.

2.4 Result and Discussion

Visual observation of the hydrolysis and condensation kinetic process can give a clear idea of how and when each of the steps occur at different pH for both nPM and 3F. Figure 2-2 shows the images of the hydrolysis and condensation process of (a) nPM and (b) 3F at four different pH 1.7, 2.0, 2.5, and 3.0 over time. Since the density of nPM

(0.932 g/mL) is lower than the water, prior to hydrolysis nPM floats on the top of the water as a concave shaped lens in all the reaction tubes, irrespective of the investigated pH.
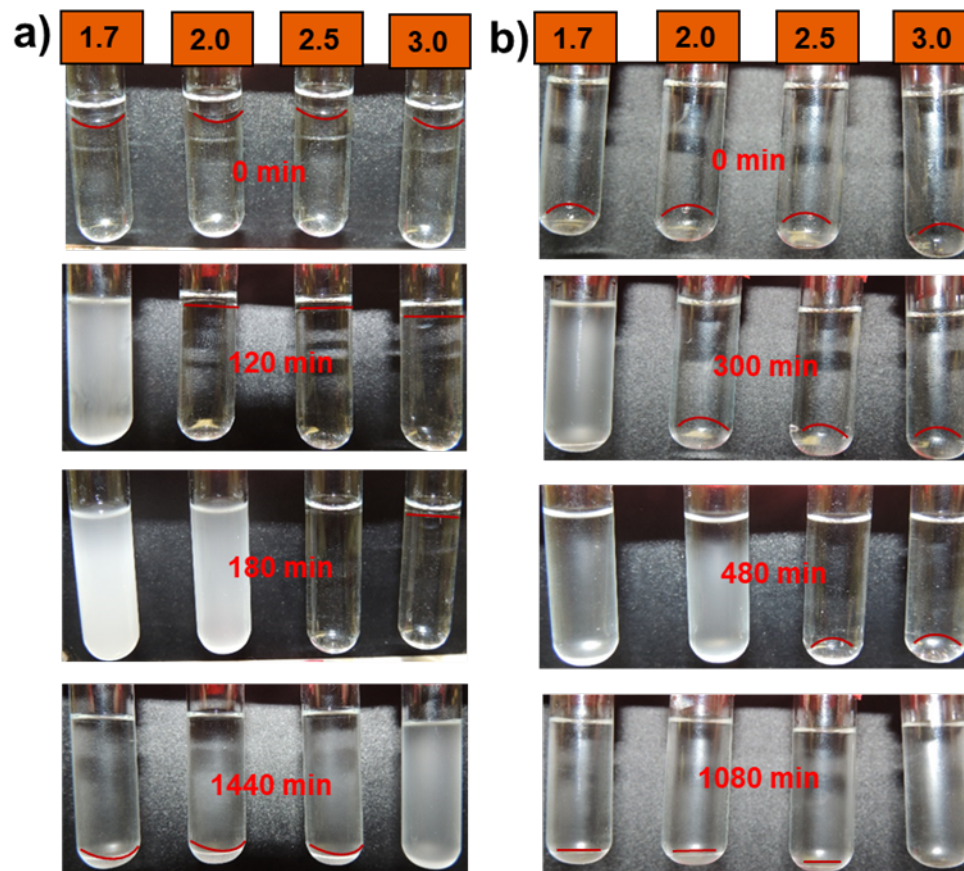
Figure 2-2. Visual observation of the hydrolysis and condensation kinetics of (a) nPM (0.4 M) and (b) 3F (0.4 M) as influenced by pH. The solution pH values are 1.7, 2.0, 2.5, and 3.0 from left to right for the tubes in each image, with the images taken at the indicated times following initiation of the reaction. The red lines highlight the boundary of the unhydrolyzed nPM or 3F with the solutions; in the last panels the red lines indicate condensation products that have settled out of solution.

As seen in Figure 2-2, after 120±10 min at pH 1.7, the nPM reaction tube solution is turbid, indicating condensation product formation. At higher pH values, hydrolysis is not yet complete, but it has progressed significantly by 120 min, which can be observed as depletion of the nPM layers at the top of the solutions. After 180±20 min, the nPM reaction at pH 2.0 was in a condensation state, while at pH 2.5 the nPM lens had disappeared, but the bulk solution was not yet turbid, indicating a hydrolyzed state. At this same time, the pH 3.0 solution was still in a partially hydrolyzed state. After 1440±200 min at pH 1.7, 2.0, and 2.5, condensed particles have settled at the bottom of the reaction tubes; whereas condensation has barely started for nPM at pH 3.0.

A similar pH-dependent pattern of hydrolysis and condensation can be observed for 3F (Figure 2-2 (b)). However, in contrast to the nPM, the 3F hydrolysis and condensation reactions are slower than the corresponding pH values for nPM. 3F is denser than water and formed a convex lens on the bottom of the reaction tube. After 300±50 min, condensation started in the pH 1.7 reaction tube. At higher pH values condensation was not observed, but the volumes of the 3F lenses decreased due to ongoing hydrolysis. After 480±40 min, the reaction at pH 2.0 began to form condensation products, whereas reactions at pH 2.5 and 3.0 were still in the hydrolysis state. After 1080±60 min, the reaction tube at pH 3.0 turned into a condensation state, and at other pH values, condensed polymeric particles started to settle, forming what appeared to be a gel at the bottom of the reaction tubes.

A more quantitative assessment of the hydrolysis and condensation process was attained using Turbiscan to measure the transmissivity of light through the reaction solutions at defined heights (e.g. at the top of the tube for nPM, and the bottom for 3F). Figure 2-3 shows the turbidity-based hydrolysis kinetics of nPM obtained by Turbiscan. These data were taken from the very top of the solution in the tube where unhydrolyzed nPM, which is less dense than water, was suspended as a lens. These Turbiscan-analyzed data clearly showed the hydrolyzed and condensation periods at pH 1.7, 2.0, 3.0, and 4.0. At pH 1.7, the transmissivity was 100 % after 40±5 min, compared to 0 % at the beginning, which means that all the nPM was hydrolyzed at this time. This transmissivity immediately started to reduce, reaching 2±0.5 % after 80±5 min.
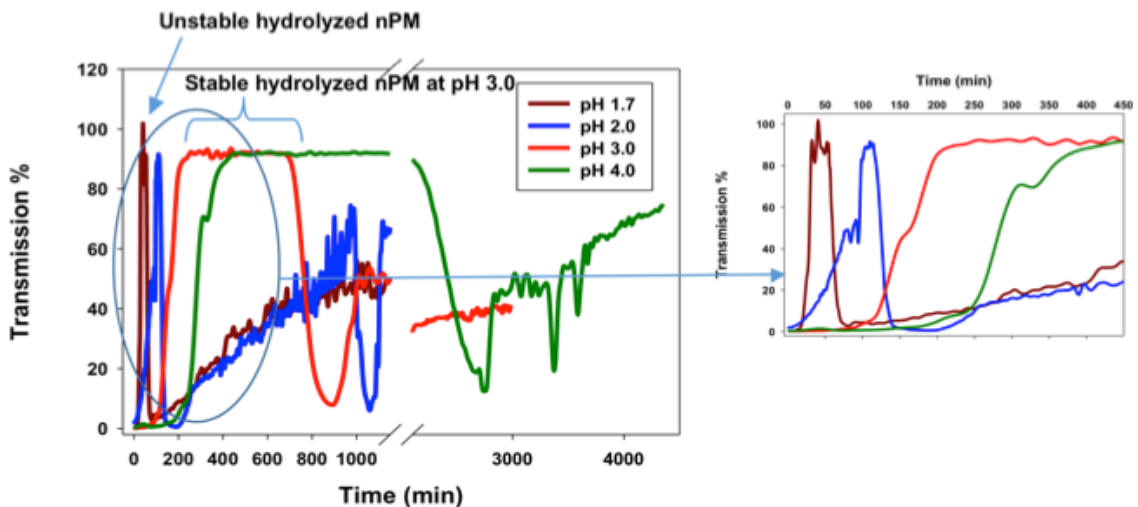
Figure 2-3. Hydrolysis and condensation kinetics of nPM based on transmissivity, using Turbiscan-analyzed data at pH 1.7, 2.0, 3.0, and 4.0.

Transmissivity started to increase by as much as 50±5 % after 900±50 min, as some of the condensed particles possibly started to drop from the solution. Similarly, for pH 2.0, transmissivity was 2±0.5 % at the beginning, and it increased as the hydrolysis was initiated, reaching 90±5 % after 105±5 min; and it remained at this value for 10±1 min, indicating that the hydrolysis products remained stable. Initiating of condensation was indicated as the transmissivity dropped, and reached 1 % after 160±10 min, after which it started to increase again, likely indicating that some particles started to separate from the solution and reached 50±4 % after 850±40 min. At pH 3.0, transmissivity increased from 0 % to 90±2 % after 240±20 min, as hydrolysis reached completion. This optimum, fully hydrolyzed state remained stable for 460±30 min, at which time condensation started. Within 180±20 min, turbidity became highest, as transmissivity turned to 7±1 % after 885±100 min. After this, transmissivity started to increase and turned to 40 % at 2700±100 min, as particles started to separate and settle at the bottom. At pH 4.0, transmissivity increased from 0 % to 90±2 % in 440±40 min, and this hydrolyzed state remained stable for 1650±50 min, before condensation started, as indicated by a reduction in transmissivity. The transmissivity reached a minimum of 12±2 % after 2750±200 min, after which it started to increase again; and decrease of transmissivity fluctuated as hydrolysis and condensation continued.

Figure 2-4 shows the 3F Turbiscan hydrolysis and condensation data at pH 1.7, 2.0, 3.0, and 4.0. For 3F transmitted light was measured at the bottom of the tube, where the dense unhydrolyzed 3F formed a lens. Transmissivity was 5±1 % at the beginning, but after 30±5 min it increased to 65±5 %, as the lens decreased in size via solubilization of hydrolyzed 3F. A fully hydrolyzed state was not attained at pH 1.7 for 3F, as indicated by the subsequent reduction in transmissivity. Unlike in the case of nPM, maximum transmissivity was never more than 65±5 % for 3F at pH 1.7, indicating that under these conditions 3F was unable to be fully hydrolyzed by the time condensation began. The transmissivity continued to decrease for 120±8 min, reaching 30±3 %, after which it increased again and plateaued at 60±5 % after 225 min, due to scattering from the NPs.
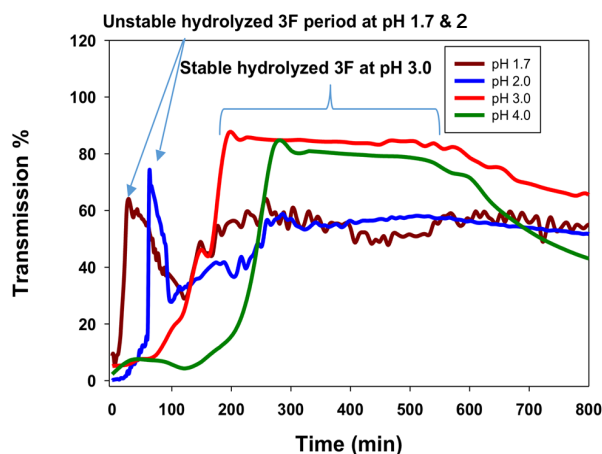
Figure 2-4. Hydrolysis and condensation kinetics of 3F, based on transmissivity, using Turbiscan-analyzed data at pH 1.7, 2.0, 3.0, and 4.0.

As seen in Figure 2-4, at pH 2.0, the 3F hydrolysis and condensation kinetics followed a similar trend as 3F at pH 1.7, with the noted difference of a slower initial hydrolysis rate at the slightly higher pH.

At pH 3.0, the hydrolysis rate further slowed, requiring 195 ± 15 min to reach a transmissivity of 87 ± 5 % that was stable for 585 ± 50 min. This plateau represents a period of stable hydrolysis product. Condensation reduced the transmissivity to 65 ± 3 % after 750 ± 75 min. A similar trend of decreasing hydrolysis rate was observed as pH 4.0, as the transmissivity increased to 82 ± 5 % after 270 ± 35 min and remained stable until 510 ± 90 min. The Turbiscan measurements clearly reveal optimal windows in which the two silanes are hydrolyzed, but condensation does not appear to be occurring.

To better assess the start of condensation, a more sensitive technique was employed. DLS was used to understand the evolution of the polymeric particles during the condensation process at acidic pH. Figure 2-5 shows a comparative hydrodynamic radius (R_h) of the polymeric NPs formed during the hydrolysis and condensation of 3F and nPM at pH 1.7. For nPM, after 80 ± 10 min of hydrolysis, NPs started to form as condensation started. Typically, particles are called "nano" when sizes are below 100 nm in at least one dimension. However, referring to particles as "nano" widely varies depending on their application fields, and the size range often goes above 100 nm and up to 500 nm.
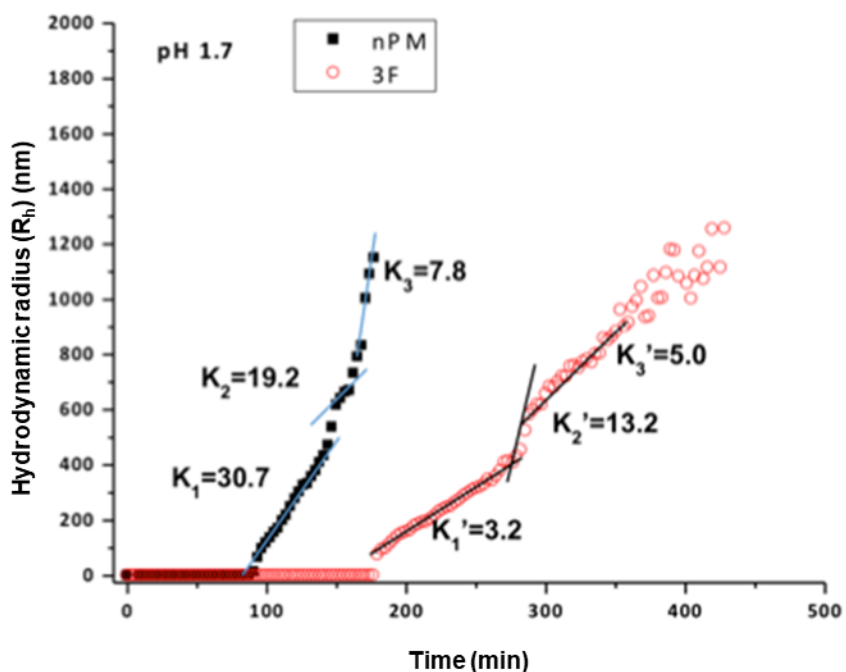
Figure 2-5. DLS comparison of evolution of polymeric NPs formation during the hydrolysis and condensation process of nPM and 3F at pH 1.7.

After 175±25 min, once the R_h became more than 1150±100 nm, they started to either separate from the solution or become larger than 2 μm in size, which is beyond the limit of detection for the DLS instrument. A aimilar pattern was observed in the case of 3F, as NPs started to form only after 160±20 min, where hydrolysis ended and condensation started. After 375±30 min, R_h was 1255±100 nm, and after that, no more particles could be observed, as particles either precipitated from the solution or became too large to be measured by DLS. As condensation progressed, NPs started to evolve with

three distinct slopes of K_1 (30.7), K_2 (19.2), and K_3 (7.8) for nPM and K_1' (3.2), K_2'

(13.2), and K_3' (5.0) for 3F, as shown in the condensation profiles (Figure 2-5). The

slower hydrolysis and condensation kinetics of 3F compared to nPM could be due to the

presence of the hydrophobic tri-fluoro group in 3F, which hinders the hydrolysis and

condensation steps shown in Figure 2-1. The three distinct slopes shown in the

condensation profiles of both 3F and nPM could represent the condensation steps such as

(021), (012), and (003) shown in Figure 2-1.

At pH 3.0, evolution of the polymeric particles was distinct, as compared to pH

1.7. At pH 3.0, polymeric particles started to appear earlier in the 3F solution, compared

to the nPM solution (Figure 2-6). Polymeric particles started to appear at 1400±150 min

in the 3F solution, which kept growing until 3400±250 min; then particles became either

too big to be measured by DLS or precipitated from the solution out of the light path. In

the nPM solution, particles started to appear at 2100±150 min and kept growing until

3100±200 min, and then no particles could be detected. But after 3700±300 min, particles

could be measured again until 4500±150 min; then particles disappeared and reappeared

again at 4800±200 min. This appearance and disappearance of particles could be due to

the continuous separation of larger particles form the solution and remodeling of the

particles. The system was unstirred and the temperature held constant. At pH 3.0,

condensation progressed with four distinct slopes of K_1'' (0.4), K_2'' (1.8), K_3'' (-0.6),

and K_4'' (0.7) in the 3F profile, but only one ($K_1''' = 1.4$) in the nPM.
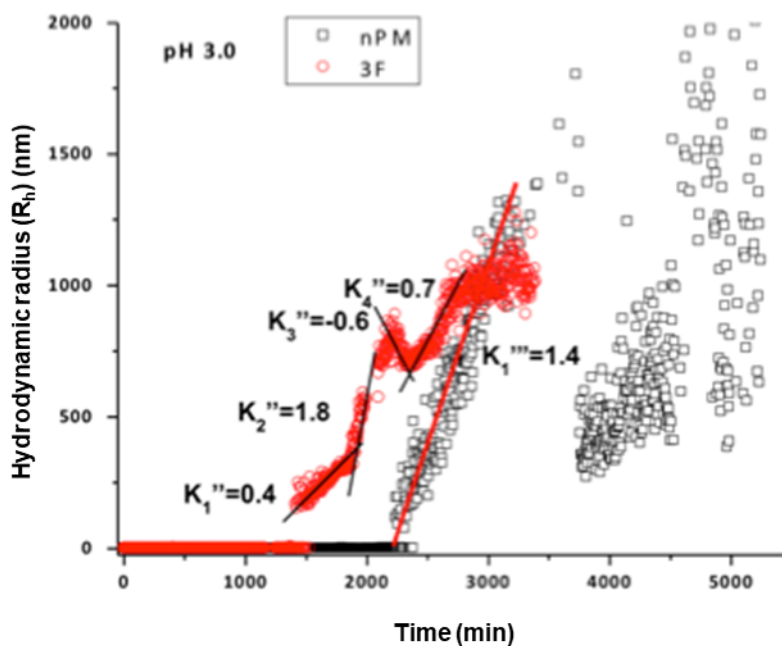
Figure 2-6. DLS comparison of evolution of polymeric NPs formation during the hydrolysis and condensation process of nPM and 3F at pH 3.0.

Correlations of transmissivities observed by Turbiscan with the hydrodynamic radiuses (R_h) of the polymeric particles measured by DLS at pH 1.7 and 3.0 for both nPM and 3F are shown in Figures 2-7 to 2-10. To compare the Turbiscan data with DLS data, transmissivity of the solution at the middle of the tube was compared, to measure turbidity arising from condensation rather than transmissivity changes due to depletion of the starting silanes that formed lenses. During the DLS analysis, 0.1 M nPM and 3F were used for the hydrolysis and condensation reaction unlike the concentration used for the Turbiscan study, where 0.4 M nPM and 3F were used. The use of low concentration was

necessary because DLS is unable to measure higher concentrations during the hydrolysis

and condensation process for both nPM and 3F, due to the cuvette geometry.
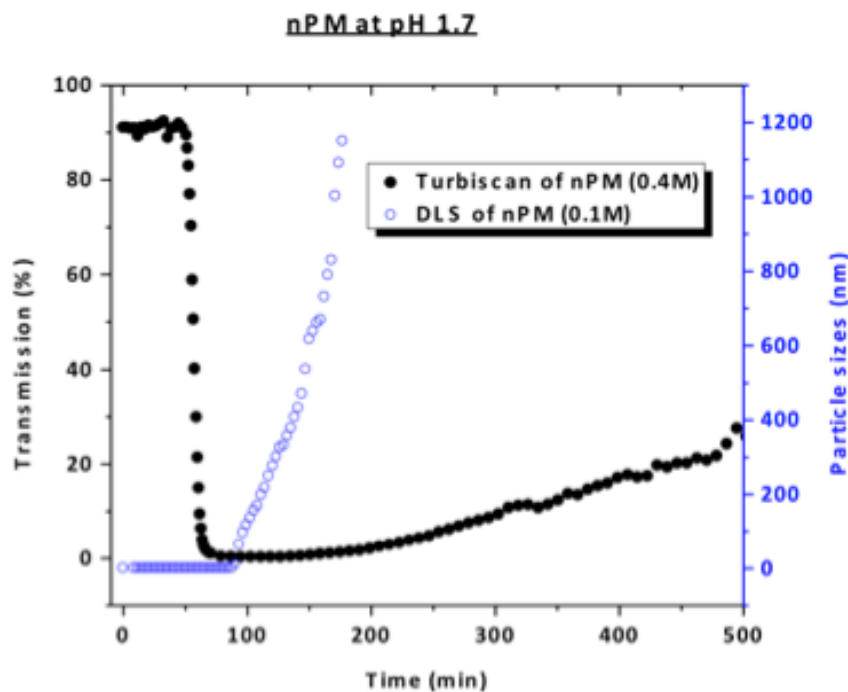
Figure 2-7. Correlation of Turbiscan transmission data with the DLS polymeric size (hydrodynamic radius, R_h) for nPM hydrolysis and condensation kinetics at pH 1.7.

Figure 2-7 shows the comparative data of Turbiscan and DLS of nPM at pH 1.7.

Even though Turbiscan data show that the transmissivity started to decrease after 60±5

min due to the turbidity in the solution, polymeric particles appeared only after 90±10

min in DLS. Two factors could be behind this delay of size appearance in DLS: first, it

could be due to the use of lower concentration of nPM; and second, it could be due to the

fact that at the beginning of the particles' formation, their sizes were too small to be observed by DLS. Once transmissivity turned 0 %, it started to increase again, as it appeared in case of transmissivity at the top.

The Turbiscan and DLS data for 3F at pH 1.7 (Figure 2-8) follow the same general trend as for nPM (Figure 2-7). In this case, polymeric NPs observed by DLS appeared earlier than the turbidity increase observed by Turbiscan. Polymeric particles started to appear in the DLS profile after 180 ± 20 min, but were not of sufficient size or concentration to reduce light transmission in the Turbiscan, which began to decrease after 240 ± 30 min. The reason could be the height difference of the data point of where the reading was taken. After almost the same time (250 ± 30 min), when the particles started to separate or become too large to be detected by DLS, the Turbiscan reading could be observed having the lowest transmissivity.
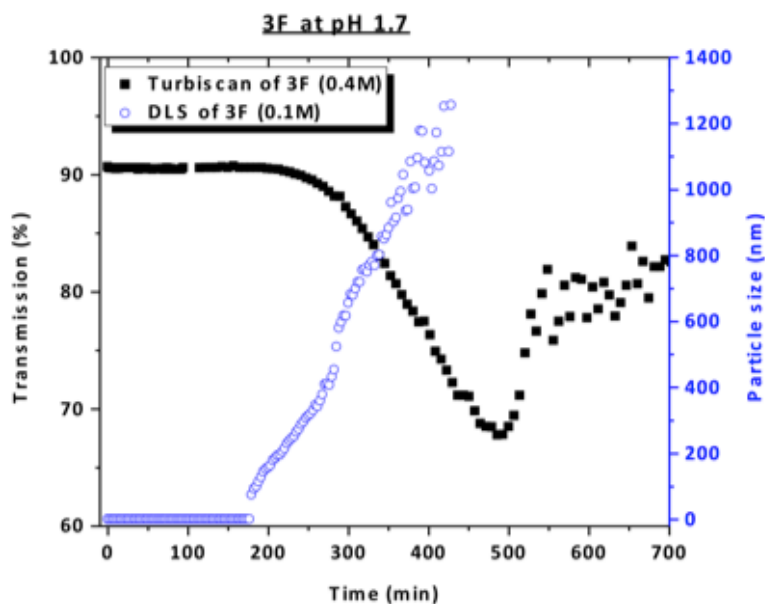
Figure 2-8. Correlation of Turbiscan-analyzed transmission data with the DLS-obtained polymeric size (hydrodynamic radius, R_h) for 3F hydrolysis and condensation kinetics at pH 1.7.

Figure 2-9 shows the comparative data for nPM at pH 3.0, where light transmissivity started to reduce far earlier (700±80 min) than the time where polymeric particles started to appear in DLS (2100±100 min). This major time difference could be due to the difference in surface to volume ratio in the liquid-air and liquid-liquid interface ratio in the two solution containers used for Turbiscan and DLS. Also, the height difference of the sampling points in the tubes could be a factor as well. After 1000±60 min, the Turbiscan data showed the lowest transmissivity, and then a sudden increase was observed at 1060±60 min, which could be due to the aggregation / sedimentation of

larger particle formations from the solution. This pattern can be observed in the DLS

data, but only after 3320±150 min.
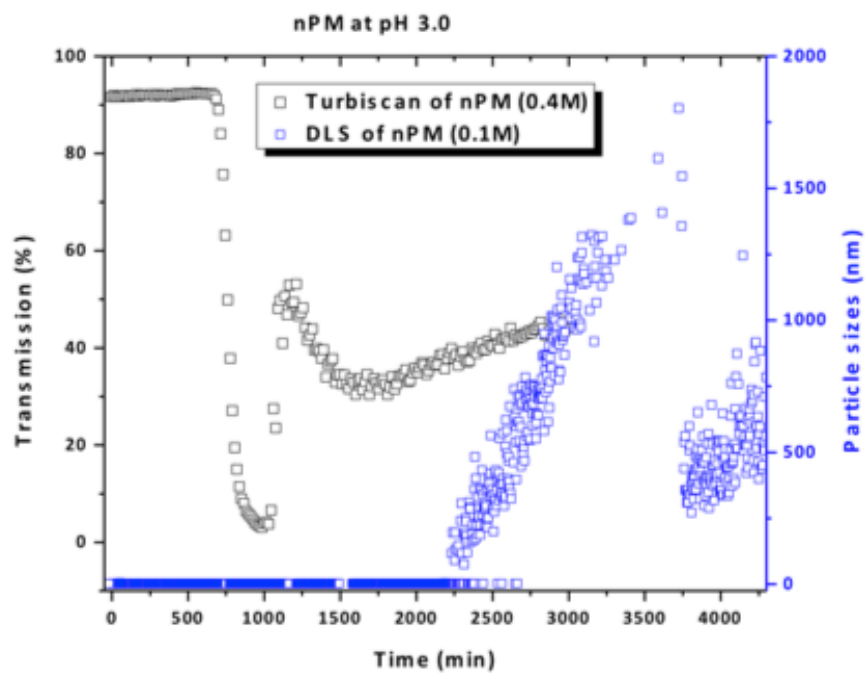
Figure 2-9. Correlation of Turbiscan transmission data with the DLS-obtained particle sizes (hydrodynamic radius, R_h) for nPM during the hydrolysis and condensation kinetics at pH 3.0.

A similar trend could be seen in case of 3F at pH 3.0 (Figure 2-10), where the

Turbiscan-analyzed data showed that the transmissivity started to reduce after 840±60

min, but these polymeric particles could be seen in DLS only after 1420±100 min.
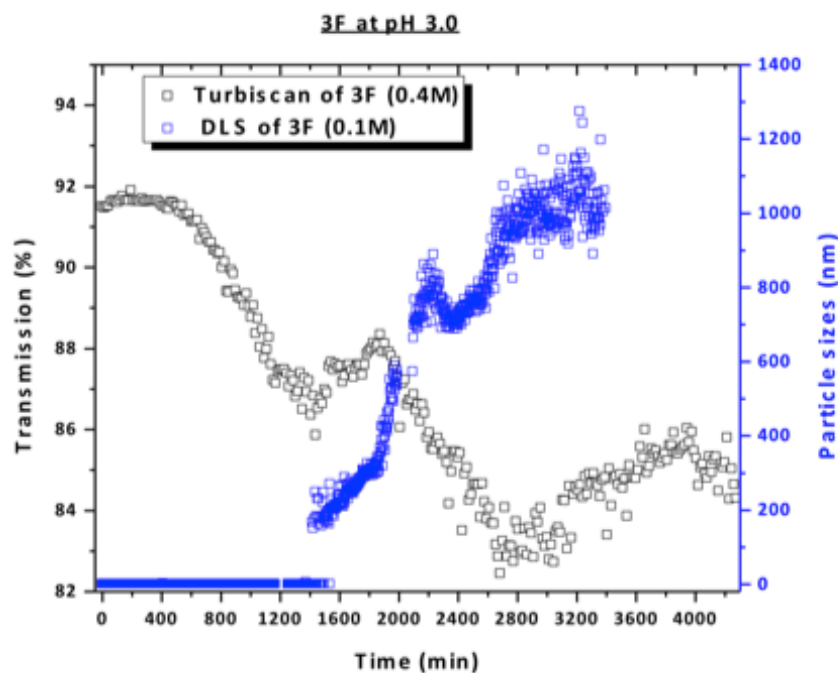
Figure 2-10. Correlation of Turbiscan-analyzed transmission data with the DLS-obtained particle sizes (hydrodynamic radius, R_h) during 3F hydrolysis and condensation kinetics at pH 3.0.

Similar to the nPM at pH 3.0, the reduction and increase of transmissivity and

hydrodynamic sizes were observed as condensation continued for 3F at pH 3.0

Figure 2-11 (a) and (b) show the AFM images of the polymeric NPs formed

during the condensation process of nPM at pH 1.7. Polymeric NPs became 10±5 to

100±20 nm after 180 min (Figure 2-11 (a)), but over the time, these particles became

irregular in shapes and sizes. Figure 2-11 (b) shows the transformation of the polymeric

NPs after 1440 min, where large and irregular particles can be observed.
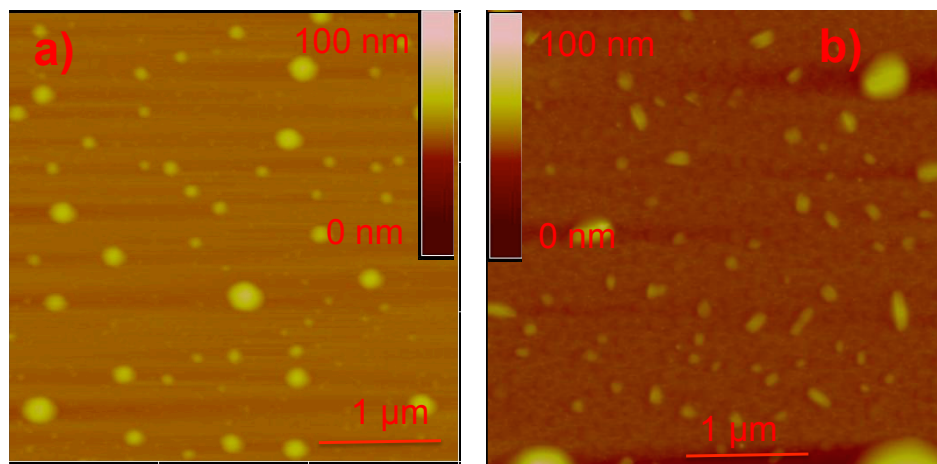
Figure 2-11. AFM images of polymeric NPs formed following the condensation of nPM after (a) 180 min and (b) 1440 min.

Similarly, Figure 2-12 (a) and (b) show the AFM images of the polymeric NPs formed during the condensation of 3F at pH 1.7. Polymeric NPs became 12 ± 5 to 200 ± 30 nm after 300 min (Figure 2-12 (a)). These particles kept growing over time, and after 1440 min, micron-sized particles were observed, along with the nano-sized particles (Figure 2-12 (b)).
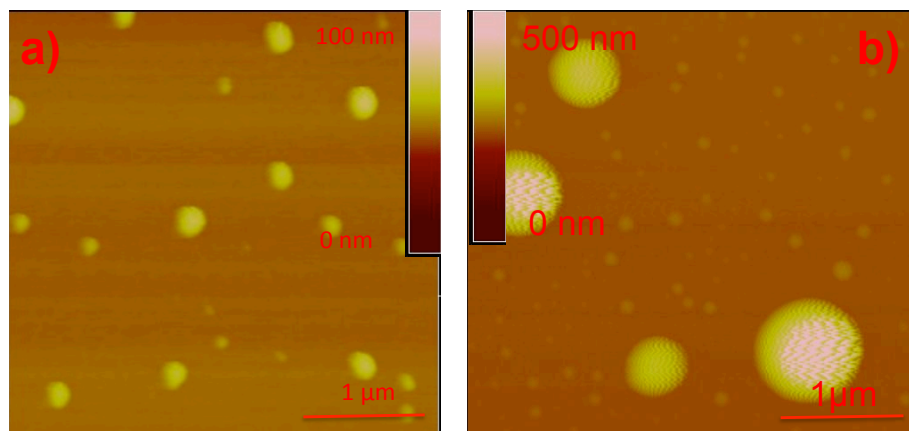
Figure 2-12. AFM images of polymeric NPs formed following the condensation of nPM after (a) 300 min and (b) 1440 min.

The ATR-FTIR spectra of nPM (0.4 M) and 3F (0.4 M) were taken at various time intervals during the hydrolysis and condensation at pH 1.7. Figures 2-13 and 2-14 show the ATR-FTIR spectra of the nPM and 3F solutions, respectively, at different transition phases during hydrolysis and condensation. Since spectra were taken directly from the aqueous solutions, the H-O-H bending peak can be observed in all the spectra of nPM (at 1635 cm^{-1}) or 3F (at 1650 cm^{-1}) throughout the hydrolysis and condensation processes.
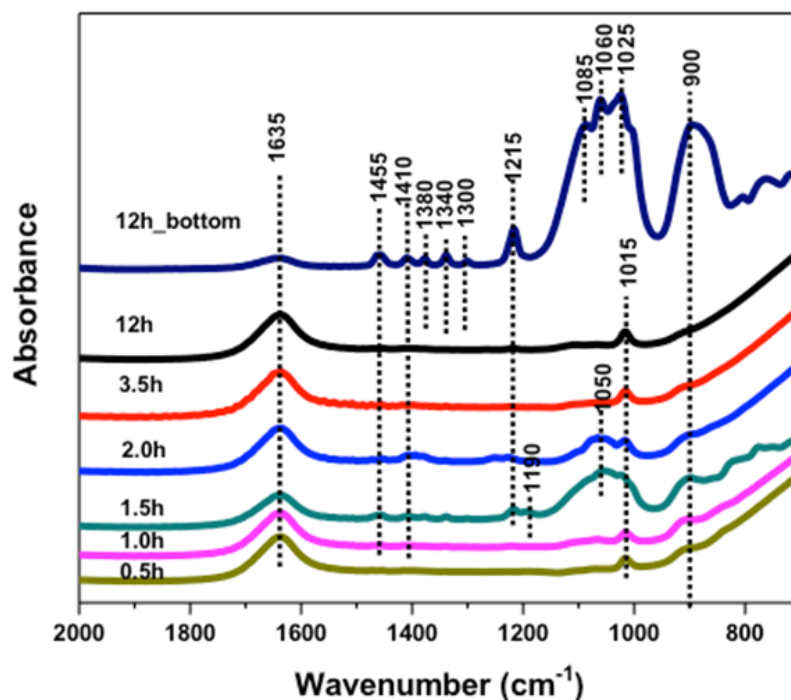
Figure 2-13. ATR-FTIR spectra of nPM at defined times during the hydrolysis and condensation process.

A Si-OH band appeared after 0.5 h at 900 cm^{-1} in the ATR-FTIR spectrum of the nPM (Figure 2-13), indicating ongoing hydrolysis. At this time another peak representing a Si-CH$_2$ band was also observed at 1015 cm^{-1}. After 1.5 h, as condensation began, this Si-OH band disappeared and the stretching vibration of Si-O-Si started to appear at 1000-1100 cm^{-1} (Figure 2-13). At this time (1.5 h), a strong Si-alkoxy (Si-O-CH$_3$) band was also observed at 1190 cm^{-1}, which implies that at this time hydrolysis was still in

progress, even though condensation has started already. After 2 h, this peak for the Si-O-CH$_3$ band disappeared, confirming the end of the hydrolysis. As condensation continued, the bands representing Si-O-Si, started to disappear (3.5 h and 12 h) as polymeric particles got larger and precipitated from the solution to form a gel at the bottom. After 12 h, the peaks for the Si-O-Si and Si-O-CH$_3$ bands appeared in the spectrum representing the gel from the bottom. Strong Si-CH$_2$ band at 1215 cm^{-1} and some vibrational peaks for C-H and C-H$_2$ can also be observed at 1315 to 1455 cm^{-1}.

Unlike the nPM spectra, 3F spectra did not show a strong band for Si-OH at 900 cm^{-1} during the possible hydrolysis period of 3F (Figure 2-14), but a weak Si-OH band appeared at 935 cm^{-1} in the spectra representing the solution at 2.5 h, 3.5 h, and 6 h, but not at 24 h. After 2.5 h, stretching vibration of Si-O-Si appeared at 1000-1100 cm^{-1}, confirming condensation. Strong stretching vibration for –CF was observed in all the spectra at 1215 and 1267 cm^{-1}. Absorbance intensity at 1215 cm^{-1} was stronger, due to the combination of Si-CH$_2$ and –CF bands. All the peaks representing the Si-O-Si band in between 1000 cm^{-1} to 1100 cm^{-1} appeared in the spectrum representing the gel at the bottom after 24 h. Vibrations of C-H and C-H$_2$ also were observed in a wide range of wavenumbers (1315 cm^{-1} to 1450 cm^{-1}) in this spectrum.
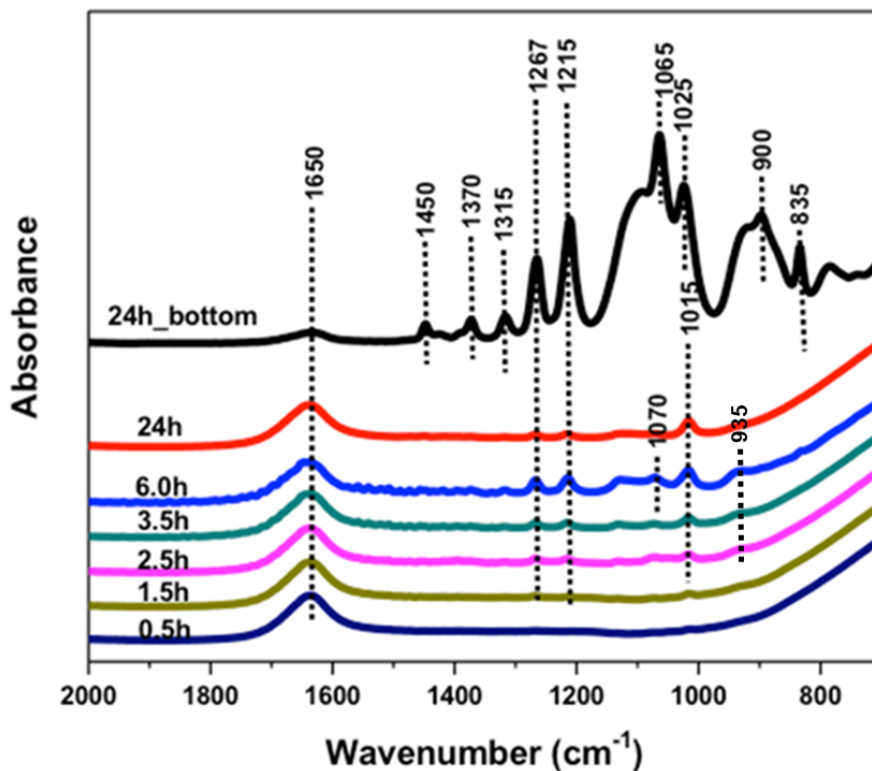
Figure 2-14. ATR-FTIR spectra of 3F at defined times during the hydrolysis and condensation process.

Zeta potential was studied to understand the physical phenomena such as surface charges of the condensed particles or aggregates. Zeta potential measures the average surface charge of the particles in a colloidal suspension with millivolt resolution. Figure 2-15 shows the zeta potential of the particles formed during the hydrolysis and condensation of nPM at pH 1.7 and 3.0. At pH 1.7, the zeta potential of condensed

polymeric particles fluctuated in between 0 to -5 mV. Since the isoelectric point of silica

particles is close to pH 2.0, zeta potential of the polymeric particles generated from nPM

at pH 1.7 were also expected to be close to zero.
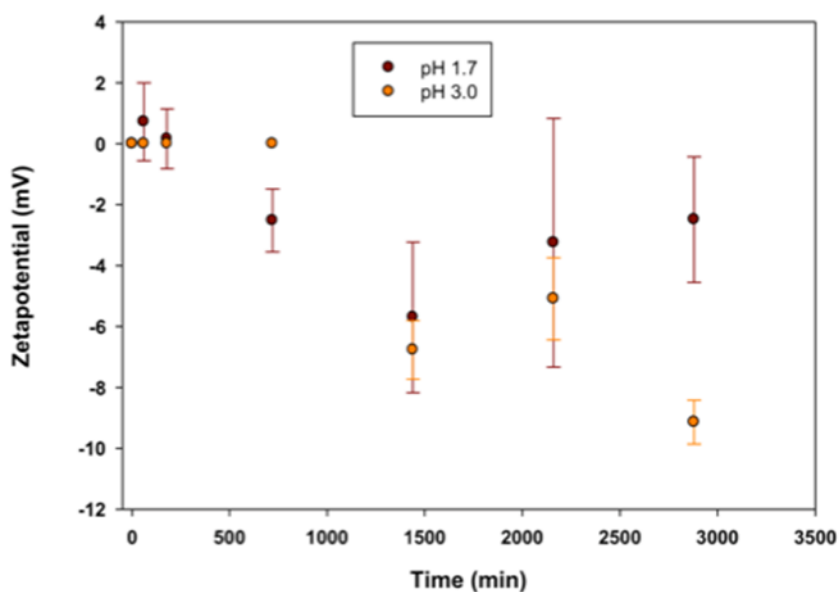
Figure 2-15. Zeta potential of polymeric NPs evolving from nPM during the hydrolysis and condensation processes at pH 1.7 and 3.0.

At pH 3.0, the nPM NPs have a zeta potential between -7 mV and -9 mV. The

increase in negative charge compared to the particles formed at pH 1.7 is expected if free

silanol groups are present on the nPM NPs that would be deprotonated as the pH is

increased above the isoelectric point.
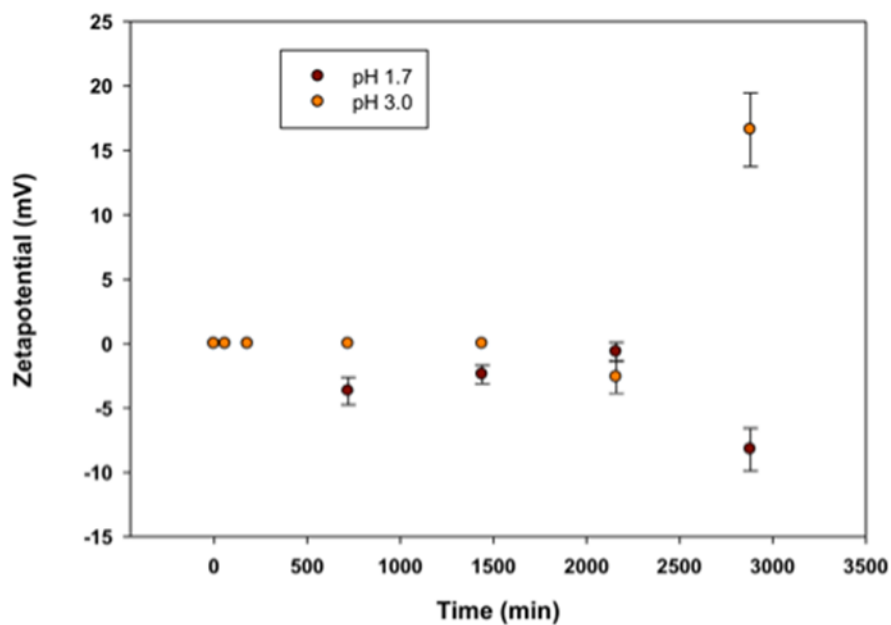
Figure 2-16. Zeta potential of polymeric NPs evolve from 3F during the hydrolysis and condensation process at pH 1.7 and 3.0.

Figure 2-16 shows the zeta potential of the particles formed during the hydrolysis and condensation of 3F at pH 1.7 and 3.0. At pH 1.7, zeta potential of the fluorinated polymeric particles was near zero mV until 2300 min, but it decreased to -8 mV after 2800 min. These decreases in the zeta potential value could be due to the continual growth of polymeric particles with higher surface charges. At pH 3.0, the zeta potential values remained close to zero mV, similar to pH 1.7 until 2300 min, but they surprisingly increased to 17 mV after 2800 min.

2.5 Conclusion

These studies on the evolution of polymeric NPs during hydrolysis and condensation of two types of hydrophobic tri-alkoxysilanes showed the distinct pattern of hydrolysis and condensation rates at various pH. These patterns were correlated using the complementary methods of turbidity scanning with Turbiscan, and monitoring evolution of particles with DLS. Hydrolysis and condensation kinetic profiles of 3F and nPM allowed the processes of hydrolysis and condensation to be tuned through the selection of pH, to provide optimal interaction with biological molecules for various applications, ranging from enzyme encapsulation to the modulation of protein conformation. AFM images confirmed the NP sizes, and revealed heterogeneity in shapes, while ATR-FTIR spectra showed the chemical compositions of the polymeric NPs generated during the condensation. Of particular interest was the presence of a silanol signal in the NP spectra, suggesting that condensation did not consume all silanols. Zeta potential confirmed this as it revealed a negative surface character on these nanoparticles. Surface available silanols combined with the hydrophobic tri-fluoro or methyl groups are desirable for applications of these two hydrophobic silanes toward modulating the protein secondary structures and corresponding fibrillation propensity.

2.6 References

1. Plueddemann, E. P. *PMSE Abstr. Pap. Am. Chem. Soc.* **1984**, *187*, 92.

2. Leyden, D. E., Chemically moDIfied surfaces: Silanes Surfaces and interfaces, First eDItion, 1986.

3. Plueddemann, E. P., Silane coupling agents, Second eDItion, 1991.

4. Spivack, J. L.; Pohl, E. R.; Kochs, P. Organoalkoxysilanes, Organosilanols and Organosiloxanols. *In Organosilicon Materials, The Handbook of Environmental Chemistry* (Chandra, G., Ed.; Springer-Verlag: Berlin), **1997**, *3* (H), 105.

5. Sanchez, J.; McCormick, A. *J. Phys. Chem.* **1992**, *96* (22), 8973.

6. Brinker, C. J. *J. Non-Cryst. Solids,* **1988**, *100*, 31.

7. Arkles, B.; Steinmetz, J. R.; Zazyczny, J.; Mehta, P. *J. Adhes. Sci. Technol.* **1992**, *6* (1), 193.

8. Schmidt, H.; Scholze, H.; Kaiser, A. *J Non-Crystalline Solids* **1984**, *63* (1–2), 1.

9. Oostendorp, D. J.; Bertrand, G. L.; Stoffer, J. O. *J. Adhes. Sci. Technol.* **1992**, *6* (1), 171.

10. Salon, B.; Belgacem, M. N. *Colloid Surf. A: Physicochem. Eng. Aspects* **2010**, *366*, 147.

11. Hardman-Rhyne, K. A.; Coyle, T. D.; Lewis, E. P.; Spooner, S. *Mater. Res. Soc. Symp. Proc.* **1986**, *73*, 173.

12. Stoffer, J.; Oostendorp, D. *Proc. Water-Borne High-Solids Coat Symp.* **1988**, *15*, 513.

13. Osterholtz, F. D.; Pohl, E. R. *J. Adhes. Sci. Technol.* **1992**, *6* (1), 127.

14. Salon, M. C. B.; Belgacem, M. N. *Phosphorus, Sulfur Silicon Relat. Elem.* **2011**, *186* (2) 240.

15. Shi X.; Graiver, D.; Narayan, R. *Silicon* **2012**, *4*, 109.

16. Peng, Y.; Turner, N. W.; Britt, D. W. *Colloids Surface B* **2014**, *119*, 6.

17. Krakovsky, I.; Urakawa, H.; Kajiwara, K.; Kohjiya, S. *J. Non-Cryst. Solids* **1998**, *231*, 31.

18. Šefčík, J.; McCormick, A. V. *Catal. Today* **1997**, *35*, 205.

19. Rankin, S. E.; Macosko, C. W.; McCormick, A. V. *AIChE J.* **1998**, *44*, 1141.

20. Alam, T. M.; Assink, R. A.; Loy, D. A. *Chem. Mater.* **1996**, *8*, 2366.

21. Torry, S. A.; Campbell, A.; Cunliffe, A. V.; Tod, D. A. *Int. J. Adhes. Adhes.* **2006**, *26*, 40.

22. Chambers, R. C.; Jones, W. E.; Haruvy, Y.; Webber, S. E.; Fox, M. A. *Chem. Mater.* **1993**, *5*, 1481.

23. Alie, C.; Pirard, J. P. *J. Non-Cryst. Solids* **2003**, *320*, 21.

24. Ogasawara, T.; Yoshino, A.; Okabayashi, H.; O'Connor, C. J. *Colloids Surf. A* **2001**, *180*, 317.

25. Riegel, B.; Blittersdorf, S.; Kiefer, W.; Hofacker, S.; Müller, M.; Schottner, G. I. *J. Non-Cryst. Solids* **1998**, *226*, 76.

26. Shih, P. T. K.; Koenig, J. L. *Mater. Sci. Eng.* **1975**, *20*, 137.

27. Kozerski, G. E.; Gallavan, R. H.; Ziemelis, M. *J. Anal. Chim. Acta* **2003**, *489*, 103.

28. Chen, S. L.; Dong, P.; Yang, G. H.; Yang, J. J. *Ind. Eng. Chem. Res.* **1996**, *35*, 4487.

29. Kozerski, G. E.; Gallavan, R. H.; Ziemelis, M. J. *Anal. Chim. Acta* **2003**, *489*, 103.

30. Pelster, S. A.; Schrader, W.; Schüth, F. *J. Am. Chem. Soc.* **2006**, *128*, 4310.

31. Leyden, D. E.; Atwater, J. B. *J. Adhes. Sci. Technol.* **1991**, *5* (10), 815.

32. Salon, B.; M. C.; Bayle, P. A.; Abdelmouleh, M.; Boufi, S.; Belgacem, M. N. *Colloid Surf. A: Physicochem. Eng. Aspects* **2008**, *312*, 83.

33. Krakovský, I.; Urakawa, H.; Kohjiya, S.; Ochiai, K.; Yamashita, S.; Kohjiya, S. *J. Non-Cryst. Solids* **1998**, *231*, 31.

34. Tejedor-Tejedor, M. I.; Paredes, L.; Anderson, M. A. *Chem. Mater.* **1998**, *10*, 3410.

35. Rose, S. V.; Marcellan, A.; Hourdet, D.; Creton, C.; Narita, T. *Macromolecules*, **2013**, *46* (11), 4567.

36. Huang, X. F.; Xiong, Y. J.; Yin, W.; Lu, L. J.; Liu, J.; Peng, K. M. *Energy & Fuels* **2016**, *30* (6), 5190.

CHAPTER 3

SILANE-PROTEIN INTERACTIONS : FLUORINE-BASED SELF-ASSEMBLED

HYDROPHOBIC POLYMER NANOPARTICLES INHIBIT AMYLOID

FIBRILLATION OF ß-LACTOGLOBULIN

3.1 Abstract

Fluorinated polymeric nanoparticles (NPs) inhibited the amyloid fibrillation of β-lactoglobulin (BLG). Initially, inhibition of fibrillation was observed qualitatively by DLS as hydrodynamic radius (R_h) in aqueous solution under the model conditions for BLG to form fibrils. Later, AFM-analyzed morphological study confirmed the inhibition of the amyloid fibrillation of BLG by the fluorinated polymeric NPs. Along with the fluorinated polymeric NPs, fluorine-free or methylated polymeric NPs were also tested against the amyloid fibrillation, and AFM images showed that they partially inhibited the fibrillation. During the fibril inhibition process, protein-fluorinated silica-based stable nanocomposite particles with the sizes <12 nm were generated. Deconvoluted ATR-FTIR spectra showed that β-sheet decreased by 29 % and 11% after BLG was treated with fluorinated polymeric NPs and methylated polymeric NPs, respectively. Docking study showed the existence of hydrogen bonding between BLG and both fluorinated and methylated silanol monomers.

3.2 Introduction

Accumulation of fibrillated protein aggregates in the brain or other tissues are commonly known as amyloid. Amyloid is a pathological feature of a series of neurodegenerative disorders such as Alzheimer's disease (AD), Parkinson's disease (PD), Huntington's disease (HD), type II diabetes, and Prion disease. (1-8) Amyloid forms due to the destabilization of α-helices and the simultaneous formation of highly ordered cross β-sheet structures that assemble into the characteristic plaques. (9-11) Also, the presence of buried hydrophobic surfaces or favorable packing of side chains contribute to the stability of the amyloid structure and makes it very resistant to degradation and depolymerization. The amyloid hypothesis correlates disease symptoms and sequence with fibrils and plaques, thus plaque-targeting is widely investigated. Molecules that stabilize α-helix or inhibit the formation of β-sheets are potential candidates to maintain the native structure of the protein and avoid amyloid formation. Thus, molecules capable of inducing conformational transition in protein should be used to develop the therapeutics to stabilize the nonpathogenic conformation. Also, the therapeutics should be able to prevent the recruitment of native proteins by the misfolded / pathogenic seed, which eventually will inhibit the amyloid formation. At present, however, there is no effective drug to cure the amyloid-based diseases, and the treatment of symptoms is also extremely limited. Most of the drugs that have been developed to target amyloid-based diseases have failed at various stages of their clinical trials. (12)

Several types of molecules have shown inhibiting ability against the amyloid growth, such as various biomolecules including peptides / antibodies, drugs, small molecules including phenolic compounds, gene therapy, and chaperones. (13-30) With the recent advancement of nanotechnology, a new therapeutic avenue has opened with the use of various NPs against amyloid fibrillation of amyloidogenic proteins. The potential influence of NPs on protein fibrillation is the function of their surface chemical functional groups, their interfacial properties including surface charges, and their shapes and sizes, which decide the surface to the volume ratio. Studies have shown that NPs are capable of crossing the blood-brain barrier (BBB) and have greater in vivo stability. (17) NPs can both inhibit and promote amyloid fibrillation, depending on surface properties, core material, assembly, concentration, and type of functional molecules present on it. For example, copolymer particles of N-isopropylacrylamide: N-tert-butylacrylamide, cerium oxide, quantum dots (QDs), carbon nanotubes, citrate-capped gold NPs, and titanium oxide are reported to promote protein assembly into amyloid fibrils in vitro, by assisting the nucleation process. (31-45), In contrast, various inorganic NPs, hydrophobic NPs, NPs functionalized with hydrophobic molecules and specific affinity molecules such as curcumin (46-48), dextran (49), and sialic acid (50-51) reportedly inhibit fibrillation processes.

Among the functionalized NPs, fluorinated NPs are of special interest due to the properties of fluorine atoms: addition of fluorine atoms increases the pharmacological

activity. Thus, various fluorinated antibiotics, anticancer, anti-inflammatory, and antiviral therapeutics have been reported. (52-54) Another beneficial property of the fluorine substitution is the increase of BBB permeability achieved by the modification of the lipophilicity or amine pKa. In fact, approximately a quarter of all the drugs developed for pharmaceutical purposes have the presence of fluorine atoms. (55-58) Fluoro-substituted alcohols such as TFE (2,2,2-trifluoroethanol) and HFIP (1,1,1,3,3,3-hexafluoro-2-propanol) are strong inducers of protein and peptide structures. (59) The hydroxyl group in HFIP and TFE preferentially binds with a carbonyl oxygen of protein backbone and acts as a protein donor, whereas the strong electronegative F group acts as a hydrogen acceptor, forming H-bonds with proton donor groups on protein. (58-61) As a consequence, the solvent exposure of the amide is minimized and the intra-polypeptide hydrogen bonding of the amide group is favored, leading to increased helical propensities. Increased hydrophobicity, which arises from both hydrocarbon groups and multiple F atoms in the fluoro-alcohols, plays an essential role in denaturing protein secondary structures and inducing the formation of helical structures. (58) A major issue with these fluoro-substituted alcohols as amyloid fibril inhibitors is their application as therapeutic agent to the targeted proteins. Thus, fluorinated polymeric NPs having multiple stable hydroxyl groups with hydrophobic characteristics are desirable to be used as therapeutic agents to inhibit amyloid fibrillation, which can be achieved using a polymerizable analog of fluoro-alcohol such as hydrolyzed fluoro-silane.

Our recent works suggest that fluoro-silane 3,3,3-trifluoropropyl trimethoxy silane (3F) is very highly efficient as protein secondary structure inducer in its hydrolyzed states. (62) Hydrolyzed 3F (H3F) can convert β-sheet structure to α-helix, where 3F- groups promote 3F-protein interaction by forming H-bonds with hydrogen donors on the protein; consequently disrupting the intra-molecular H-bonds between distant residues involved in β-sheets, and favoring H-bonding between more proximal amino acids on the polypeptide chain, leading to α-helices. Given that the β-sheet structure is the reason why amyloid fibrils formed, fluorinated polymeric NPs having the same characteristics as H3F capable of inducing β-sheet would be a strong candidate as amyloid inhibitor, which could be achieved by condensing the H3F.

In this study, anti-fibrillar activity of fluorinated polymeric NPs was investigated against a model template protein β-lactoglobulin (BLG) which exhibits predominantly β-sheet secondary structure. BLG is a globular protein containing 162 amino acids, with a MW of 18.4K g/mol, IEP of 5.1, and an internal hydrophobic core surrounded by a hydrophilic exterior. In order for BLG to form amyloid fibrils, it first refolded into protofilament at acidic pH and at temperature >80°C, where the protein possesses a dominant positive charge. (63) If heating continues for a few hours, the contour length of these protofilaments become > 0.5 μm, forming amyloid fibrils. (64) Since the fibrils of globular proteins have a similar structure to those causing amyloidosis diseases, BLG has been widely investigated to understand the amyloid fibril formation. (65-77)

BLG is not only well characterized, it is also easily available and relatively cheap, and that is the reason why we have selected it as our model template protein. Non-fluorinated or methylated polymeric NPs were also investigated against BLG, to demonstrate the importance of the fluorine moieties in the NPs for anti-fibrillation activities; and these methylated polymeric NPs were obtained with the condensation of hydrolyzed n-propyltrimethoxy silane (HnPM).

The objective of this study was to investigate the modulation of fibril properties of BLG using fluorinated and methylated polymeric NPs, study the secondary structural transformation in the BLG during the BLG-NPs interaction, and molecular docking of protein-ligand interactions.

3.3 Materials

3,3,3-trifluoropropyl trimethoxy silane (3F, > 95 % purity, MW = 218.3, d = 1.14 g/ml) and n-propyltrimethoxy silane (nPM, > 95 % purity, MW = 164.3, d = 0.94 g/ml) were purchased from Gelest, Inc. (Morrisville, PA). β-lactoglobulin from bovine milk (BLG, > 90 % purity, MW = 18,400) was obtained from Sigma-Aldrich (St. Louis, MO); the thioflavin T powder was purchased from EMD Millipore, Darmstadt, Germany; and Muscovite mica was purchased from SPI supplies for the AFM study (PA, USA).

3.4 Experimental methods

Preparation of BLG solutions

BLG stock solution was prepared by dissolving 200 mg of BLG powder in 10 ml double distilled deionized (DI) water at pH 2.0 with gentle shaking, which gave 20 mg/ml (1.088 mM) solution. The dissolved BLG solution was then filtered through a 0.2 μm syringe filter (Millex-GS, Millipore) and stored at 4°C.

Dynamic Light Scattering (DLS) analysis

Evolution of the hydrodynamic sizes (R_h) of the polymeric NPs during the hydrolysis and condensation of nPM and 3F was analyzed using DLS (DynaPro NanoStar, Wyatt Technology Corporation, Santa Barbara, CA). Measurements were taken using a quartz cuvette (JC-426, 1 μl) filled with 0.7 ml 3F (0.1 M) or nPM (0.1 M) aqueous solutions at pH 2.0. Hydrolysis and condensation kinetics of 3F and nPM were collected over 10 h. For the BLG fibrillation study, initially 0.7 ml BLG solution (1 mg/ml (0.013 mM) and pH 2.0) was added in the cuvette, and its R_h was measured. After that, the same BLG solution was heated for 3 h at 90°C, to observe the R_h of the fibrils. To measure the R_h sizes of the products generated after the interaction of BLG with fluorinated and methylated polymeric NPs, 0.7 ml of 3F or nPM solutions (0.2 M) at pH 2.0 were monitored as the hydrolysis progressed. After the hydrolysis was completed, the 0.35 ml solution was replaced with 0.35 ml of 2 mg/ml (0.026 mM) BLG solution (at pH

2.0) and the R_h size was measured after heating the sample for 3 h at 90°C. For the

control sample, 0.35 ml aqueous solution (at pH 2.0) was used without adding BLG.

Amyloid fibrillation with polymeric NPs

0.4 M 3F and nPM solutions were prepared adding 0.18 ml of 3F and nPM in 5

ml glass vials, where 2.32 ml of DI water (at pH 2.0) were already kept. As soon as all 3F

and nPM were hydrolyzed, condensation followed immediately, and started to form

polymeric NPs. Once all of the 3F and nPM were hydrolyzed, 0.75 ml 3F and nPM were

added separately to 0.25 ml of BLG (1.088 mM) solution in 5 ml glass vials with

magnetic stir bars in them. Reaction was let to occur for 5 min at room temperature

(23°C), then transferred to an oil bath with temperature of 90°C, and the samples were

heated for 5 h. For the control samples, in three separate glass vials, 3F (0.3 M), nPM

(0.3 M), and BLG (0.272 mM) were also heated at 90°C for 5 h. Reactions were stopped

using ice bath; and once solution temperature came down to room temperature, different

analyses were performed.

Thioflavin T (ThT) fluorescence assay

A stock solution of 3.0 mM ThT in phosphate-NaCl buffer (10 mM phosphate and

150 mM NaCl, pH 7.0) was filtered through a 0.2 μm syringe filter (Millex-GS,

Millipore). Stock solution was stored at 4°C in a brown glass bottle covered with

aluminum foil. Working solution was prepared by diluting stock solution 50-fold in

phosphate-NaCl buffer (the final ThT concentration was 60 μM). 200 μl samples were

added on the 96-well plate from the 2.5 ml glass vials, where ThT and target solutions were added at 3:1 ratio. Emission spectra were taken from 460 nm to 560 nm after excitation at 440 nm, using a Synergy4 Hybrid Multi-Mode Micro Plate Reader (BioTek, Inc., VT, USA).

Fibrillation analysis with Atomic Force Microscopy (AFM)

To observe the structural formation of BLG fibrils and polymeric NPs, AFM images were taken using a Nanoscope III Bioscope (Digital Instrument, Inc.) in tapping mode. 100 µl samples were dropped onto freshly cleaved mica surfaces, then gently washed with DI water, and air-dried before taking AFM images. AFM tips were obtained from TED Pella Inc., CA (TAP300AL-G-50).

Fourier Transformed Infrared Spectroscopy (FTIR)

The interactions of BLG with fluorinated and methylated polymeric NPs were analyzed by FTIR using a Varian 660-IR with a horizontal single reflection Pike Technologies MIRacle attenuated total reflectance (ATR) unit, fitted with a ZnSe crystal. 100µl samples were drop cast on the ZnSe crystal of the ATR platform and air-dried before taking the reading. Readings were taken after averaging 20 scans over the range of 1200 cm^{-1} to 1800 cm^{-1}, with a resolution of 1 cm^{-1}. Prior to each reading, a background scan was acquired. FTIR obtained spectra were later deconvoluted using ORIGIN PRO 2017, to ascertain the influence of the fluorinated and methylated polymeric NPs on the secondary structural motifs of BLG, along with the untreated BLG and BLG fibrils.

Docking studies

Docking study was performed using Autodock 4.2.6. The 3D structures of H3F and HnPM monomers were drawn using Marvin software. BLG was interacted with H3F and HnPM monomers using Autodock Tools 1.5.6. Hydrogen atoms were added and Kollman charges were used to set the charges on BLG, and Gasteiger charges were added to H3F and HnPM monomers. The docking grids were carried out with a default spacing value of 1 Å, and grid volume $70 \times 70 \times 70$ points, covering the entire surface of the BLG. The protein molecule was set to rigid, while the ligand molecule was considered to be flexible. In the docking simulation, a Lamarckian generic algorithm was used to generate 10 binding models, each of which was individually selected as the lowest binding energy among a maximum of 2,700,000 evaluations. These 10 complexes were clustered according to their root-mean-square deviation (RMSD) values and binding energies, in order to distinguish the preferred binding model.

Statistical analysis

Triplicate samples were studied throughout the experiment, and average values with the associated standard deviations were calculated and shown in the appropriate Figures. One-way ANOVA test was performed using Sigma Plot 13.0.

3.5 Results and Discussion

Hydrolysis was favored over condensation at acidic pH, and all three O-CH$_3$ of 3F and nPM underwent sequential hydrolysis, yielding silanols. Polymeric NPs containing silanol were generated in aqueous media, as condensation followed the hydrolysis. Presence of silanol in the NPs is desirable in the amyloid inhibition process, as it showed the secondary structure inducing ability. (78) Aqueous synthesis of NPs makes them suitable to be used in the biological system. The hydrolysis and condensation kinetic profiles of 3F and nPM as well as the evolution of the hydrodynamic radius (R$_h$) of the NPs are shown in Figure 3-1, obtained from DLS analyzed data. NPs started to appear as the condensation began at 80±10 min for nPM and at 180±20 min for 3F. As condensation progressed, NPs continued to grow and become >1 μm in 180±25 min for nPM and in 400±50 min for 3F. The NPs" growth rate had a sudden jump after the R$_h$ size turned 400±20 nm for both 3F and nPM; and possibly the aggregation of the individual NPs was due to electrostatic interactions.
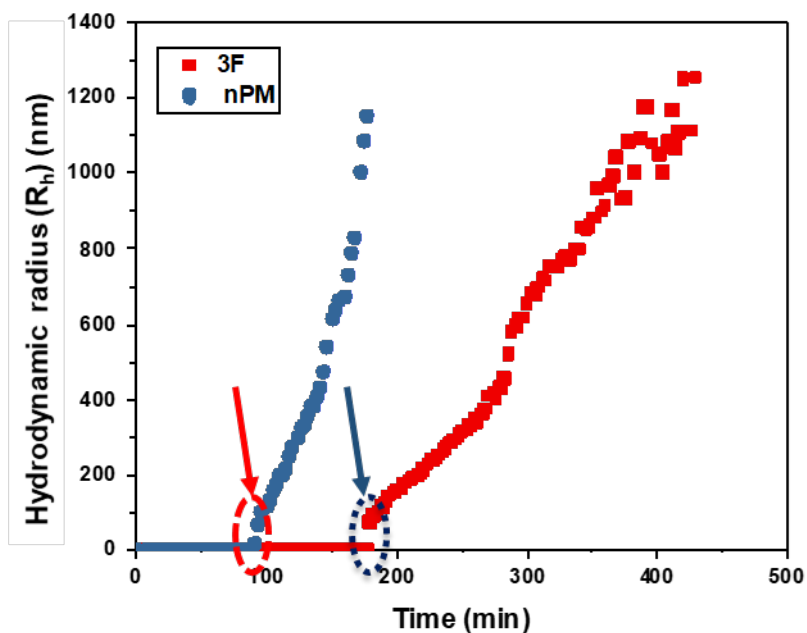
Figure 3-1. Evolution of hydrodynamic radius (R_h) sizes of 3F and nPM during the hydrolysis and condensation process at pH 2.0. Arrows indicate the time when samples were taken for the amyloid study.

Figure 3-2 shows the 3D structure and space-filling model of the NPs growth of 3F, which could start from 1 nm size and continue to grow. These polymeric NPs can grow linearly or branchwise to form spherical particles, but still contain silanol functionality, as shown by the 3D model structure of the NPs.

OH-

OH-

≈1 nm
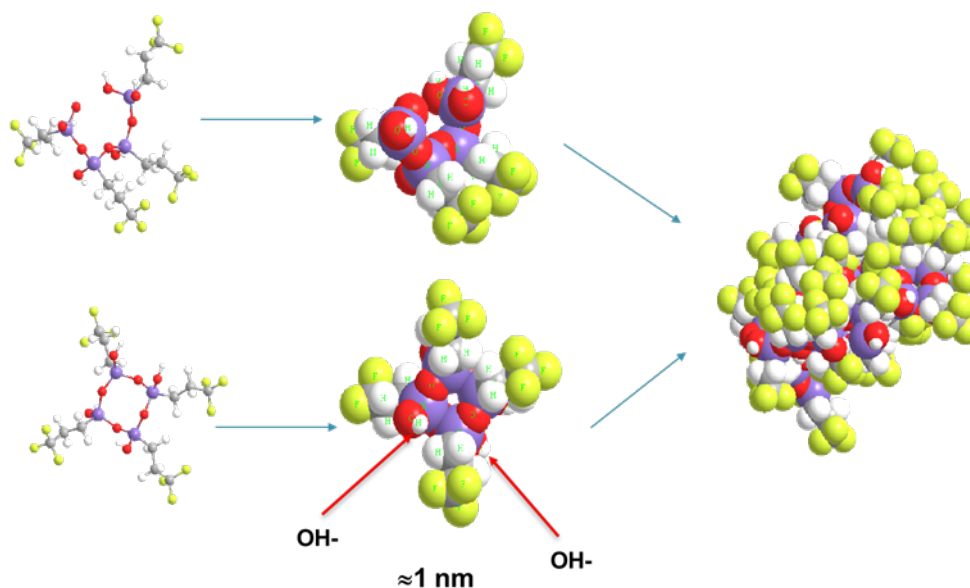
Figure 3-2. Schematic of the 3D structure and space filling model for fluorinated polymeric NPs, suggesting that both linear and cyclic geometries are possible, and silanol as well as 3F moieties are present on the NP surface for interaction with proteins.

DLS has been widely used to determine the proteins and their fibril sizes in solution. In this study, DLS was used to determine the hydrodynamic diameter of the protein, fibrils, fluorinated and methylated polymeric NPs, and the composite particles formed as the fibril inhibition process completed. Amyloid fibril inhibition study was performed using NPs formed at the very early stage of the condensation of 3F and nPM, shown as arrow in Figure 3-1, where NPs are in their smallest sizes. At this stage, along with the newly formed polymeric 3F and nPM NPs, their free hydrolyzed 3F and nPM monomers may also be available. These hydrolyzed monomers may also take part in the amyloid inhibition process, as these monomers favor transition of beta-sheets into alpha-

helices. The DLS study gives a comparative picture of the hydrodynamic sizes of the

products generated, observed after treating BLG with fluorinated and methylated
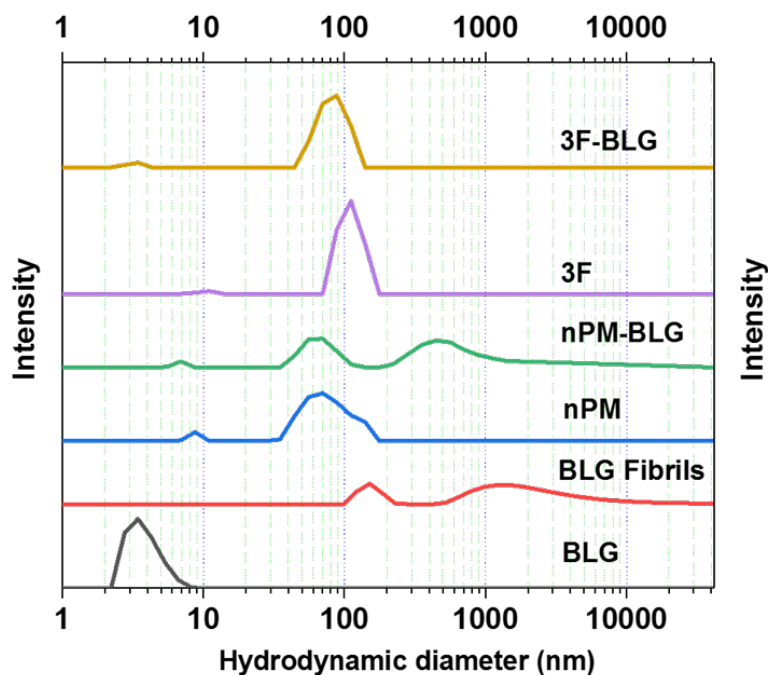
polymeric NPs.

Figure 3-3. Hydrodynamic diameter of BLG, fibrillated BLG, fluorinated and methylated polymeric NPs treated BLG, and control fluorinated and methylated polymeric NPs. The fibrillation of BLG was performed at 90°C for 5 h in DLS cuvette. Fluorinated and methylated polymeric NPs were added in BLG (0.272 mM), and reacted for 5 min before heating at 90°C for 5 h at pH 2.0.

Figure 3-3 shows the hydrodynamic diameter of BLG, potential BLG fibrils, and

evolved NPs during the amyloid inhibition process, using fluorinated and methylated

polymeric NPs. The hydrodynamic diameter of BLG was observed as 4 nm at pH 2, and after heating at 90°C for 5 h fibrils formed with a bimodal size distribution with peaks at 150 nm and 1μm. Bolisetty et al. conducted an experiment on the kinetic of the BLG fibrillation, and observed similar bimodal fibril size distribution at 90°C. (79)

Hydrodynamic diameter of fluorinated and methylated polymeric NPs treated BLG showed distinct size distribution compared to the control or untreated NPs. Bimodal size distributions were observed for both the particles formed after 3F NPs treated with BLG and untreated control NPs; but sizes reduced after 3F NPs (3±1 nm and 85±7 nm) were treated with BLG, compared to the control NPs (19±2 nm and 110±10 nm). Hydrodynamic diameter of nPM NPs treated BLG showed tri-modal size distribution (7±1 nm, 60±3 nm and 500±40 nm), compared to the bimodal sized distribution (9±1 nm, 70±5 nm) of their control NPs. The reduction in the sizes observed after 3F NPs treated BLG indicates the fibril inhibition, which was not observed in the case of nPM NPs treated BLG. This reduction in size also indicates the possible termination of the NPs' growth as they interact with BLG molecules. The appearance of the particles with the size of 500±40 nm during the nPM NPs interaction with BLG indicates the possibility of fibril formation.

Fluorescent dye such as ThT is widely used to determine the formation of protein fibrils during the amyloid aggregation process. (80-90) When ThT reacted with fibrillated protein, a specific binding between ThT and the β-sheet structure of fibrils

formed, which enhanced the fluorescent intensity of ThT, indicating the presence of

fibrils. In this study, ThT fluorescence-based method was used to identify the fibrils in

the fluorinated and methylated polymeric NPs treated BLG solution. The spectrum

representing the BLG fibril-ThT in Figure 3-4 (a) and (b) shows that the fluorescence

intensity doubled, compared to the spectrum of nonfibrillated BLG-ThT, which confirms

the existence of fibrils.
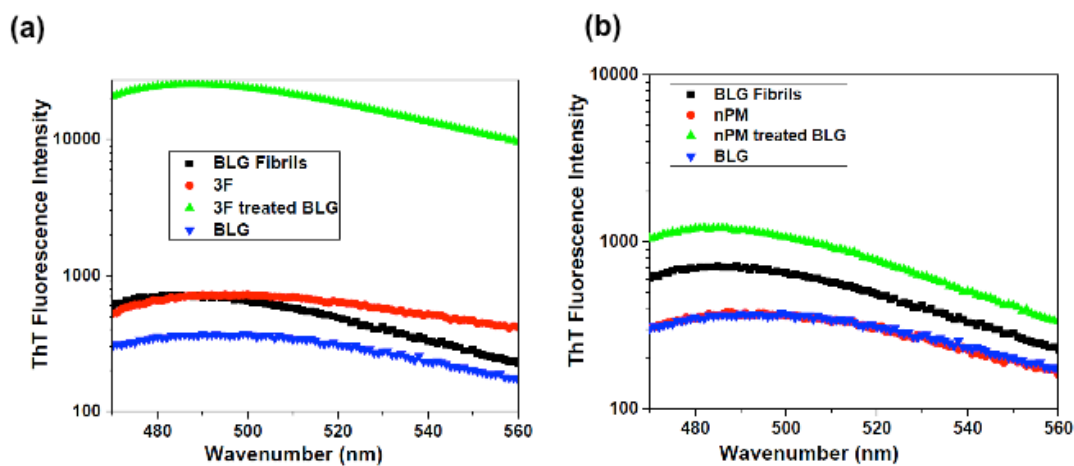
Figure 3-4. Emission spectra of ThT fluorescence obtained from (a) fluorinated and (b) methylated polymeric NPs treated BLG, along with fibrillated, nonfibrillated BLG, and their controls.

Although the spectrum of nPM-ThT was observed identical to that of

nonfibrillated BLG-ThT, the intensity of the spectrum representing 3F-ThT increased.

The 3F NPs treated BLG-ThT emission spectrum was 70 times and nPM NPs treated

BLG-ThT was 3 times higher in fluorescence intensity, compared to that of nonfibrillated

BLG-ThT. A comparative picture of the fluorescence intensity at 485 nm taken from all the emission spectra of nonfibrillated BLG-ThT, fibrillated BLG-ThT, nPM-ThT, 3F-ThT and 3F and nPM NPs treated BLG-ThT is shown in Figure 3-5. Fluorescence intensity was taken at 485 nm because intensities of all the spectra are observed as optimum at this wavelength.
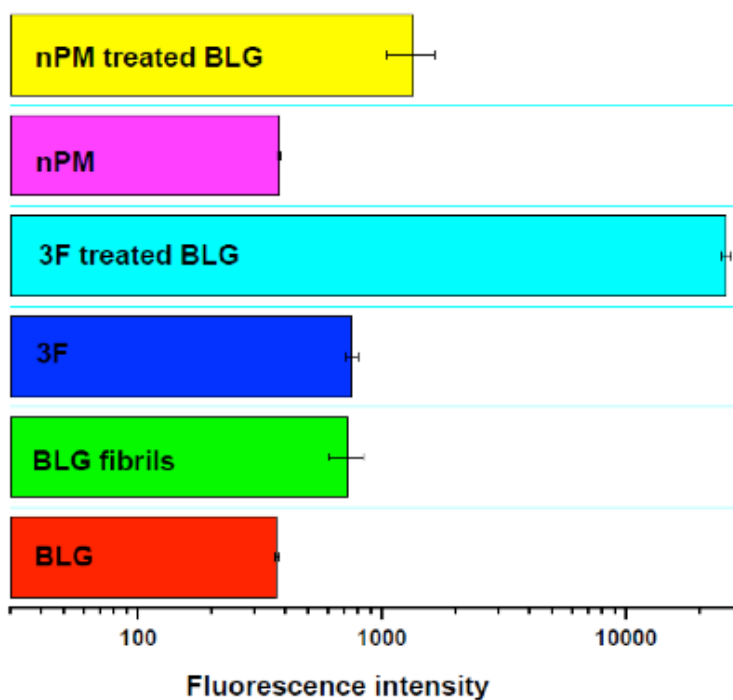
Figure 3-5. Comparison of ThT fluorescence intensity of fluorinated and methylated polymeric NPs treated BLG along with fibrillated and nonfibrillated BLG (0.272 mM), and their controls at 490 nm.

As fluorinated and methylated polymeric NPs are expected to inhibit the fibrillation of BLG, increased fluorescence intensity could mean inefficiency in

fibrillation inhibition. But a recently published report showed that ThT can bind with silica gel and generate very high fluorescence. D'Amico et al. observed ThT entrapped in the silica xerogel, resulting in high fluorescence intensity, compared to the free ThT molecule. (91) The electrostatic interaction between positive ThT and negative $\equiv SiO^-$ groups creates a very strong ThT^+-SiO^- bond, immobilizing ThT molecules inside the pores of the xerogels. This electrostatic interaction strongly hinders the rotational mobility of the ThT, increasing its overall fluorescence intensity. During the amyloid inhibition process, fluorinated and methylated polymeric NPs went through the continual condensation process, generating fluorinated and methylated silica colloids and BLG-silica composite colloids. These colloids contain a large number of $\equiv SiO^-$, which potentially could interact with positively charged ThT, resulting in enhanced fluorescence intensity. Thus, lower fluorescence intensity of BLG fibrils, compared to 3F and nPM treated BLG, could be due to the interaction between ThT and 3F-BLG / nPM-BLG composites instead of BLG fibrils. Thus, success in inhibition of fibrillation by fluorinated and methylated polymeric NPs is not distinguishable with these ThT fluorescence spectra.

The fluorescence intensity of ThT after interacting with fluorinated and methylated polymeric colloids shown in Figure 3-5 was much lower, relative to the fluorescence intensity observed with 3F-BLG / nPM-BLG composites. This could be due to the fact that the sample used from the 3F and nPM condensed solution might not have

enough colloids in the sample interacted with ThT, since colloids tend to precipitate as condensation continues. This also means that 3F-BLG / nPM-BLG composites tend to remain suspended in solution for a longer time, compared to the fluorinated and methylated polymeric NPs.

To have a comprehensive idea of the structures of protein fibrils, colloidal particles and nanocomposites, nanoscopic image analysis was used. AFM is widely used to observe the amyloid fibrils formation and analyze their structural properties. (65-68) In this study, AFM images were taken to investigate the nanoscopic development in BLG during the inhibition process by fluorinated and methylated polymeric NPs. Figure 3-6 shows the AFM images of untreated BLG, fluorinated and methylated polymeric NPs treated BLG, along with the 3F and nPM associated NPs. Unheated BLG created a thin layer of 2 nm on the mica surface (Figure 3-6 (a)) at pH 2.0; and after heated at 90°C for 5 h, BLG formed fibrils with various lengths and shapes (Figure 3-6 (b)). Figure 3-6 (c) shows that two different NP-size groups were generated in the controlled system of 3F, which were consistent with the DLS-obtained data described earlier. Fluorinated polymeric NPs treated BLG showed no fibrils presence, but rather spherical NPs with two distinct size groups of NPs, as shown in Figure 3-6 (d).
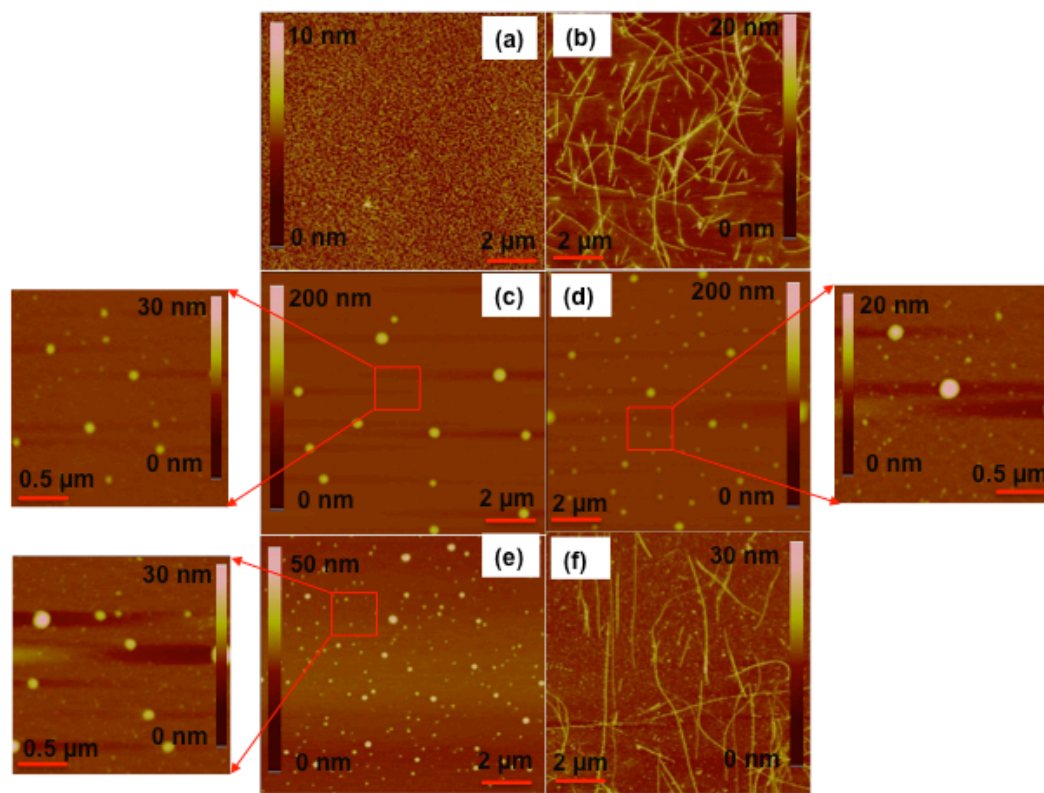
Figure 3-6. AFM images of (a) BLG (0.272 mM), (b) fibrillated BLG (0.272 mM), (c) evolved particles after heating fluorinated polymeric NPs, (d) particles formed after fluorinated polymeric NPs reacted with BLG (0.272 mM) for 5 min and then heated, (e) evolved particles after heating methylated polymeric NPs, and (f) particles formed after methylated polymeric NPs reacted with BLG (0.272 mM) for 5 min and then heated.

These results confirm the amyloid inhibition by fluorinated polymeric NPs and associated NPs generated during the inhibition process. The NPs generated during the amyloid inhibition process are relatively monodispersed compared to the NPs generated due to condensation of fluorinated polymeric NPs alone. These monodispersed NPs could be the composite material consisting of both 3F and BLG or only 3F.

Unlike fluorinated polymeric NPs treated BLG, fibrils were generated when BLG was treated with methylated polymeric NPs. However, these fibrils were thinner, relatively longer in size, and fewer in number, compared to the untreated BLG fibrils shown in Figure 3-6 (e) and (f). Along with fibrils, relatively small sized NPs were also observed, which could be composite materials consisting of nPM and BLG or simply NPs generated from the condensation of nPM.

To analyze the length, size, and number of the BLG fibrils, composite NPs of 3F and nPM with BLG and their non-composite NPs were generated during the amyloid fibril inhibition process, and a series of histograms were plotted based on the AFM images shown in Figure 3-7.
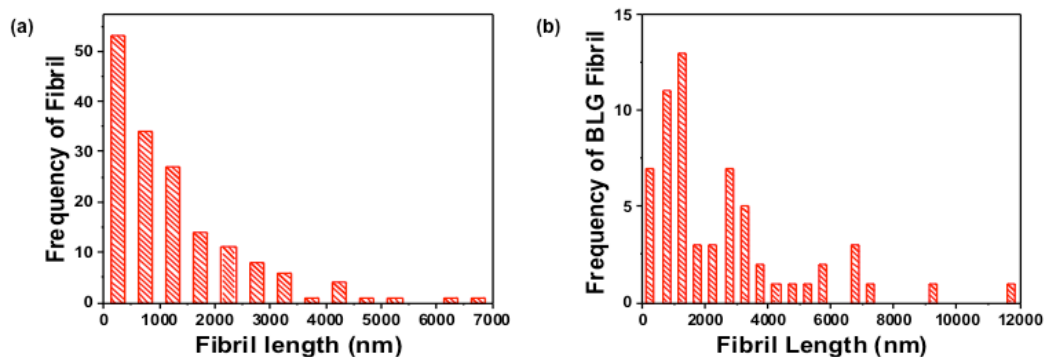
Figure 3-7. Histograms of the sizes of the (a) BLG fibrils formed at 90°C for 5 h, and (b) BLG fibrils formed after methylated polymeric NPs reacted with BLG (0.272 mM) and then heated.

The histogram of BLG fibrils showed that around 50±5 fibrils were <0.5 μm in length, and the majority of the fibrils were larger than 2 μm but smaller than 5 μm (Figure 3-7 (a)). No fibril was formed when BLG was treated with fluorinated polymeric NPs, but when treated with methylated polymeric NPs, fibrils were formed. These fibrils were fewer in number, compared to the untreated BLG fibrils (Figure (3-7 (b)).

The histogram of nPM treated BLG also showed that few fibrils were below 0.5 μm, but the overall size of the fibril length increased, compared to the untreated BLG fibrils; and the longest fibril was measured as >12 μm.
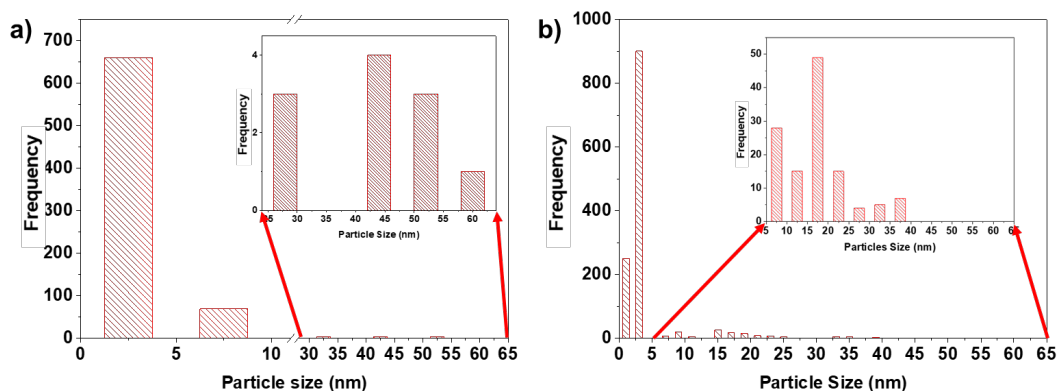
Figure 3-8. Histograms of the sizes of the (a) evolved particles after heating fluorinated polymeric NPs at 90°C for 5 h, and (b) particles formed after fluorinated polymeric NPs reacted with BLG (0.272 mM) for 5 min and were then heated at 90°C for 5 h. The insert in the Figures shows the amplified frequency of the indicated particle size zones.

The histograms of the NPs generated from the fluorinated and methylated polymeric NPs used in the fibrillation inhibition process are shown along with the NPs

generated from the control 3F and nPM NPs in Figures 3-8 and 3-9. Figure 3-8 (a) shows

that NPs generated from fluorinated polymeric NPs after heating for 5 h at 90°C were

mostly below 5±1 nm in diameter, and some ranged from 30±2 nm to 60±2 nm, which

were obtained from the height profile from the AFM images. But as 3F NPs were used in

the inhibition process against BLG, NPs sizes decreased, as shown in Figure 3-8 (b),

where the majority of NPs ranges below 4 nm and in the range between 10±2 to 40±5

nm, with a bimodal distribution.
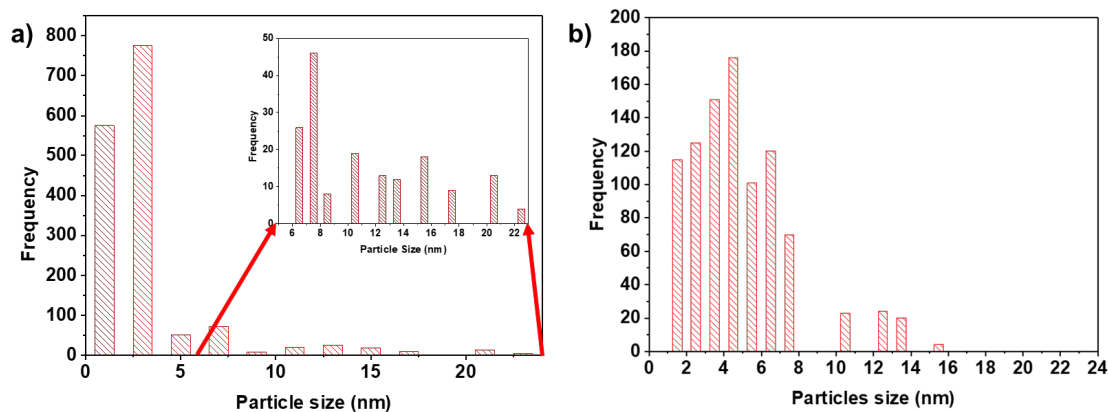
Figure 3-9. Histograms of the sizes of the (a) evolved particles after heating methylated polymeric NPs at 90°C for 5 h, (b) particles formed after methylated polymeric NPs reacted with BLG (0.272 mM) for 5 min, and then heated at 90°C for 5 h.

This decrease in size indicates that the BLG interacting 3F NPs were restricted in

growth. Similar to the fluorinated polymeric NPs, the histogram of the particles generated

from the methylated polymeric NPs used to inhibit the BLG fibrillation showed decrease

in sizes and number, compared to the NPs generated from control nPM, shown in Figure 3-9 (a) and (b). Although methylated polymeric NPs did not inhibit the fibril growth of BLG, this histogram showed that it interacted with BLG, which hindered the further growth of the methylated polymeric NPs.

As the AFM images show, the fibrils and NPs generated from fluorinated and methylated polymeric NPs after the inhibition process were distinct in size, shape, and length, compared to the untreated BLG fibrils, fluorinated and methylated polymeric NPs; and a cross-sectional analysis gives further understanding of their structural formation, as shown in Figure 3-10.

The height profiles obtained from the cross-section of the AFM images of BLG fibrils are shown in Figure 3-10 (a) and fluorinated and methylated polymeric NPs treated BLG and associated NPs are shown in Figure 3-10 (b) and (c), respectively. The height of the BLG fibrils ranged from 2±0.5 nm to 12±1 nm, where the majority were between 4±0.5 nm to 6±1nm, and these numbers were consistent with published reports. (65)
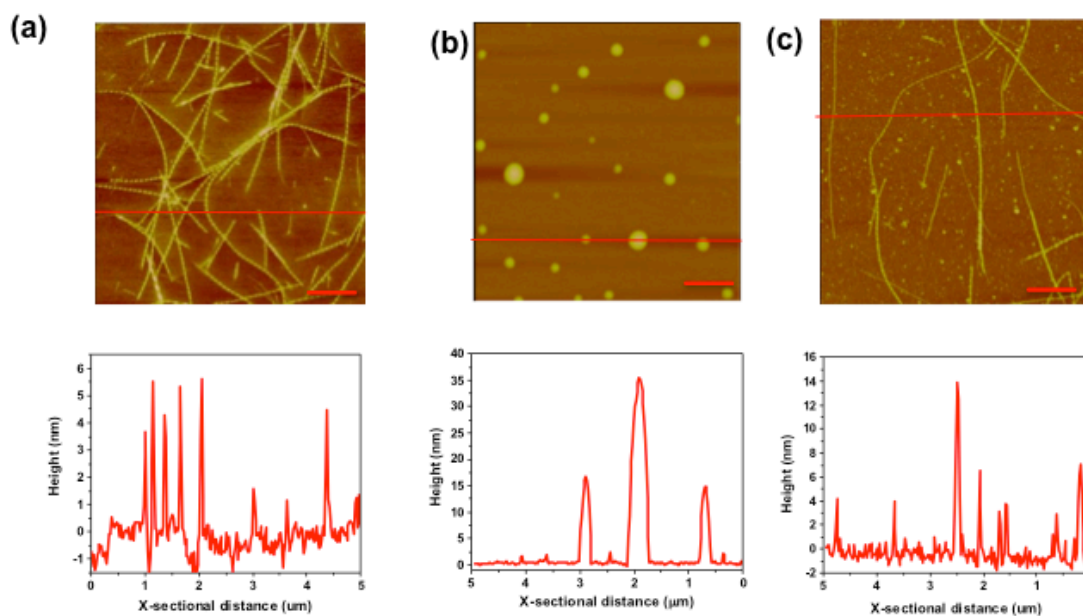
Figure 3-10. Height profile of (a) BLG fibrils (0.272 mM), (b) 3F-BLG composite NPs formed after fluorinated polymeric NPs reacted with BLG (0.272 mM) for 5 min and then were heated, and (c) BLG fibrils and nPM-BLG composite NPs formed after methylated polymeric NPs reacted with BLG (0.272 mM) for 5 min and then were heated.

The height of the NPs generated after the fluorinated polymeric NPs interacted with BLG in the inhibition process ranged from 5±1 nm to 35±5 nm. The height of the fibrils generated after the methylated polymeric NPs interacted with BLG mostly ranged from 8±1 nm to 12±1 nm, which was higher than the untreated BLG fibrils. Also, the NPs generated during this process had similar width / diameter as described earlier, while their height ranged from 15±1 nm to 20±2 nm.

Adamcik et al. described the structural formation of the BGL fibrils based on the periodicity of the pitch in various fibrils observed in AFM obtained images. (65, 67)

Figure 3-11 shows the longitudinal cross-section of the BLG fibrils analyzed with a Nanoscale analyzer. Untreated BLG fibrils showed four types of periodicity (p) in the pitch, such as 70±8 nm, 160±10 nm, 200±15 nm, and 320±20 nm (Figure 3-11 (a)). Three of these four types of periodicities had fibrils height of 4±0.5 nm, 6±0.5 nm, and 8±1 nm, which represent 2, 3, and 4 individual fibrils getting together in twisted formation. However, one of the fibrils had a little different structural formation than the twisted shape fibrils, and with a 10±1 nm height and periodicity of 320±20 nm, it formed more helical-shaped fibrils. As these fibrils turned into helical shapes, their periodicity was half of the obtained 320 nm.

Based on the obtained periodicities and fibril heights, 3D models representing all the fibril structures are shown on the left side of Figure 3-11 (a). The untreated BLG fibrils' structural morphologies were consistent with already published reports. Figure 3-11 (b) shows the cross-section of the fibrils that formed after methylated polymeric NPs interacted with BLG. These fibrils had different types of heights, but no distinct periodicity could be observed in any of the fibrils. This indistinct periodicity may imply that the methylated polymeric NPs treatment of BLG helped individual fibrils to compile together with more internal structural induction, such as increased β-sheet, which ultimately lead to the formation of a nanotube-type fibril structure. A 3D model is shown in the right side of Figure 3-11 (b), representing the fibril nanotube.
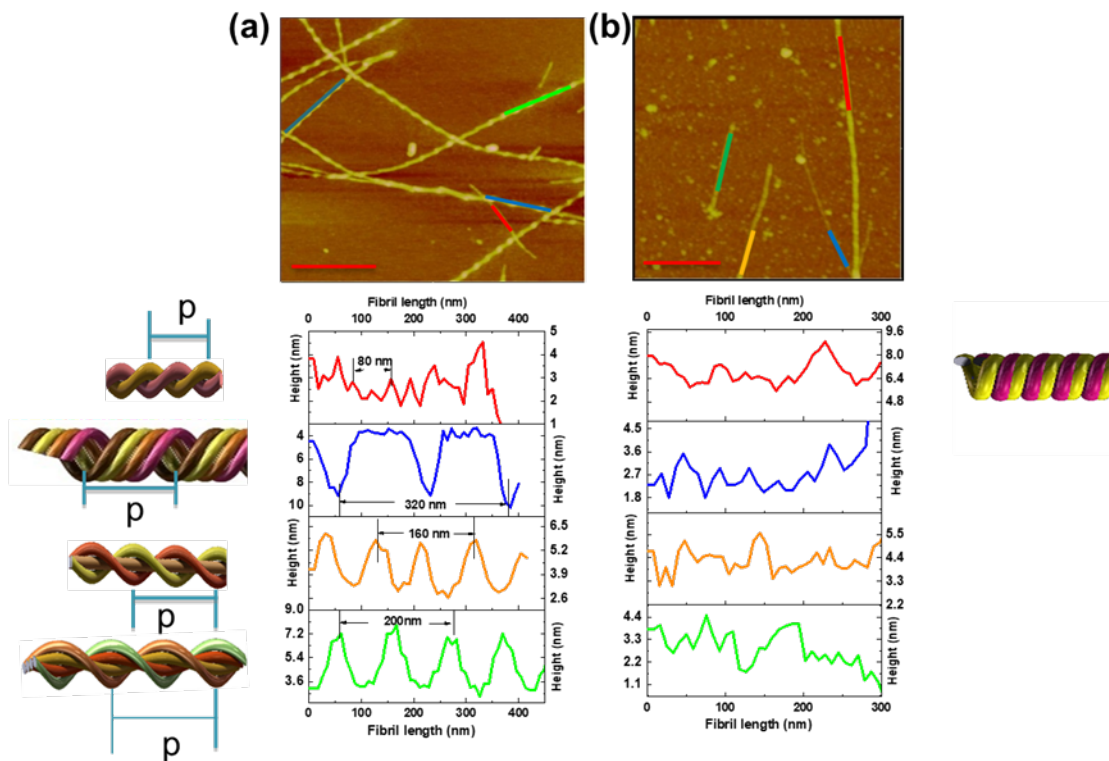
Figure 3-11. Longitudinal height profiles and pitch periodicities of (a) BLG (0.272 mM) fibrils, and (b) methylated polymeric NPs treated BLG fibrils. 3D structures show the possible structural formation for fibrils, based on the longitudinal height profile and the fibrils' pitch periodicities.

Based on the DLS and AFM analyzed data, a schematic representing possible formations of fibrils and associated NPs during the fibrillation inhibition process is shown in Figure 3-12.
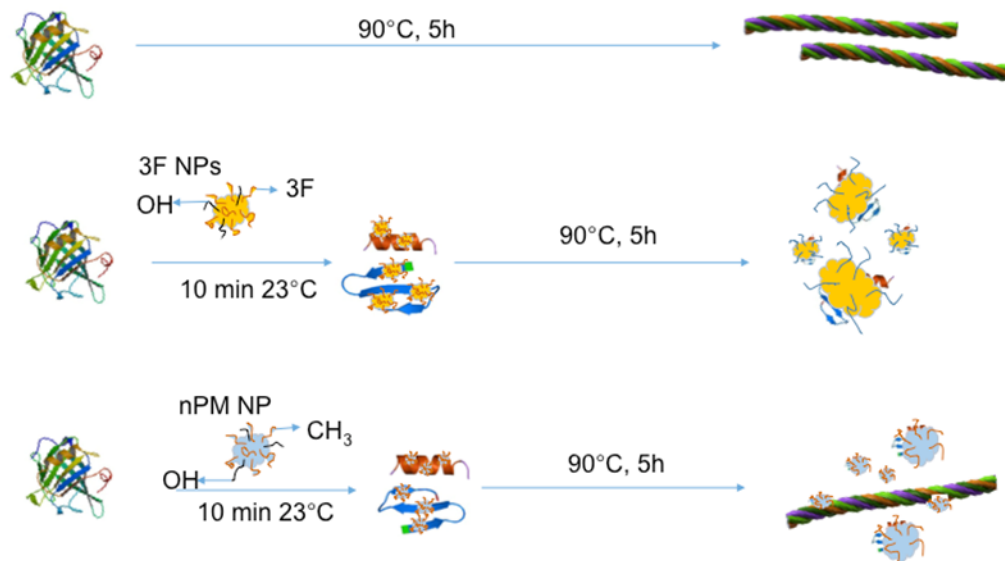
Figure 3-12. Schematic representations of protein fibrillation processes and inhibition, using fluorinated and methylated polymeric NPs against BLG.

ATR-FTIR is widely used to analyze the transformations that occur in protein secondary structures. (75, 92-94) Figure 3-13 shows the ATR-FTIR spectra of the nanocomposites generated after the amyloid inhibition process, along with the fibrillated and nonfibrillated BLG. Two amide peaks, amide I at 1725-1600 cm^{-1}, and amide II at 1525-1550 cm^{-1}, were visible in all four spectra, such as BLG, fibrillated BLG, 3F treated composite NPs, nPM treated BLG fibrils and associated NPs. Another major peak at 1725 cm^{-1} was also visible in all spectra. Vibration in this region represents the protonated carboxyl groups of aspartic and glutamic residues. (75)
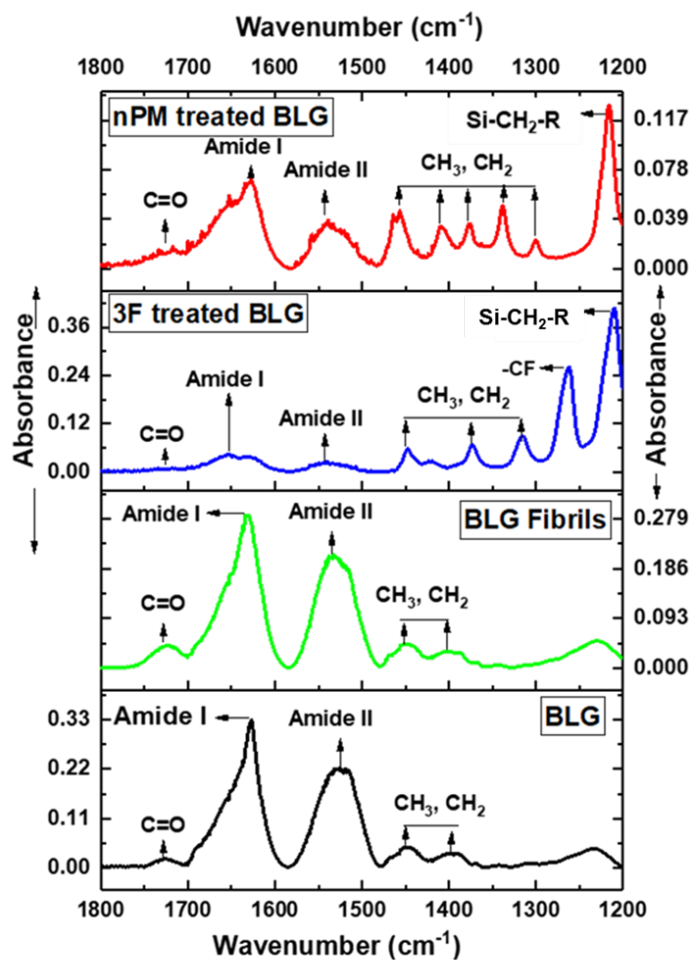
Figure 3-13. ATR-FTIR spectra of BLG (0.272 mM), BLG (0.272 mM) fibrils, 3F and nPM NPs treated BLG (0.272 mM).

Increase in the intensity of this peak implies more exposure of the backbone carboxyl groups, potentially through backbone cleavage. (75) The FTIR spectral zone representing CH_3 and CH_2 (1300-1480 cm^{-1}) showed the presence of additional peaks in the fluorinated and methylated polymeric NPs treated BLG products, compared to both

the fibrillated and nonfibrillated BLG. These additional peaks were due to the presence of nPM and 3F functionality in the post inhibition process products. The presence of –CF peak at 1250 cm^{-1} and Si-CH$_2$-R peak at 1210 cm^{-1} increases the possibility of having the combination of BLG and fluorinated silica particles present in the composite NPs.

The fibrillated BLG spectrum showed that the absorbance intensity of the two amide peaks at 1625 cm^{-1} (amide I) and 1525 cm^{-1} (amide II) were reduced, but these two amide regions widened in wavenumber, compared to the nonfibrillated BLG, indicating structural transformation of BLG as fibrillation occurred. Also, increments in the intensity of peak at 1725 cm^{-1} confirmed the fibril formation of BLG as structural transition occurred. (75) The spectrum representing fibrils and associated NPs generated after the interaction of BLG and methylated polymeric NPs showed that the absorbance intensity reduced drastically in both the amide zones, and amide I peak at 1625 cm^{-1} broke into three smaller peaks. Also, the increments in the intensity of the protonated carboxyl peak at 1725 cm^{-1} represented the presence of fibrillated BLG. Similarly, the spectrum representing the nanocomposites generated after fluorinated polymeric NPs interacted with BLG also showed reduction in two amide peaks, but unlike breaking into smaller peaks, amide I peak at 1625 cm^{-1} shifted to 1650 cm^{-1}. The transition in the major peaks in the spectra can be concluded as a major conformational transformation in the secondary structure during the fluorinated and methylated polymeric NPs treatment of BLG.

For better understanding of the possible conformational changes in the secondary structures of BLG after the inhibition process, FTIR spectra in the amide zones were deconvoluted. Secondary structures are shown as numbers in the amide I zone (1600 cm^{-1} to 1700 cm^{-1}), and this zone was selected because it was observed as the most sensitive part of the spectra, where possible conformation change may occur.
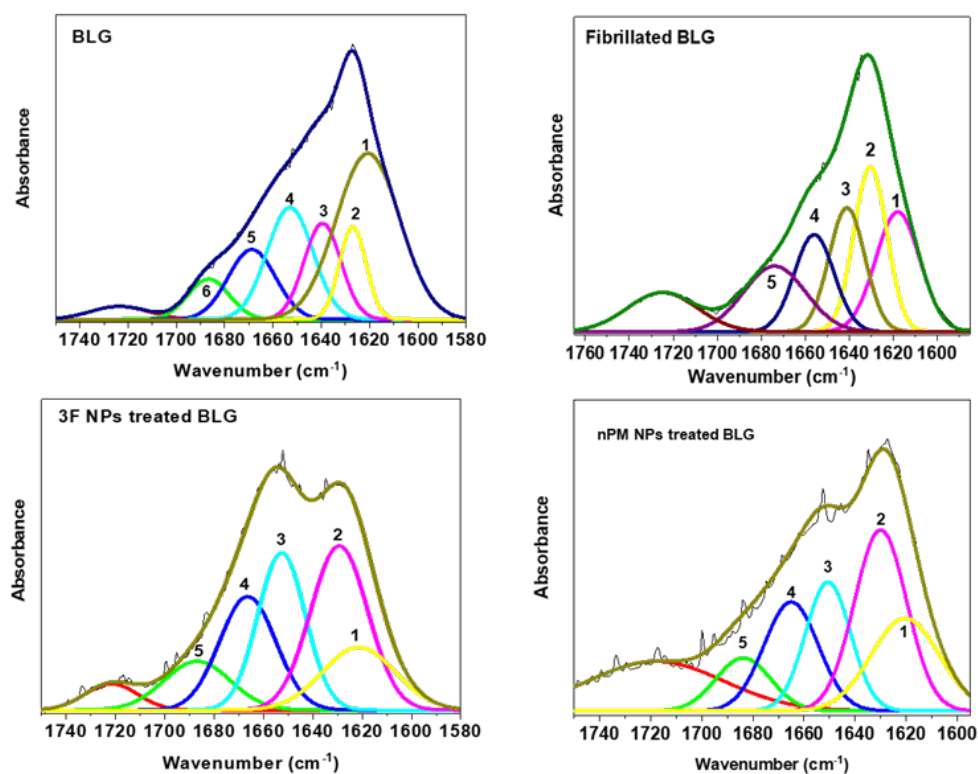
Figure 3-14. Deconvoluted ATR-FTIR spectra of BLG (0.272 mM), BLG (0.272 mM) fibrils, 3F and nPM NP treated BLG (0.272 mM). Individual peaks between 1600 cm^{-1} to 1700 cm^{-1} are numbered.

Figure 3-14 shows the individual deconvoluted peaks that represent different types of

protein secondary structures such as α-helix (1654±2 cm^{-1}), β-sheet (1612-1650 cm^{-1} and

1691±2 cm^{-1}), β-turn (1666-1687 cm^{-1}), and 3$_{10}$-helix (1663±3 cm^{-1}). (92, 94) All the

deconvoluted peaks for the secondary structures are shown in numbers in all the spectra

in Table 3-1.

Table 3-1. Deconvoluted components of the secondary structures of BLG (0.272 mM), BLG (0.272 mM) fibrils, 3F and nPM treated BLG (0.272 mM) obtained from Figure 3-14.

Wavenumber (cm^{-1})	Assigned structure	Deconvoluted components			
		BLG	BLG Fibril	3F NPs treated BLG	nPM NPs treated BLG
1621±3	β-sheet	1	1	1	1
1627±2	β-sheet	2		2	
1633±2	β-sheet		2		2
1642±1	β-sheet	3	3		
1648±2	Random				3
1656±2	α-helix	4	4	3	
1663±3	3$_{10}$-helix				4
1667±1	β-turn	5		4	
1680±2	β-turn		5		5
1685±2	β-turn	6		5	

From Table 3-1, it can be observed that the α-helix structure disappeared after the methylated polymeric NPs treated BLG, and it turned into random secondary structure and 3_{10}-helical structure.

The secondary structures were identified from the deconvoluted spectra, and individual spectral areas were calculated. Comparative data of the conformational change of the secondary structures β-sheet and α-helix were calculated based on the % area of individual peaks obtained from the spectra is shown in Figure 3-15.
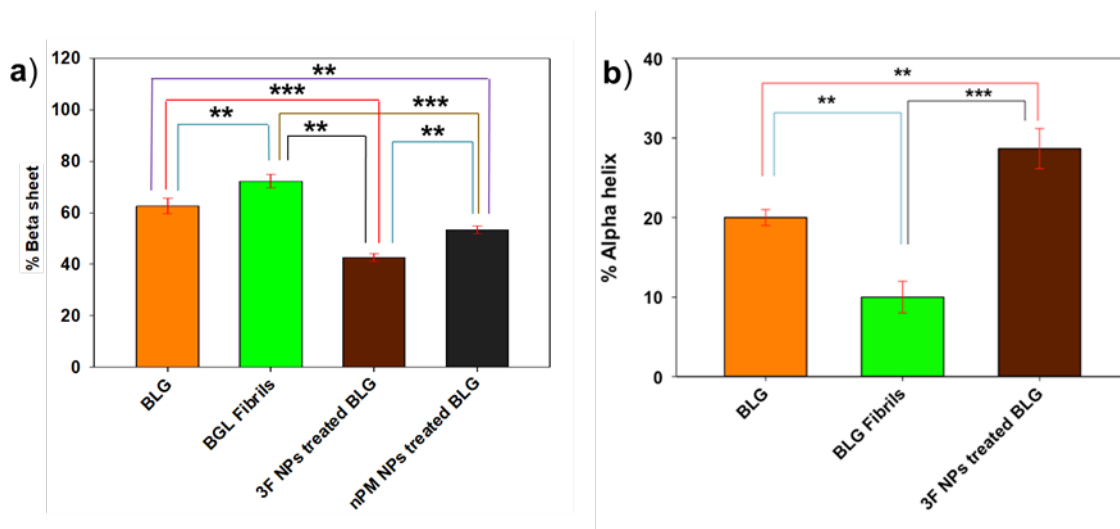
Figure 3-15. Comparative β-sheet (a) and α-helix (b) % of BLG, fibrillated BLG, 3F and nPM treated BLG. P value obtained after performing one-way ANOVA test. **, and *** represent P value ≤ 0.01 and ≤ 0.001, respectively, obtained after performing one-way ANOVA test among the samples.

Analyzed data shows that β-sheet increased by 11 % and α-helix decreased by 9 % in the fibrillated BLG, compared to the nonfibrillated BLG. These increases in the β structures were expected, since they are responsible for the formation of fibrils. Increased β-sheet and decreased α-helix imply that α-helix is transformed into β structures.

The fibrils and associated NPs generated after interaction of methylated polymeric NPs with BLG showed disappearance of the α-helix structure and 7 % reduction in the β-sheet structure, which eventually converted to random secondary structures and 3_{10}-helical structures. A different picture was observed with data obtained from the fluorinated polymeric NPs treated BLG nanocomposites, where β-sheet decreased by 29 % and α-helix increased by 10 %, which confirmed the β-sheet induction by the fluorinated polymeric NPs. Figure 3-15 shows the comparative plotting of the β-sheet % (Figure 3-15 (a)) and α-helix % (Figure 3-15 (b)) in each individual case, with one-way ANOVA analysis indicating that the observed conformation shifts are significant.

BLG reportedly has three potential binding sites for ligand binding: 1) internal β-barrel cavity, 2) surface hydrophobic pocket in a groove between α -helix and β-barrel, and 3) outer surface near Trp19-Arg124. (95-100) To examine the binding mode of fluorinated and methylated polymeric NPs at the active site of BLG and how they may affect the conformation of BLG, docking simulations were carried out using AutoDock,

but due to fluorinated and methylated polymeric NPs size constrains, only monomeric

hydrolyzed forms of both 3F and nPM or silanols were used.
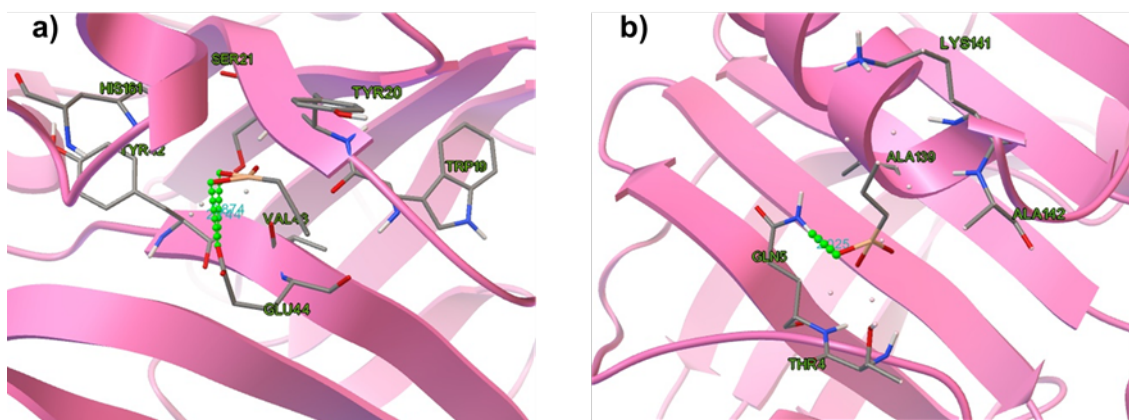
Figure 3-16. Predicted modes of binding between (a) fluorinated and (b) methylated silanol with BLG at the lowest binding energy. Hydrogen bonds are marked as a line of green dots.

During the docking, a maximum number of 10 conformers were considered, and

the lowest energy conformation was used for further analysis. Docking results showed

that both 3F and nPM were located in the β-domain, as shown in Figure 3-16 (a), and (b).

On the basis of Figure 3-16, the interacting residues of possible binding patterns

and properties resulting from the bindings are listed in Table 3-2. The docking results

showed that fluorinated silanol binds to the surface of BLG by two hydrogen bond

interactions with GLU44. The predicted binding site for fluorinated silanol on BLG was

clustered around residues such as HIS161, SER21, TYR20, TYR42, GLU44 and VAL45.

There were two hydrogen bonds between H3F and ILE, with the distance of 2.874 Å and

2.744 Å.

Table 3-2. Dock scores and summary of molecular interaction between fluorinated and methylated silanols and BLG.

Interacting molecules	Intermolecular energy (Kcal/mol)	Torsional energy (Kcal/mol)	Binding energy (Kcal/mol)	No of H-bonds	Residues of H-bonds	Residues of inteaction
nPM NPs-BLG	-4.88	1.79	-3.09	1	GLN5	GLN5, ALA139, LYS141, ALA142, THR4
3F NPs-BLG	-5.07	1.49	-3.58	2	Glu44 (contain 2 H-bonds)	HIS161, SER21, TYR20, TYR42, TRY20, GLU44, VAL45

Similarly, the predicted binding site for methylated silanol on BLG was clustered

around residues such as GLN5, ALA139, LYS141, ALA142, and THR4. The docking

results showed that methylated silanol binds to the surface of BLG by one hydrogen bond

interactions, and these hydrogen bonds occurred between methylated silanol with GLN5,

with distance of 2.021 Å. 3F and nPM bonded with hydrophobic amino acids of BLG,

where the hydroxyl group acted as hydrogen bond donor. Thus, it can be concluded that

the interaction of the hydroxyl groups in the structure of fluorinated and methylated

polymeric NPs with BLG has a significant role in the binding process, which eventually

takes part in inhibiting and prohibiting the amyloid fibril process.

3.6 Conclusion

This study demonstrated the amyloid inhibition behavior of fluorinated and methylated polymeric silane NPs against a globular protein, BLG. The hydrolysis and condensation profiles of both silanes were determined using DLS, in order to control particle size and reactivity. After initial confirmation of the amyloid inhibition capability of fluorinated polymeric NPs by DLS and fluorescence data, detailed structural information was obtained by AFM. The AFM-based study showed the complete inhibition of amyloid fibrils growth by fluorinated polymeric NPs, but there was no inhibition by methylated polymeric NPs. Later, ATR-FTIR study showed transformation in the secondary structure of BLG during the inhibition process, where it showed that decrease in β structures occurred due to interaction between fluorinated polymeric NPs and BLG. Expectedly, the percentage of β structures increased during the interaction between methylated polymeric NPs and BLG, since the AFM image showed that methylated polymeric NPs promoted amyloid formation. Lastly, a molecular docking study confirmed that free silanols were involved through hydrogen with protein residues for both silanes. The successful amyloid inhibition ability of fluorinated polymeric NPs showed the potential use of these NPs as nanotherapeutic agents against amyloid diseases. In the future, a comprehensive study on the use of these fluorinated polymeric NPs against various amyloid-based diseases should be explored.

3.7 References

1. Toyama, B. H.; Weissman, J. S. *Annu. Rev. Biochem.* **2011**, *80*, 557.

2. Dobson, C. M. *Nature* **2003**, *426*, 884.

3. Caughey, B.; Lansbury, P. T. *Annu. Rev. Neurosci.* **2003**, *26*, 267.

4. Nelson, R.; Sawaya, M. R.; Balbirnie, M.; Madsen, A. ∅.; Riekel, C.; Grothe, R.; Esenberg, D. *Nature* **2005**, *435*, 773.

5. Chiti, F.; Dobson, C. M. *Annu. Rev. Biochem.* **2006**, *75*, 333.

6. Chiti, F.; Dobson, C. M. *Nat. Chem. Biol.* **2009**, *5*, 15.

7. Knowles, T. P.; Fitzpatrick, A. W.; Meehan, S.; Mott, H. R.; Vendruscolo, M.; Dobson, C. M.; Welland, M. E. *Science* **2007**, *318*, 1900.

8. Sandal, M.; Valle F.; Tessari, I.; Mammi, S.; Bergantino, E.; Musiani, F.; Brucale, M.; Bubacco L.; Samori, B. *PLoS Biol.* **2008**, *6*, e6.

9. Sunde, M.; Blake, C. C. *Q. Rev. Biophys.* **1998**, *31*, 1.

10. Ohnishi, S.; Takano, K. *Cell. Mol. Life Sci.* **2004**, *61*, 511.

11. Kagan, B. L.; ThunDImadathil, J. *Adv. Exp. Med. Biol.* **2010**, *677*, 150.

12. Palmer, A. M. *Trends Pharmacol. Sci.* **2011**, *32* (3), 141.

13. Ono, K.; Hasegawa, K.; Naiki, H.; Yamada, M. *J. Neurosci. Res.* **2004**, *75*, 742.

14. Yang, F.; Lim, G. P.; Begum, A. N.; Ubeda, O. J.; Simmons, M. R.; Ambegaokar, S. S.; Chen, P.; Kayed, R.; Glabe, C. G.; Frautschy, S. A.; Cole, G. M. *J. Biol. Chem.* **2005**, *280*, 5892.

15. Garcia-Alloza, M.; Borrelli, L. A.; Rozkalne, A.; Hyman, B. T.; Bacskai, B. J. *J. Neurochem.* **2007**, *102*, 1095.

16. He, J.; Wang, y.; Chang, A. K.; Xu, L.; Wang, N.; Chong, X.; Li, H.; Zhang, B; Jones, G. W.; Song, Y. *J. Agric. Food Chem.* **2014**, *62* (39), 9442.

17. Kai, T.; Zhang L; Wang X.; Jing A.; Zhao B.; Yu X.; Zhou F. *ACS Chem. Neurosci.* **2015**, *6* (6), 879.

18. Zhang, C.; Browne, A.; Child, D.; Tanzi, R. E. *J. Biol. Chem.* **2010**, *285*, 28472.

19. Stains, C. I.; Mondal, K.; Ghosh, I. *ChemMedChem.* **2007**, *2*, 1674.

20. Austen, B. M.; Paleologou, K. E.; Ali, S. A. E.; Qureshi, M. M.; Allsop, D.; El-Agnaf, O. M. A. *Biochemistry* **2008**, *47*, 1984.

21. Frydman-Marom, A., Rechter, M., Shefler, I., Bram, Y., Shalev, D. E., Gazit, E. *Angew. Chem., Int. Ed.* **2009**, *48*, 1981.

22. Vilasi, S.; Iannuzzi, C.; Portaccio, M., Irace, G.; Sirangelo, I. *Biochemistry* **2008**, *47*, 1789.

23. Yu, W.-B.; Jiang, T.; Lan, D. M.; Lu, J. H.; Yue, Z. Y.; Wang, J.; Zhou, P. *Arch. Biochem. Biophys.* **2012**, *523*, 144.

24. Sevigny, J.; Chiao, P.; Bussiere, T.; Weinreb, P.; Williams, L.; Maier, M.; Dunstan, R.; Salloway, S.; Chen, T.; Ling, Y.; O'Gorman, J.; Qian, F.; Arastu, M.; Li, M.; Chollate, S.; Brennan, M. S.; Quinyero-Monzon, O.; Scannevin, R. H.; Arnold, H. M.; Engber, T.; Rhodes, K.; Ferrero, J.; Hang, Y.; Mikulskis, A.; Grimm, J.; Hock, C.; Nitch, R. M.;

Sandrock, A. *Nature* **2016**, *537*, 50.

25. Ghosh, A.; Pradhan, N.; Bera, S.; Datta, A.; Krishnamoorthy, J.; Jana, N. R.; Bhunia, A. *ACS Chem. Neurosci.* **2017**, *8* (4), 718.

26. Kar, R. K.; Gazova, Z.; Bednarikova, Z.; Mroue, K. H.; Ghosh, A.; Zhang, R.; Ulicna, K.; Siebert, H. K.; Nifantiev, N. E.; Bhunia, A. *Biomacromolecules* **2016**, *17* (6), 1998.

27. Librizzi, F.; Carrotta, R.; Spigolon, D.; Bulone, D.; Biagio, P. L. S. *J. Phys. Chem. Lett*. **2014**, *5* (17), 3043.

28. Hopping, G.; Kellock, J.; Caughey, B.; Daggett, V. *ACS Med. Chem. Lett.* **2013**, *4*, 824.

29. Miura, Y.; You, C.; Ohnishi, R., Sci. Technol. *Adv. Mater.* **2008**, *9*, 024407.

30. Wada, M.; Miyazawa, Y.; Miura, Y. *Polym. Chem.* **2011**, *2*, 1822.

31. Cabaleiro-Lago, C.; Quinlan-Pluck, F.; Lynch, I.; Lindman, S.; Minogue, A. M.; Thulin, E.; Walsh, D. M.; Dawson, K. A.; Linse, S. *J. Am. Chem. Soc.* **2008**, *130*, 15437.

32. Xiao, L.; Zhao, D.; Chan, W. H.; Choi, M. M. F.; Li, H.-W. *Biomaterials* **2010**, *31*, 91.

33. Cabaleiro-Lago, C.; Quinlan-Pluck, F.; Lynch, I.; Dawson, K. A.; Linse, S. *ACS Chem. Neurosci.* **2010**, *1*, 279.

34. Skaat, H.; Shafir, G.; Margel, S. *J. Nanopart. Res.* **2011**, *13*, 3521.

35. Richman, M.; Wilk, S.; Skirtenko, N.; Perelman, A.; Rahimipour, S. *Chem. Eur. J.*

2011, *17*, 11171.

36. Yoo, S. I.; Yang, M.; Brender, J. R.; Subramanian, V.; Sun, K.; Joo, N. E.; Jeong, S. H.; Ramamoorthy, A.; Kotov, N. A. *Angew. Chem., Int. Ed.* **2011**, *50*, 5110.

37. Thakur, G.; Micic, M.; Yang, Y.; Li, W.; Movia, D.; Giordani, S.; Zhang, H.; Leblanc, R. M. *Int. J. Alzheimers DIs.* **2011**, *2011*, 502386.

38. Skaat, H.; Chen, R.; Grinberg, I.; Margel, S. *Biomacromolecules* **2012**, 13, 2662

39. MahmouDI, M.; Akhavan, O.; Ghavami, M.; Rezaee, F.; Ghiasi, S. M. A. *Nanoscale* **2012**, *4*, 7322.

40. Liao, Y. H.; Chang, Y. J.; Yoshiike, Y.; Chang, Y. C.; Chen, Y. R. *Small* **2012**, *8*, 3631.

41. Derakhshankhah, H.; Hajipour, M. J.; Barzegari, E.; LotfabaDI, A.; Ferdousi, M.; ASaboury, A. A.; Ng, F. P.; Raoufi, M.; Awala, H.; Mintova, S.; DInarvand, R.; MahmouDI, M. *ACS Appl. Mater. Interfaces* **2016**, *8* (45), 30768.

42. Anand, B.G.; Dubey, K.; Shekhawat, D. S.; Kar, K. *Biochemistry* **2016**, *55* (24), 3345.

43. Skaat, H.; Chen, R.; Grinberg, I.; Margel, S. *Biomacromolecules* **2012**, *13* (9), 2662

44. Palmal, S.; Jana, N. R.; Jana, N. R. *J. Phys. Chem. C* **2014**, *118* (37), 21630.

45. S. Li, L.; Wang, C.; Chusuei, C.; Suarez V. M.; Blackwelder, P. L.; Orbulescu, J.; Lebanc, R. M. *Chem. Mater.* **2015**, *27* (5), 1764.

46. Palmal, S.; Maity, A. R.; Singh, B. K.; Basu, S.; Jana, N. R.; Jana, N. R. *Chem. Eur. J.* **2014**, *20*, 6184.

47. Taebnia, N.; MorsheDI, D.; Yaghmaei, S.; Aliakbari, F.; Rahimi, F.; Aprpanaei, A. *Langmuir* **2016**, *32*, 13394.

48. Tiwari, S.K.; Agarwal, S.; Seth, B.; Yadav, A.; Nair, S.; Bhatnagar, P.; Karmakar, M. ; Kumari, M.; Chauhan, L. K.; Patel, D. K.; Srivastava, V.; Singh, D.; Gupta, S. K.; Tripathi, A.; ChaturveDI, R. K.; Gupta, K. C. *ACS Nano* **2014**, *8*, 76.

49. Siposova, K.; Pospiskova, K.; Bednarikova, Z.; Safarik, I.; Safarikova, M.; Kubovcikova, M.; Kopcansky, P.; Gazova, Z. *J. Magnetism and Magnetic Materials* **2017**, *427*, 48.

50. Chikae, M.; Fukuda, T.; Kerman, K.; Idegami, K.; Miura, Y.; Tamiya, E. *Bioelectroc hemistry* **2008**, *74*, 118.

51. Kouyoumdjian, H.; Huang, X. *Carbohydrate Nanotechnology* (Stine, K., Ed.) **2015**, *12*, 309.

52. Rocha, S.; Thuneman, A. F.; Pereira, M. D.; Coelho, M.; Mohwald, H.; Brezesinski, G. *Biophys. Chem.* **2008**, *137* (1), 35.

53. Saraiva, A. M.; Cardoso, I.; Pereira, M. C.; Coelho, M. A. N.; Saraiva, M. J.; Moehwald, H.; and Brezesinski, G. *ChemBioChem* **2010**, *11*, 1905.

54. Yousaf, M.; Huang, H.; Li, P.; Wang, C.; Yang, Y. *ACS Chem. Neurosci.* **2017**, *8* (6), 1368

55. Torok, M.; Abid, M.; Mhadgut, S. C.; Torok, B. *Biochemistry* **2006**, *45* (16), 5377.

56. Sood, A.; Abid, M.; Hailemichael, S.; Foster, M.; Török, B.; Török, M. *Bioorg. Med. Chem. Lett.* **2009**, *19*, 6931.

57. Müller, K.; Faeh, C.; DIederich, F. *Science* **2007**, *317*, 1881.

58. Buck, M. *Q Rev. Biophys.* **1998**, *31* (3), 297.

59. Yamaguchi, K.; Naiki, H.; Goto, Y. *J. Mol. Biol.* **2006**, *363* (1), 279.

60. Khan, M. V.; Rabbani, G.; Ahmad, E.; Khan R. H. *Int. J. Biol. Macromol.* **2014**, *70*, 606.

61. Rajan R; Balaram P. *Int. J. Pept. Protein Res.* **1996**, *48* (4), 328.

62. Peng Y.; Britt, D. W. **2011**, Utah State University, Logan.

63. Bolisetty, S.; Vallooran, J. J.; Adamcik, J.; Mezzenga, R. *ACS Nano* 2013, 7, 6146

64. Adamcik, J.; Mezzenga, R. *Macromolecules* **2012**, *45* (3) 1137.

65. Adamcik, J.; Jung J. M.; Flakowski J.; Rios P. L.; DIetler G.; Mezzenga R., *Nature nanotechnology* **2010**, *5* (6), 423.

66. Adamcik, J.; Mezzenga, R. *Macromolecules* **2012**, *45* (3), 1137.

67. Adamcik, J.; Mezzenga, R. *Soft Matter* **2011**, *7* (11), 5437.

68. Adamcik, J.; Mezzenga, R. *Current opinion in colloid & interface science* **2012**, *17* (6), 369.

69. Jones, O. G.; Handschin, S.; Adamcik, J.; Harnau, L.; Bolisetty, S.; Mezzenga, R. *Biomacromolecules* **2011**, *12* (8), 3056.

70. Gilbert, J.; Campanella, O.; Jones, O. G. *Biomacromolecules* **2014**, *15* (8), 3119.

71. Jones, O.G.; Adamcik, J.; Handschin, S.; Bolisetty, S.; Mezzenga, R. *Langmuir* **2010**, *26* (22), 17449.

72. Guzzi, R.; Rizzuti, B.; Labate, C.; Zappone, B.; De Santo, M. P. *Biomacromolecules* **2015**, *16* (6), 1794.

73. Jordens, S.; Riley, E. E.; Usov, I.; Isa, L.; Olmsted, P. D.; Mezzenga, R. *ACS Nano* **2014**, *8*, 11071.

74. Dave, A. C.; Loveday, S. M.; Anema, S. G.; Jameson, G. B.; Singh, H. *Biomacromolecules* **2014**, *15* (1), 95.

75. Hettiarachchi, C. A.; Melton, L. D.; Gerrard, J. A.; Loveday, S. M. *Biomacromolecules* **2012**, *13* (9), 2868.

76. Zappone, B.; De Santo, M. P.; Labate, C.; Rizzuti, B.; Guzzi, R. *Soft matter* **2013**, *9*, 2412.

77. Lee, G.; Lee, W.; Lee, H.; Lee, C. Y.; Eom, K.; Kwon, T. *Scientific Reports* **2015**, *5*, 16220.

78. Peng, Y.; Turner N. W.; Britt, D. W. *Colloids Surface B* **2014**, *119*, 6.

79. Bolisetty, S.; Adamcik, J.; Mezzenga, R. *Soft Matter* 2011, *7* (2), 493.

80. Sudhakar, S.; Kalipillai, P.; Santhosh, P. B.; Mani, E. *J. Phys. Chem. C* **2017**, *121* (11), 6339.

81. Ban, S. K.; Paul, S. *ACS Appl. Mater. Interfaces* **2016**, *8* (46), 31587.

82. Tu, Y.; Ma S.; Liu, F.; Sun, Y.; Dong, X. *J. Phys. Chem. B* **2016**, *120* (44), 11360.

83. D'Amico, M.; Carlo, M. G.; Groenning, M.; Militello, M.; Vetri, V.; Leone, M.; *J. Phys. Chem. Lett.* **2012**, *3* (12), 1596.

84. Cabaleiro-Lago, C.; Quinlan-Pluck, F.; Lynch, I.; Dawson, K. A.; Linse, S. *ACS Chem. Neurosci.* **2010**, *1*, 279.

85. Cabaleiro-Lago, C.; Quinlan-Pluck, F.; Lynch, I.; Lindman, S.; Minogue, A. M.; Thulin, E.; Walsh, D. M.; Dawson, K. A.; Linse, S. *J. Am. Chem. Soc.* **2008**, *130*, 15437.

86. Anand, B.G.; Dubey, K.; Shekhawat, D.S.; Kar, K. *Biochemistry* **2016**, *55* (24), 3345.

87. Cabaleiro-Lago, C.; Szczepankiewicz, O.; Linse, S. *Langmuir* **2012**, *28* (3), 1852.

88. Cedervall, T.; Lynch, I.; Lindman, S.; Berggard, T.; Thulin, E.; Nilsson, H.; Dawson, K. A.; Linse, S. *Proc. Natl. Acad. Sci. U.S.A.* **2007**, *104*, 8691.

89. Kroes-Nijboer, A.; Lubbersen, Y.S.; Venema, P.; van der Linden, E. *J. Struct. Biol.* **2009**, *165* (3) 140.

90. Loveday, S. M.; Wang, X. L.; Rao, M. A.; Anema, S. G.; Creamer, L. K.; Singh, H. *International Dairy Journal* 2010, *20*, 571.

91. D'Amico, M.; Schiro, G.; Cupane, A.; D'Alfonso, L.; Leone, M.; Militello, V.; Vetri, V. *Langmuir* **2013**, *29* (32), 10238.

92. Yang, H. Y.; Yang, S. N.; Kong, J. L.; Dong, A. C.; Yu, S. N. *Nature Protocols* **2015**, *10*, 382.

93. Pal S.; Maity, S.; Sardar P.; Chakraborty J.; Halder U. C. *Int. J. Biol. Macromol.*

2016, *84*, 121.

94. Andreas, B. *Prog. Biophys. Mol. Biol.* **2000**, *74*, 141.

95. Pereira, R. N.; Souza, B. W. S.; Cerqueira, M. A.; Teixeira, J. A.; Vicente, A. A. *Biomacromolecules* **2010**, *11* (11), 2912.

96. Papiz, M. Z.; Sawyer, L.; Eliopoulos, E. E.; North, A. C. T.; Findlay, J. B. C.; Sivaprasadarao, R.; Jones, T. A.; Newcomer, M. E.; Kraulis, P. J. *Nature* **1986**, *324*, 383.

97. Monaco, H. L.; Zanotti, G.; Spadon, P.; Bolognesi, M.; Sawyer, L.; Eliopoulos, E.E. *J. Mol. Biol.* **1987**, *197*, 695.

98. Ragona, L.; Pusterla, F.; Zetta, L.; Monaco, H. L.; Molinari, H. *FolDIng Des.* **1997**, *2*, 281.

99. Sawyer, L.; Brownlow, S.; Polikarpov, I.; Wu, S. Y. *Int. Dairy J.* **1998**, *8*, 65.

100. Wu, S. Y.; Pérez, M. D.; Puyol, P.; Sawyer, L. *J. Biol. Chem.* **1999**, *274*, 170.

CHAPTER 4

AQUEOUS SYNTHESIS OF SUPERHYDROPHOBIC NANOPARTICLES AND

THEIR AMYLOID INHIBITION ABILITY

4.1 Abstract

Superhydrophobic silica nanoparticles (SHSN) were synthesized from fluorinated (3F) and methylated (nPM) trimethoxy-silane precursors. This synthesis from hydrophobic precursor silanes occurs through an acid hydrolysis followed by base-initiated condensation, without the need for organic solvents. SEM and AFM analysis reported that fluorinated SHSN were relatively monodisperse and smaller (250 ± 30 nm), compared with the methylated SHSN (500 ± 200 nm). Water contact angles on both fluorinated and methylated SHSN coated surfaces were > 150°. Amyloid inhibition behavior of these SHSN against BLG showed that fluorinated SHSN could inhibit amyloid fibrillation, whereas under the same conditions the methylated SHSN did not inhibit BLG fibrillation.

4.2 Introduction

A surface is considered superhydrophobic when it exhibits a water contact angle larger than 150° and detachment or sliding angle lower than a 5° tilt of the surface. Superhydrophobic surfaces have gained wide interest due to their low fouling, self-cleaning, and low friction properties. (1) Superhydrophobic surfaces have various potential applications due to their anticorrosive, self-cleaning, antifogging, anti-icing, drag reducing, oil-water separating, and water harvesting properties. (2-11) Nanoparticles (NPs) with superhydrophobic properties can also be used as drug delivery vehicles and therapeutic agents against the protein misfolding-based diseases. (12-14) Engineered biocompatible NPs have shown great promise as therapeutic agents for amyloid-related diseases, as they are capable of crossing the blood-brain-barrier (BBB). (15, 16) NPs can both promote and inhibit protein aggregation by binding with proteins and trapping the early intermediates. (17) N-isopropylacrylamide / N-tert-butylacrylamide, titanium oxide, and quantum dots based NPs can promote the protein assembly into amyloid fibrils in vitro, by assisting the nucleation process. (18-20) In contrast, other studies have demonstrated that hydrophobic NPs, or NPs functionalized with hydrophobic molecules, can inhibit the fibrillation process. (21-22) Cabaleiro-Lago et al. reported that copolymer NPs of variable hydrophobicity inhibited the fibrillation of αβ (1-40). (17) Fluorinated NPs are also potential inhibitors against the αβ fibrillation. (23) To investigate

superhydrophobic NPs against amyloid formation, we have synthesized fluorinated and

methylated SHSN from alkyl- and fluoro-silane precursors.

Conventional synthesis of SHSN follows the Stöber method, where hydrophilic silica

nanoparticles (HSN) are first synthesized, isolated, purified, and then functionalized

using the hydrophobic silanes. (8, 9) This multi-step method for synthesizing SHSN is

carried out using alcohol as the solvent, and it requires addition of a strong base. Here,

we present an aqueous method to synthesize SHSN from a single precursor, where

precursors are initially hydrolyzed in a mild acidic condition before a catalyst (NH_4OH)

is added to initiate condensation. This method requires only a single isolation and

washing step, providing a more sustainable and environmentally friendly approach to

produce SHSN. Our synthesized SHSN were tested against the fibrillation of BLG. The

size and shapes of the SHSN were assessed using DLS and AFM, and

superhydrophobicity was confirmed by static water contact angle.

4.3 Experimental procedure

Materials

3,3,3-trifluoropropyl trimethoxy silane (3F, > 95 % purity, MW = 218.3, d =

g/ml), and n-propyltrimethoxy silane (nPM, > 95 % purity, MW = 164.3, d = 0.94 g/ml)

were purchased from Gelest, Inc. (Morrisville, PA). 50 % (w/w) NH_4OH was purchased

from Fisher Scientific. Muscovite mica was purchased from SPI supplies for the AFM study (PA, USA); AFM tips were obtained from TED Pella Inc., CA (TAP300AL-G-50).

Synthesis of fluorinated and methylated SHSN

0.4 M nPM and 3F were hydrolyzed at pH 3.0 in glass vials at room temperature. Once nPM and 3F were hydrolyzed, 0.05 M NH_4OH was added to generate NPs with different sizes. Reactions were continued until stable white NPs were visible. Once the NPs were formed, both nPM and 3F solutions with newly formed NPs were centrifuged; and then the NPs were separated from the supernatant and washed with DI water, and freeze-dried overnight.

Characterization of fluorinated and methylated SHSN

SEM images were taken using a FEI Quanta FEG 650 equipped with an Oxford X-Max Energy Dispersive X-ray spectroscope (EDS) housed in the Microscopy Core Facility at Utah State University. Samples were imaged with 20 kV accelerating potential without conductive coatings. AFM images were taken using a Nanoscope III Bioscope (Digital Instrument, Inc.) in tapping mode. 100 µl samples were dropped on freshly cleaved mica surfaces, then gently washed with DI water, and air-dried before taking AFM images.

The hydrophobicity of the NPs was determined using water contact angle. The contact angle was measured with a VCA Optima digital contact angle instrument (AST

products, Billerica, MA). 10 µl DI water was dropped on NP thin films prepared on double-stick tape over glass slides, and then the contact angle was measured.

The NP FTIR spectra were collected using a Varian 660-IR with a horizontal single reflection Pike Technologies MIRacle attenuated total reflectance (ATR) unit, fitted with a ZnSe crystal. 100 µl samples were drop cast on the ZnSe crystal of the ATR platform, and air-dried before taking the reading. Readings were taken after averaging 20 scans over the range of 600 to 1800 cm^{-1} with a resolution of 1 cm^{-1}. Prior to each reading, a background scan was acquired. The spectra provide signatures of the pure NPs for future works involving mixed alkyl-fluoro-NPs and NP-protein interactions.

Interaction of fluorinated and methylated SHSN with BLG

Fluorinated and methylated SHSNs were reacted against BLG at pH 2.0 and room temperature for 10 min, and then the fibrillation process was tested at 85°C for 5 h. Next, samples were cooled down to room temperature again, using ice bath, and resulting protein fibrils were investigated using AFM, operating in tapping mode in air.

4.4 Results and Discussion

SEM images of fluorinated and methylated SHSN are shown in Figure 4-1 (a) and (b), respectively. Average size of the fluorinated and methylated SHSN were 250±30 nm and 500±200 nm, respectively.
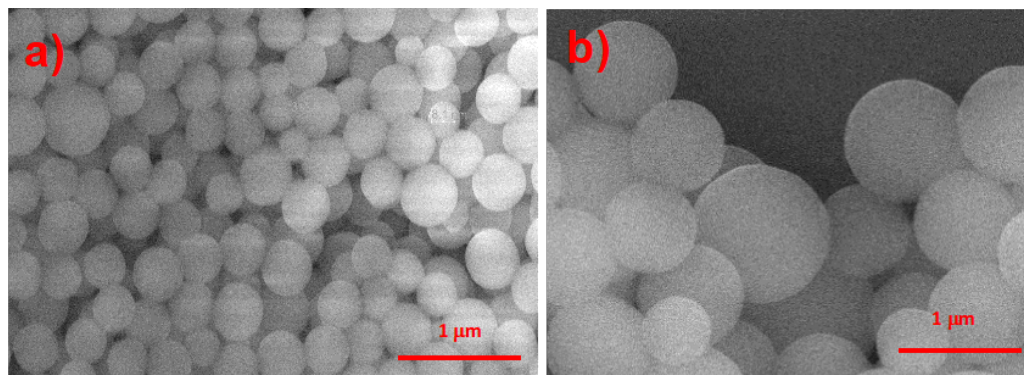
Figure 4-1. SEM images of (a) fluorinated SHSN and (b) methylated SHSN

These size DIstributions were further confirmed using AFM image analysis shown as 3D structures in Figure 4-2. Both SEM and AFM showed that the methylated NPs were larger in size, compared to the fluorinated NPs, and the fluorinated NPs were highly monodispersed, as compared to the methylated NPs.
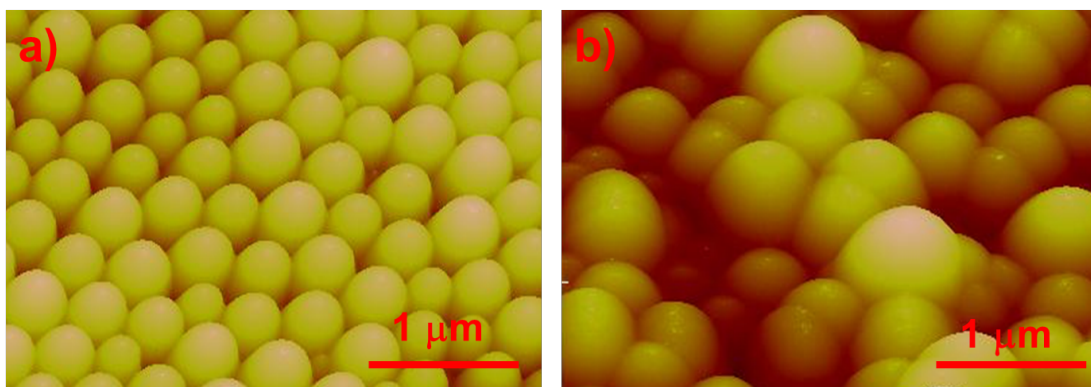
Figure 4-2. AFM images of (a) fluorinated SHSN, and (b) methylated SHSN.

The presence of the fluorine functionality in the fluorinated NPs was confirmed, as ATR-FTIR-spectra shows the –CF stretching at 1250 cm^{-1}, 840 cm^{-1}, and 990 cm^{-1} (Figure 4-3). Presence of CH$_3$, and CH$_2$ bending along with the Si-O-Si, and Si-CH$_2$-R stretching peaks confirmed the hydrophobic functionality on both the SHSN surfaces.
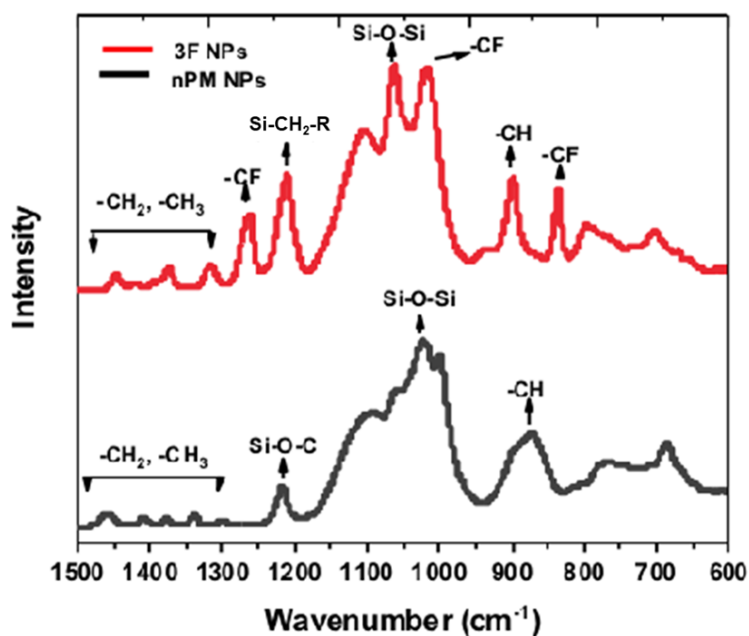
Figure 4-3. ATR-FTIR spectra of (a) fluorinated SHSN (red, top), and (b) methylated SHSN (black, bottom).

Superhydrophobicity was confirmed by water contact angles on the fluorinated and methylated SHSN-coated surfaces. Figure 4-4 (a) and (b) show that the water contact

angles are >150° on both the fluorinated and methylated SHSN-coated surfaces, and

confirm the superhydrophobic behavior of both SHSNs.
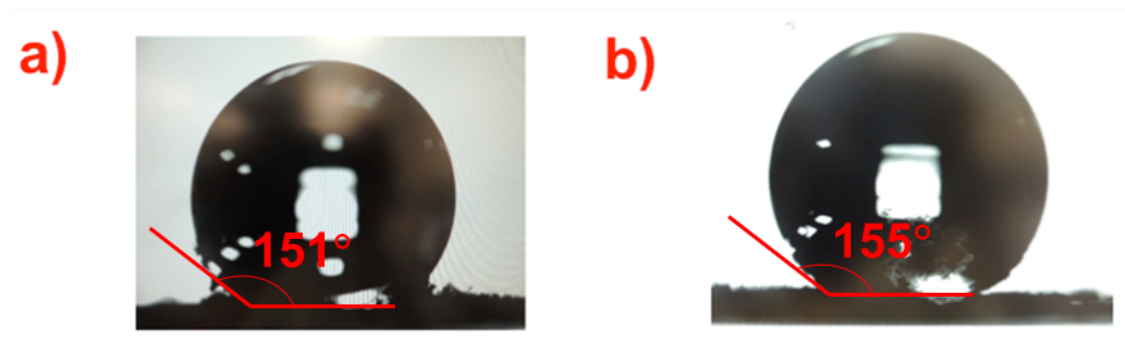
Figure 4-4. Static water contact angle (a) fluorinated SHSN, and (b) methylated SHSN prepared as thin films on double-stick tape.

When these SHSN were used against the fibrillation of BLG, the fluorinated

SHSN were capable of inhibiting the amyloid formation, with only a few fibrils being

observed in the AFM image representing the fluorinated SHSN-treated BLG (Figure 4-5

(a)). In the same AFM image, significant aggregated features are observed, which may be

the unreacted NPs or NP-BLG composites formed after the NPs and BLG interaction.

However, methylated SHSN did not inhibit the fibrillation of BLG, as Figure 4-5 (b)

shows numerous fibrils formed during the inhibition process. This distinct inhibition

behavior of fluorinated and methylated SHSN proves that the amyloid inhibition is

discretely affected, due to the presence of the fluorine functionality.
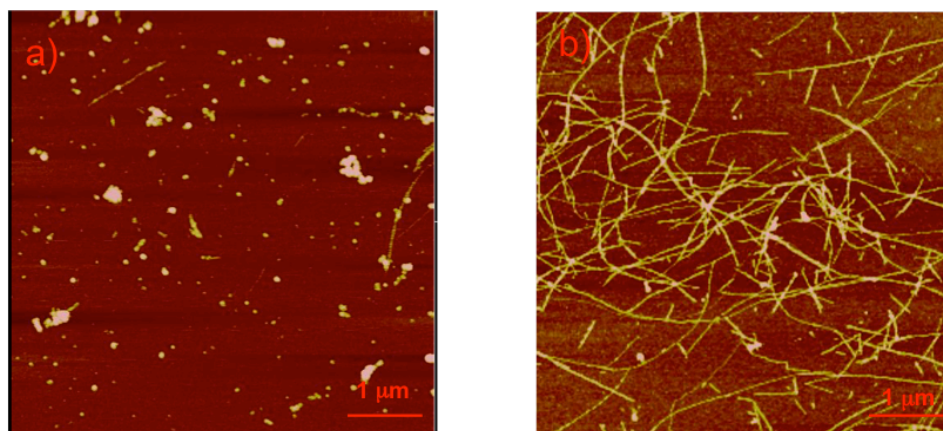
Figure 4-5. AFM images of amyloid inhibition of BLG by (a) fluorinated SHSN, and (b) methylated SHSN.

4.5 Conclusion

The successful aqueous synthesis of the superhydrophobic NPs from both fluorinated and methylated silane precursors showed a new, environmentally friendly and simple approach to synthesize the SHSN, without using a orthosilicate precursor, followed by surface modification with the hydrophobic silane as a capping layer. These SHSN have applications as discrete particles for tuning protein secondary structure, as well as composite properties when assembled as thin films, rendering the surface superhydrophobic. The facile synthesis of the NPs in aqueous solvents offers this approach suitable for biological interactions. The unique amyloid inhibition ability of the fluorinated SHSN, contrasted with the methylated SHSN, underscores the role of the fluoro-groups in this activity. Both NPs exhibited a similar surface energy, based on

sessile water droplet contact angles, thus the protein structure-tuning behavior is not merely a function of surface energy. These results suggest the potential of fluorinated SHSN to be used in the treatment of protein misfolding-based diseases as well as in biotechnology applications where protein aggregation and assembly must be controlled. The aqueous synthesis process from a single precursor is an economically and environmentally viable approach to scaling this technology for superhydrophobic nanoparticle production.

4.6 References

1. Li, X. M.; Reinhoudt, D.; Crego-Calama, M. *Chem. Soc. Rev*. **2007**, *36*, 1350.

2. Wang, S.; Liu, K.; Yao, X.; Jiang, L. *Chem. Rev.* **2015**, *115* (16), 8230.

3. Wen, L.; Tian, Y.; Jiang, L. *Angew. Chem., Int. Ed.* **2015**, *54* (11), 3387.

4. Simpson, J. T.; Hunter, S. R.; Aytug, T. *Rep. Prog. Phys.* **2015**, *78* (8), 086501.

5. Lai, Y.; Tang, Y.; Gong, J.; Gong, D.; Chi, L.; Lin, C.; Chen, Z. *J. Mater. Chem.* **2012**, *22* (15), 7420.

6. Sun, Z.; Liao, T.; Liu, K.; Jiang, L.; Kim, J. H.; Dou, S. X. *Small* **2014**, *10* (15), 3001.

7. Zhang, Y. L.; Xia, H.; Kim, E.; Sun, H.-B. *Soft Matter* **2012**, *8* (44), 11217.

8. Chu, Z.; Feng, Y.; Seeger, S. *Angew. Chem., Int. Ed.* **2015**, *54* (8), 2328.

9. Wang, B.; Liang, W.; Guo, Z.; Liu, W. *Chem. Soc. Rev.* **2015**, *44* (1), 336.

10. Li, J.; Shi, L.; Chen, Y.; Zhang, Y.; Guo, Z.; Su, B. I.; Liu, W. *J. Mater. Chem.* **2012**, *22* (19), 9774.

11. Li, A.; Sun, H. X.; Tan, D. Z.; Fan, W. J.; Wen, S. H.; Qing, X. J.; Li, G. X.; Li, S. Y.; Deng, W. Q. *Energy Environ. Sci.* **2011**, *4* (6), 2062.

12. Spuch, C.; Saida, O.; Navarro, C. *Recent Pat. Drug Delivery Formulation* **2012**, *6*, 2.

13. Sahni, J. K.; Doggui, S.; Ali, J.; Baboota, S.; Dao, L; Ramassamy, C. *J. Controlled Release* **2011**, *152*, 208.

14. Brambilla, D.; Le Droumaguet, B.; Nicolas, J.; Hashemi, S. H.; Wu, L. P.; Moghimi, S. M.; Couvreur, P.; Andrieux, K. *NanomeDIcine* **2011**, *7*, 521.

15. Silva, G. A. *Nat. Rev. Neurosci.* **2006**, *7*, 65.

16. Kabanov, A. V.; Gendelman, H. E. *Prog. Polym. Sci.* **2007**, *32*, 1054.

17. Cabaleiro-Lago, C.; Quinlan-Pluck, F.; Lynch, I.; Dawson, K. A.; Linse, S. *ACS Chem. Neurosci.* **2010**, 1,279.

18. Linse, S.; Cabaleiro-Lago, C.; Xue, W. F.; Lynch, I.; Lindman, S.; Thulin, E.; Radford, S. E.; Dawson, K. A. *Proc. Natl. Acad. Sci. U. S. A.* **2007**, *104*, 8691.

19. Wu, W. H.; Sun, X.; Yu, Y. P.; Hu, J.; Zhao, L.; Liu, Q.; Zhao, Y. F.; Li, Y. M. *Biochem. Biophys. Res. Commun.* **2008**, *373*, 315.

20. Thakur, G.; Micic, M.; Yang, Y.; Li, W.; Movia, D.; Giordani, S.; Zhang, H.; Leblanc, R. M. *Int. J. Alzheimers DIs*. **2011**, *2011*, 502386

21. Richman, M.; Wilk, S.; Skirtenko, N.; Perelman, A.; Rahimipour, S. *Chem.Eur. J.* **2011**, *17*, 11171.

22. Skaat, H.; Chen, R.; Grinberg, I.; Margel, S. *Biomacromolecules* **2012**, *13*, 2662.

23. Rocha, S.; Thunemann, A. F.; Pereira, M. C.; Coelho, M.; Mohwald, H.; Brezesinski, G. *Biophys. Chem.* **2008**, *137*, 35,

CHAPTER 5

SUPERHYDROPHOBIC SILICA NANOPARTICLES AS CARRIERS FOR

HYDROPHOBIC SMALL DRUG MOLECULES

5.1 Abstract

Two hydrophobic therapeutic biomolecules, curcumin and quercetin were

successfully loaded on fluorinated and methylated superhydrophobic silica nanoparticles

(SHSN). DLS and SEM were used to measure the sizes of the curcumin and quercetin-

loaded nanoparticles (NPs). Hydrodynamic radius (R_h) measured by DLS showed that

after loading curcumin, the R_h of the fluorinated SHSN increased from 135 nm to 165

nm, and the R_h of the methylated SHSN increased from 250 nm to 308 nm. Similarly,

after loading quercetin, R_h of the SHSN increased from 135 nm to 175 nm, but the R_h of

the methylated SHSN increased from 250 nm to bimodal sizes of NPs, such as 134 nm

and 380 nm. This bimodal distribution of quercetin-loaded methylated SHSN was later

confirmed by DLS study. Curcumin loading in both fluorinated and methylated NPs and

quercetin loading in methylated NPs did not change the spherical shape of the

corresponding NPs, but quercetin loading in fluorinated NPs deformed the shape of the

NPs. Hydrophobicity of the fluorinated SHSN decreased after loading curcumin and

quercetin, as water contact angle decreased from 151° to 136° and 142°, respectively.

Similarly, hydrophobicity of the methylated SHSN also decreased after loading of

curcumin and quercetin, as water contact angle decreased from 155° to 142° and 145°, respectively. ATR-FTIR spectra confirmed the conjugation of the curcumin and quercetin in the NPs. Release kinetic study showed a quick initial burst of curcumin and quercetin release within 1 to 1.5 h; while cumulative releases reached their plateau after 5 h for curcumin and 7 to 10 h for quercetin, from both fluorinated and methylated NPs.

5.2 Introduction

Biomolecules such as curcumin and quercetin recently have attracted the attention of the scientific community, due to their astonishing antioxidant, anti-inflammatory, anticarcinogenic, chemopreventive, antiangiogenic, anti-diabetic, antiviral, and antibacterial properties. (1-10) Extensive research has been carried out on both quercetin and curcumin around the globe, to demonstrate their great potential as therapeutic agents, and both have shown the way toward clinical trials for a variety of diseases. (11-14) Despite the wide spectrum of beneficial properties, the use of both of these biomolecules in the commercial field is limited, because of their hydrophobic nature. (15-18) Hydrophobicity has been the major obstacle in their progress from being used as a drug in the lab to clinical studies. In recent years, researchers have focused on exploring the potential applications of these hydrophobic small molecules as drugs, with the aid of modern nanotechnologies. (19-21) Loading or conjugating these molecules in NPs, liposomes, micelles, soy protein isolate, oil body encapsulation, cyclodextrin, chitosan,

and phospholipid complex has proven to enhance the dispersibility and bioactivity of these molecules for clinical trials. (22-30) Conjugating or loading the drug molecules in NPs has become increasingly remarkable, because it offers numerous benefits, including ease of handling, enhanced stability, controlled release, and enhanced bioavailability and efficacy. Inorganic silica, alumina, and titanium-based NPs are widely used as drug carriers for their compatibility in biological systems. (31-36). Superhydrophobic silica nanoparticles (SHSN) have the potential to be used as drug delivery vehicles for the active drug molecules. Conventional synthesis of drug-loaded SHSN includes the initial synthesis of hydrophilic silica NPs, following the Stöber method, followed by isolation, purification of the NPs, and then functionalizing them, using a hydrophobic silane; followed by further isolation, purification, and drug loading steps. (37, 38) This multistep method is carried out using alcohol as a solvent, and it requires the addition of a strong base. In previous chapters, we have described a new one-step aqueous synthesis of SHSN, which opens the door to loading or conjugating small hydrophobic drug molecules in SHSN, in an environmentally friendly and biocompatible system.

This study aimed to synthesize quercetin and curcumin-loaded / conjugated superhydrophobic silica NPs in an environmentally friendly aqueous system, with only a single isolation and washing step. This effective and stable incorporation of drug molecules in the SHSN can lead to other hydrophobic drug molecules being integrated in the NP-based drug delivery vehicles.

5.3 Experimental procedure

Materials

3,3,3-trifluoropropyl trimethoxy silane (3F, > 95 % purity, MW = 218.3, d = 1.14 g/ml), and n-propyltrimethoxy silane (nPM, > 95 % purity, MW = 164.3, d = 0.94 g/ml) were purchased from Gelest, Inc. (Morrisville, PA). 50 % (w/w) NH_4OH was purchased from Fisher Scientific. Muscovite mica was purchased from SPI supplies for the AFM study (PA, USA); AFM tips were obtained from TED Pella Inc., CA (TAP300AL-G-50). Ethanol was obtained from Pharmco-AAPER (Brookfield), and dimethyl sulfoxide (DMSO) (99.5 %) was obtained from Sigma-Aldrich (MO, U.S.A). Quercetin hydrate was purchased from Acros Organics (Morris Plains, NJ, USA), and curcumin was purchased from Sigma-Aldrich (MO, U.S.A).

Synthesizing silica-drug molecule composite

Hydrolysis of 3F (0.4 M) and nPM (0.4 M) were performed at pH 3.0 separately, in glass vials in DI water. 4 mg of quercetin and curcumin were separately dissolved in 2 ml ethanol to have 2 mg/ml solution, and then added to the hydrolyzed silanes. Next, quercetin and curcumin-loaded silica NPs were synthesized, following the Stöber method. (39) The overall experimental process is shown in Figure 5-1. Once the synthesis was completed, as white colloidal particles appeared, NPs were centrifuged, washed, and lyophilized for further characterization and drug release study. Note: samples were taken before lyophilization, to perform DLS study.
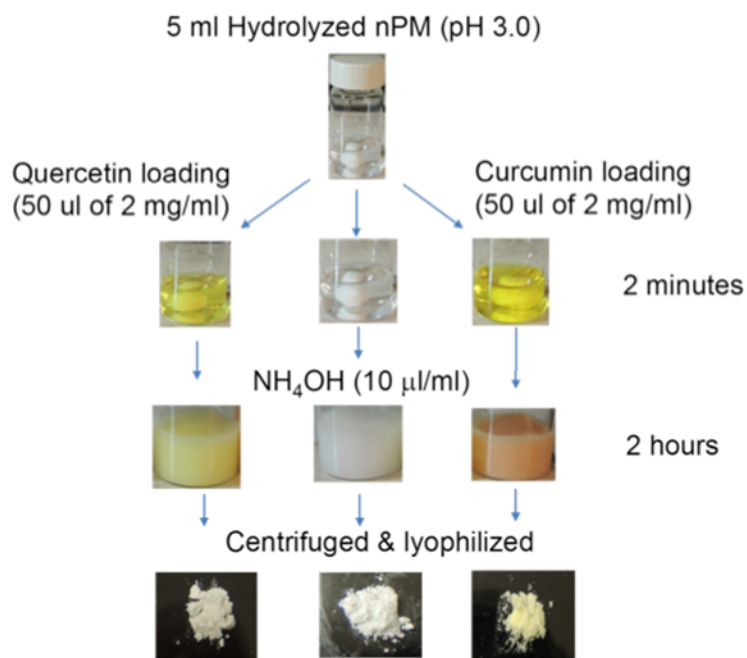
Figure 5-1. Flow chart and corresponding images of loading small drug molecules in HSNs.

Characterization of drug-loaded silica nanocomposite particles

The hydrodynamic radii (R_h) of the curcumin and quercetin-loaded or unloaded, fluorinated and methylated NPs were analyzed using DLS (DynaPro NanoStar, Wyatt Technology Corporation, Santa Barbara, CA), with a 658 nm laser. DLS measurements were taken using a quartz cuvette (JC-426, 1 μl) filled with 1 ml aqueous solution containing drug-loaded and unloaded NPs. Prior to the R_h measurement, NPs in the aqueous solutions were diluted 100 times.

SEM was performed with a FEI Quanta FEG 650 equipped with an Oxford X-Max Energy Dispersive X-ray Spectroscope (EDS) housed in the Microscopy Core

Facility at Utah State University. Samples were imaged with 20 kV accelerating

potential, without conductive coatings. AFM images were taken using a Nanoscope III

Bioscope (Digital Instrument, Inc.) in tapping mode. 100 µl samples were dropped onto

freshly cleaved mica surfaces, and then gently washed with DI water and air-dried before

taking AFM images. The water contact angle was measured with a VCA Optima digital

contact angle instrument (AST products, Billerica, MA) on the quercetin and curcumin-

loaded and non-loaded HSN kept on a double-stick tape surface over glass slides, using

10 µl sessile drops of DI water. The chemical bonding between silica and drug molecules

were analyzed by FTIR, using a Varian 660-IR with a horizontal single reflection Pike

Technologies MIRacle attenuated total reflectance (ATR) unit, fitted with a ZnSe crystal.

100µl samples were drop casted on the ZnSe crystal of the ATR platform, and air-dried

before taking the reading. Readings were taken after averaging 20 scans over the range of

600 cm^{-1} to 1800 cm^{-1}, with a resolution of 1 cm^{-1}. Prior to each reading, a background

scan was acquired.

Drug release kinetics study

Drug release kinetic study was performed in a PBS buffer solution (pH 7.0) for 4

days. 0.5 mg/ml curcumin and quercetin-loaded, fluorinated and methylated SHSN were

added in 1 ml PBS solution and shaken (200 rpm) at 37°C, kept in an incubator. All

samples were covered with aluminum foil during the incubation period.
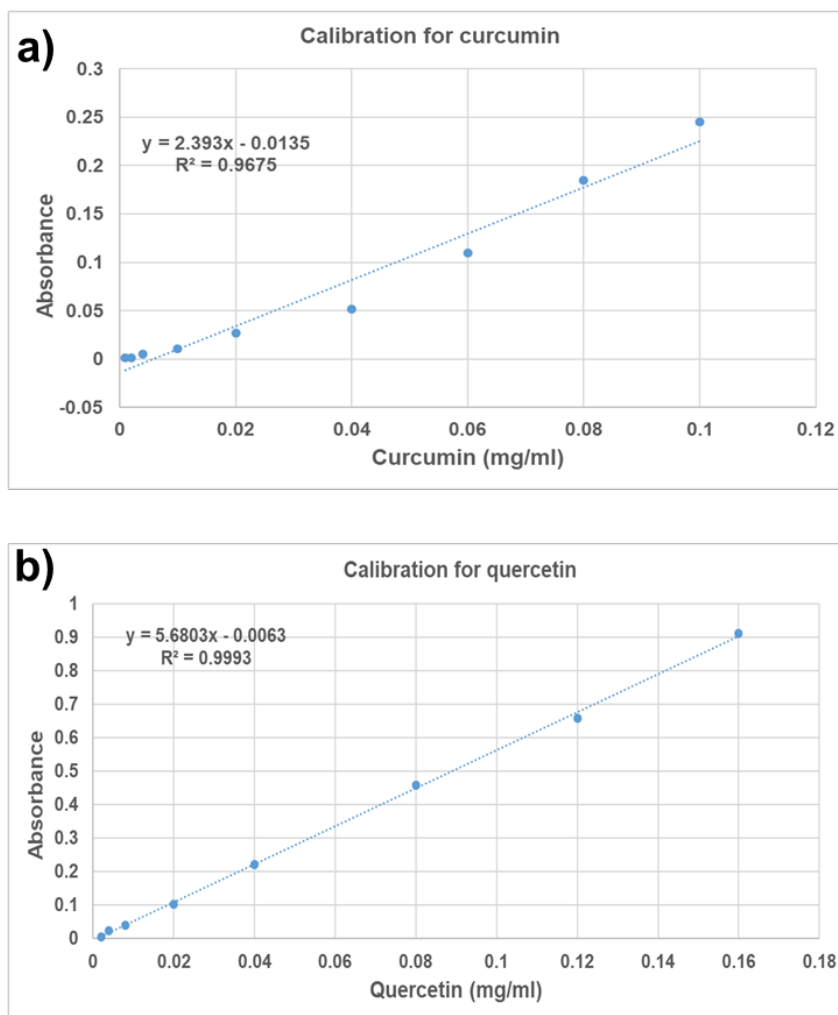
Figure 5-2. Calibration curve for (a) curcumin, and (b) quercetin measured in 50 % ETOH and 50 % DMSO, respectively.

After being centrifuged at 14 k for 10 min, 100 μl samples were collected from the supernatant of each vial at the desired time, and added in 100 μl DMSO and ETOH in a 96-well plate to measure quercetin and curcumin absorbance, respectively. Absorbance data were taken at 370 nm and 420 nm wavelengths for quercetin and curcumin,

respectively. Prior to the analysis of release kinetics of both curcumin and quercetin, calibration curves were obtained, as shown in Figure 5-2 (a) and (b) for curcumin and quercetin, respectively. For the absorbance reading of curcumin samples 50 % ETOH, and for quercetin samples 50 % DMSO solutions were used.

5.4 Results and Discussion

Hydrodynamic radius (R_h) of curcumin and quercetin loaded on both fluorinated and methylated NPs are shown in Figures 5-3 and 5-4, respectively. R_h size of the curcumin loaded fluorinated NPs were larger (165±18 nm), compared to the unloaded fluorinated NPs (135±10 nm) shown in Figure 5-3 (a). Similarly, the R_h of the curcumin-loaded methylated NPs were larger (308±35 nm), compared to the unloaded NPs (250±22 nm) shown in Figure 5-3 (b).
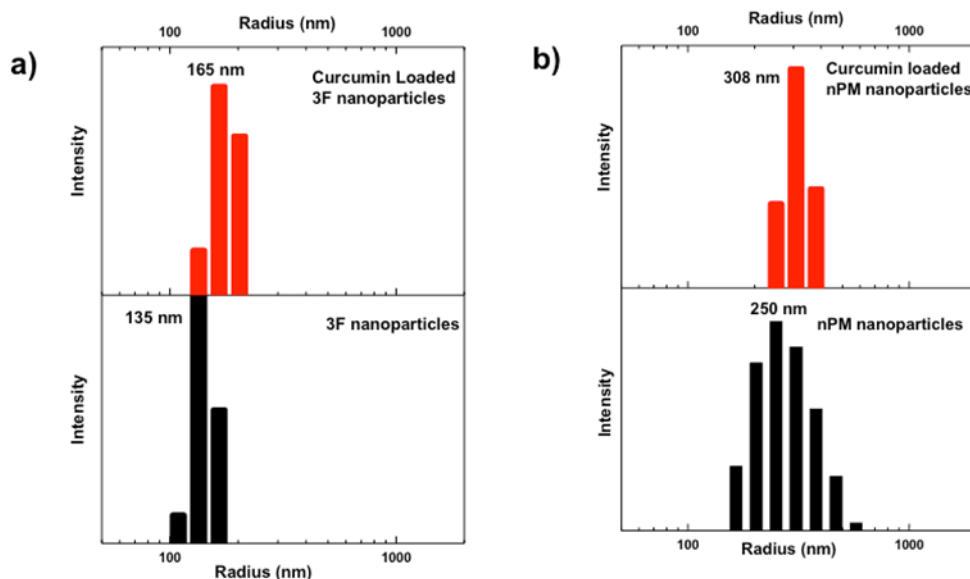
Figure 5-3. Hydrodynamic radius (R_h) of curcumin loaded (a) fluorinated NPs, and (b) methylated NPs.

Quercetin-loaded fluorinated and methylated NPs followed a similar trend as curcumin-loaded NPs. Figure 5-4 (a) shows that quercetin-loaded fluorinated NPs were larger (175±8 nm), compared to the unloaded NPs (135±10 nm). But interestingly, a bimodal distribution of NPs was observed in the case of quercetin-loaded methylated NPs, as two sizes of 134±5 nm and 380±20 nm can be observed in Figure 5-4 (b). Increase in the sizes of the drug-loaded fluorinated and methylated NPs indicates the successful loading or conjugation of the drug molecules.
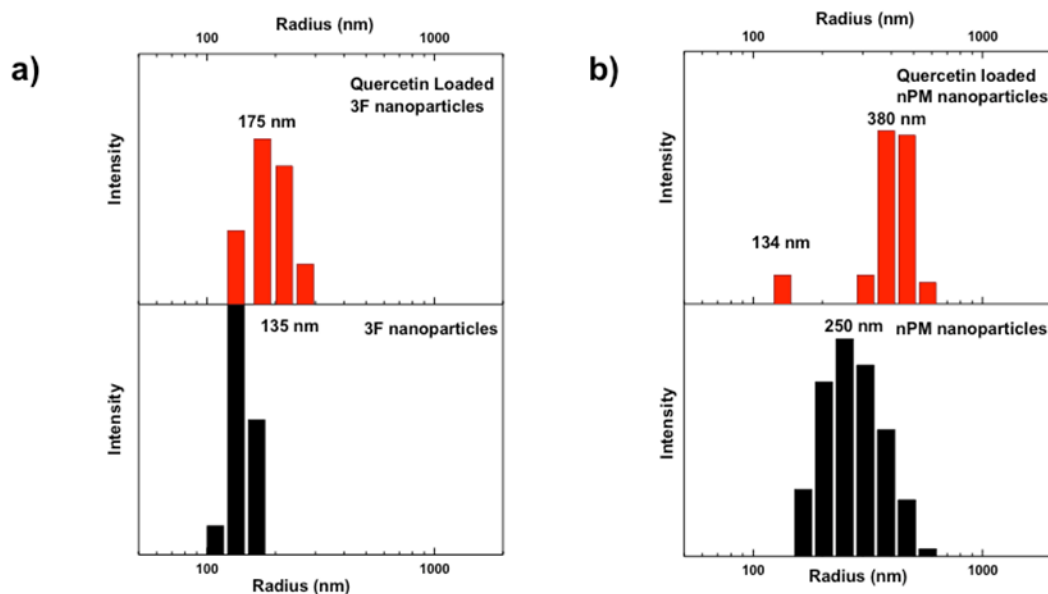
Figure 5-4. Hydrodynamic radius (R_h) of quercetin-loaded (a) fluorinated NPs, and (b) methylated NPs.

For further confirmation, SEM images were obtained, as shown in Figures 5-5 and 5-6. SEM images confirmed the increase of NP sizes after loading the drug molecules. Figure 5-5 (a) and (b) show the curcumin-loaded and unloaded fluorinated NPs. Curcumin-loaded fluorinated NPs (Figure 5-5 (a)) showed increase in size, compared to the unloaded NPs (Figure 5-5 (b)), as their diameter increased from 250±20 nm to 290±5 nm, which is consistent with the DLS-obtained sizes.

An opposite trend can be observed in the curcumin-loaded methylated NPs' sizes, as curcumin-loaded NPs decreased to 450±50 nm (Figure 5-5 (d)) from unloaded NPs of 540±50 nm (Figure 5-5 (c)). The shapes of the NPs didn't change after curcumin was

loaded in the fluorinated NPs, rather it remained smooth and spherical as it was in the

unloaded NPs. However, after curcumin was loaded in the methylated NPs, the shape of

the NPs no longer remained spherical, rather it turned into egg-shaped structures.
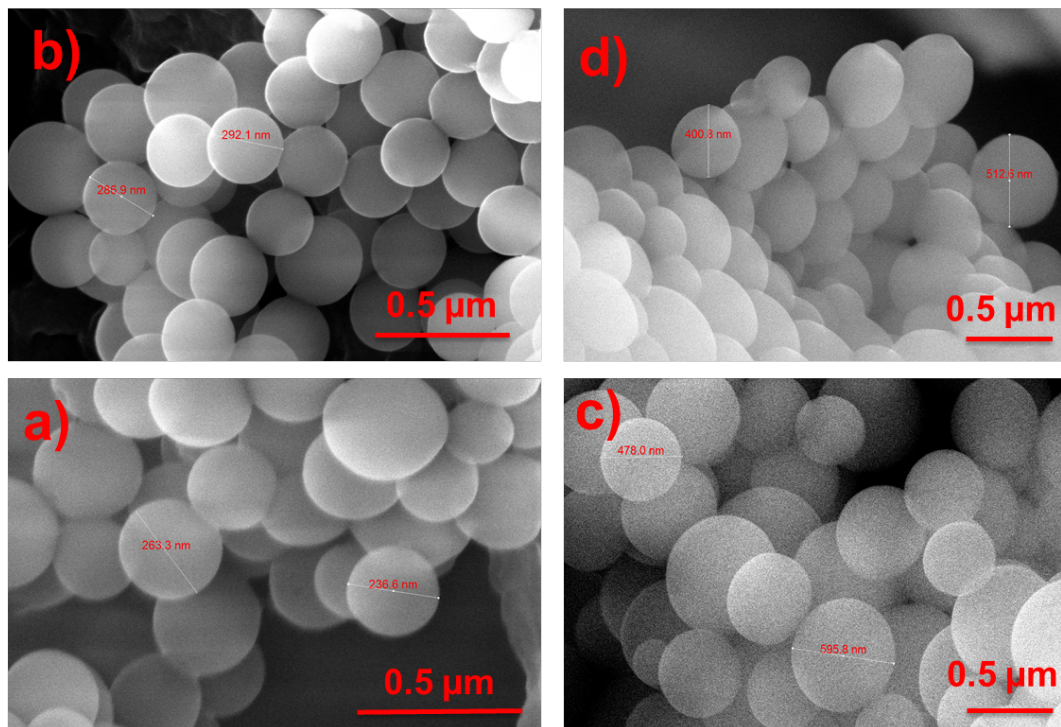
Figure 5-5. SEM images of (a) fluorinated NPs, (b) curcumin-loaded fluorinated NPs, (c) methylated NPs, and (d) curcumin-loaded methylated NPs.

Quercetin-loaded fluorinated NPs also increased in size (290±10 nm) (Figure 5-6

(a)), compared to the unloaded NPs (250±20 nm) (Figure 5-6 (b)); and this increase is

consistent with the DLS-obtained data. However, fluorinated NPs were deformed,

unsmooth in shape, after quercetin was loaded.
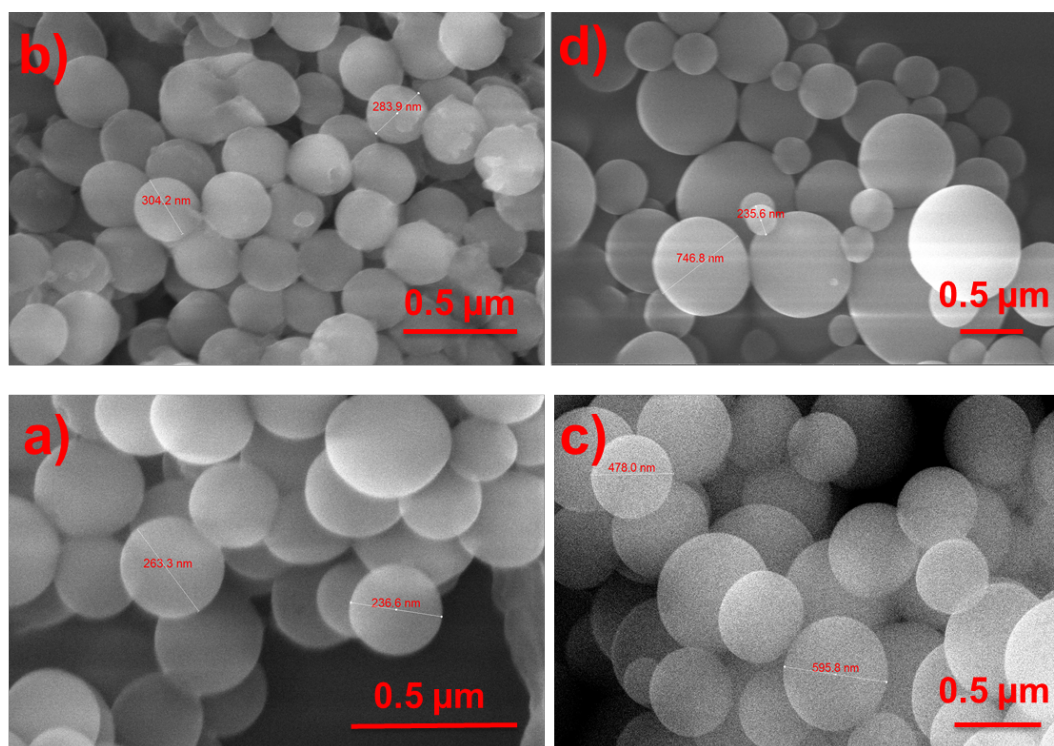
Figure 5-6. SEM images of (a) fluorinated NPs, (b) quercetin-loaded fluorinated NPs, (c) methylated NPs, and (d) quercetin-loaded methylated NPs.

Quercetin-loaded methylated NPs (Figure 5-6 (d)) didn't change in shape,

compared to the unloaded NPs (Figure 5-6 (c)); rather, bimodal NPs such as (235±5 nm

and 750±10 nm) were observed, compared to the unloaded NPs (540±50 nm) shown in

Figure 5-6 (c). This bimodal distribution is consistent with the DLS-analyzed sizes.

The transformation in the hydrophobicity after loading the drug molecules in fluorinated and methylated NPs' surfaces was studied using water contact angles, as shown in Figure 5-7 (a) and (b), respectively. Curcumin loading decreased the hydrophobicity in both fluorinated and methylated NPs, as the water contact angle dropped from 151°±1° to 136°±2° on the fluorinated NPs and 155°±1° to 142°±1° on the methylated NPs' surfaces. Similarly, quercetin loading also decreased the water contact angle on the NPs' surfaces, as water contact angle dropped from 151°±1° to 142°±2 on the fluorinated NPs and 155°±1° to 145°±1 on the methylated NPs' surfaces.
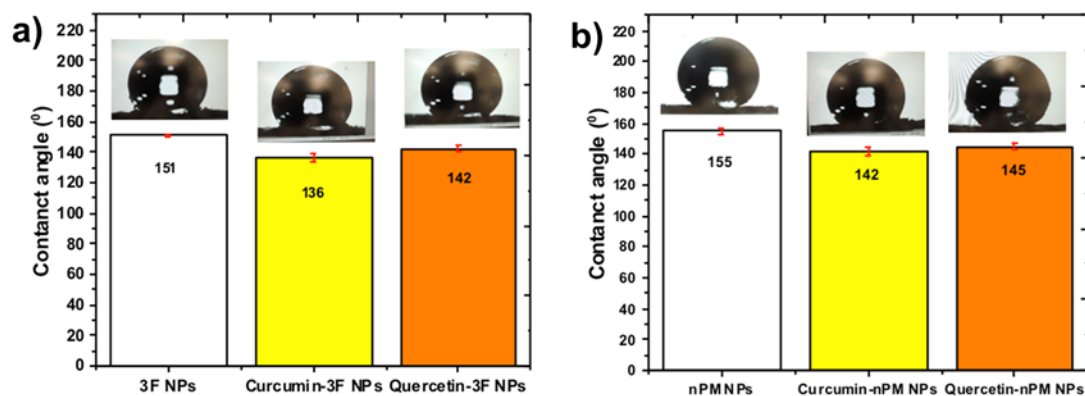
Figure 5-7. Static water contact angles measured on curcumin and quercetin-loaded (a) fluorinated NPs, and (b) methylated NPs' surfaces.

ATR-FTIR spectra of the curcumin and quercetin-loaded NPs confirmed the presence of these two drug molecules on the surface of both the fluorinated and

methylated NPs. ATR-FTIR spectra of curcumin-loaded fluorinated and methylated NPs

are shown in Figure 5-8 (a) and (b), respectively. The presence of the aromatic

functionality from 1490 cm^{-1} to 1690 cm^{-1} confirms the presence of curcumin on both the

fluorinated and methylated NPs' surface. The presence of fluorine functionality was

confirmed as the -CF bending stretch was observed at 1250 cm^{-1} and 840 cm^{-1}.
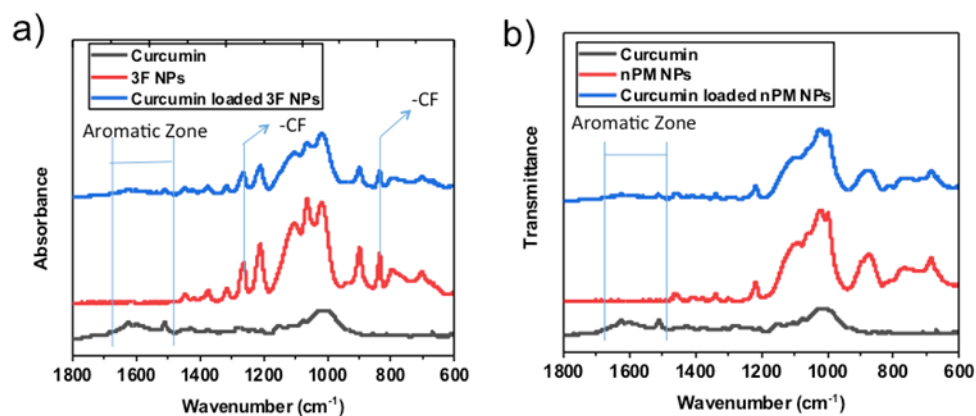
Figure 5-8. ATR-FTIR spectra of curcumin-loaded (a) fluorinated NPs, and (b)
methylated NPs.

Similarly, quercetin loading in both fluorinated and methylated NPs was
confirmed in the ATR-FTIR spectra shown in Figure 5-9 (a) and (b), respectively, with
the presence of the peak around the aromatic zones being 1490 cm^{-1} to 1690 cm^{-1}.
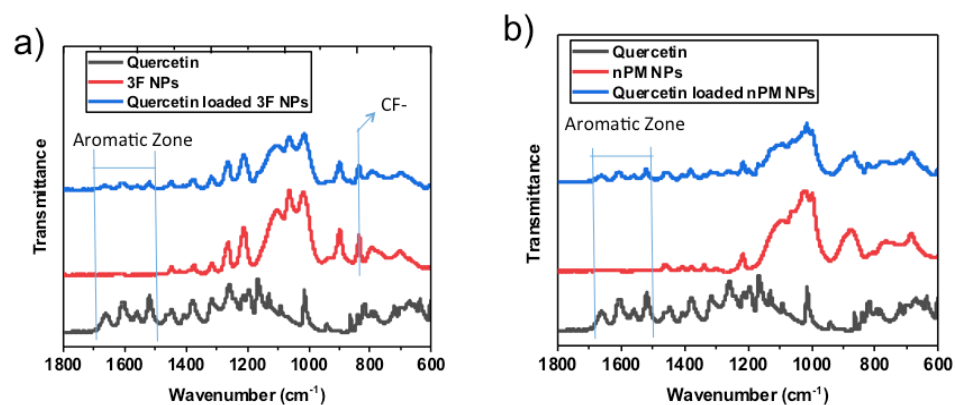
Figure 5-9. ATR-FTIR spectra of quercetin-loaded (a) fluorinated NPs, and (b) methylated NPs.

After the successful loading of curcumin and quercetin molecules in both fluorinated and methylated NPs, release kinetics of these drug molecules were also studied. The release kinetics of curcumin from the fluorinated and methylated NPs in the PBS solution showed that from both NPs, a quick burst of curcumin release occurred within 60±10 min, and then cumulative release reached the plateau after 300±10 min. However, only 20 % and 12 % of curcumin were released from the fluorinated and methylated NPs, respectively, after reaching the plateau (Figure 5-10).
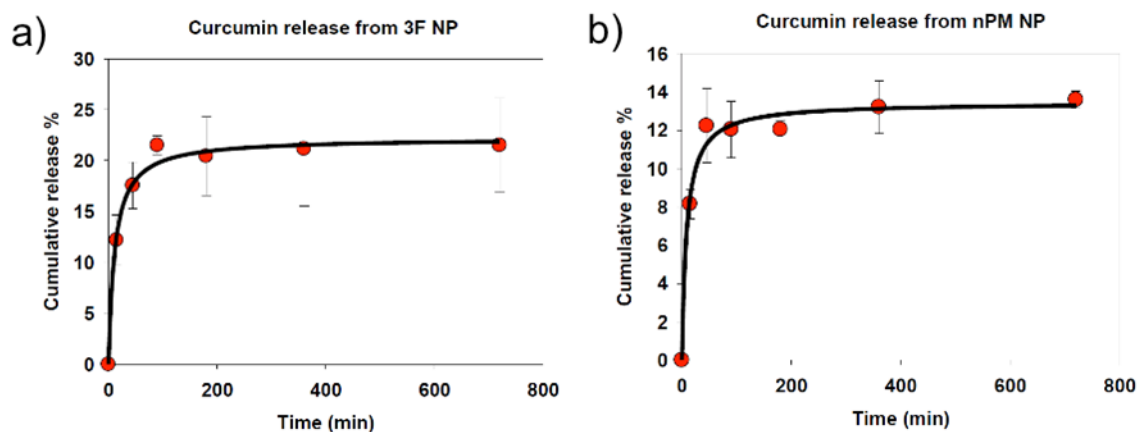
Figure 5-10. Release kinetics of curcumin from (a) fluorinated NPs, and (b) methylated NPs.

Unlike the curcumin release, quercetin release was slower from both fluorinated and methylated NPs, as shown in Figure 5-11 (a) and (b), respectively. After an initial burst of quercetin release within 100±20 min, a total of 32 % quercetin was released from the fluorinated NPs over 420±20 min, and 40 % of quercetin was released from the methylated NPs over 600±30 min, after reaching the plateau.

Ethanol dissolved curcumin and quercetin initially were dissolved in aqueous solution at pH 3.0, and later condensed to form NPs in basic solution (at pH ~ 9.5 to 10.0), by adding NH_4OH. Although curcumin is expected to be stable at a pH near 10.0, curcumin may be degraded at such high pH, which may reduce the curcumin's efficacy as a drug, as well as its loading efficiency. Nevertheless, the curcumin loading and release was a proof of concept, along with that of quercetin. The possible degradation

may be mitigated by the presence of the silane molecules, which can stabilize compounds (e.g. enzymes are encapsulated in silane porous glasses and are more stable against denaturing conditions).

The higher release % of quercetin from fluorinated and methylated NPs, compared to curcumin, means that these NPs are relatively better drug delivery vehicles for quercetin. As the time of the optimum release of curcumin and quercetin varies, they can be suitable to be used in different biological systems where faster or slower drug release is needed.
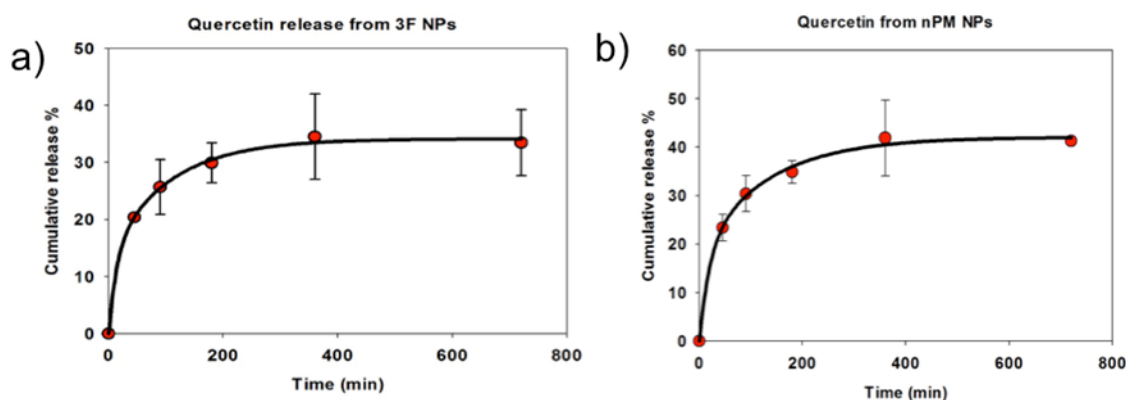
Figure 5-11. Release kinetics of quercetin from (a) fluorinated NPs, and (b) methylated NPs.

5.5 Conclusion

In this study, we successfully loaded two hydrophobic drug molecules, curcumin and quercetin, on fluorinated and methylated SHSN in a simple and environmentally

friendly aqueous system. The loading or conjugation of both the molecules was confirmed using different analytics tools such as DLS, AFM, and ATR-FTIR. The release kinetics of the drug molecules showed distinct behavior, as curcumin release was quicker and lesser than the quercetin release. Further study on the effect of the drug-loaded NPs against the biological cells could reveal the efficiency of these drug-loaded NPs.

5.6 References

1. Sharma, R. A.; Gescher, A. J.; Steward, W. P. *Eur. J. Cancer* **2005**, *41*, 1955.

2. Anand, P.; Thomas, G.; Kunnumakkara, A. B.; Sundaram, C.; Harikumar, K. B.; Sung, B.; Tharakan, S. T.; Misra, K.; Priyadarsini, I. K.; Rajasekharan, K. N.; Aggarwal, B. B. *Biochem. Pharmacol.* **2008**, *76*, 1590.

3. Maheshwari, R. K.; Singh, A. K.; GadDIpati, J.; Srimal, R. C. *Life Sci.* **2006**, *78*, 2081.

4. Chattopadhyay, I.; Biswas, K.; Bandyopadhyay, U.; Banerjee, R. K. *Curr. Sci.* **2004**, *87*, 44.

5. Senft, C.; Polacin, M.; Priester, M.; Seifert, V.; Kögel, D.; Weissenberger, J. *BMC Cancer* **2010**, *10* (491), 1.

6. Casagrande, R.; Georgetti, S. R.; Verri, Jr. W. A.; Dorta, D.J.; Santos, A. C.; Fonseca, M. J. J. *Photochem. Photobiol.* B **2006**, *84*, 21.

7. Cushnie, T. P.; Lamb, A. J. *Int. J. Antimicrob. Agents* **2005**, *26*, 343.

8. Ruiz, P. A.; Braune, A.; Holzlwimmer, G.; Quintanilla-Fend, L.; Haller, D. *J. Nutr.* **2007**, *137*, 1208.

9. Teixera, S.; Siquet, C.; Alves, C.; Boal, I.; Marques, P.; Borges, F.; Lima, J. L. F. C.; Reis, S. *Free RaDIc. Biol. Med.* **2005**, *39*, 1099.

10. Vicentini, F. T.; Fonseca, Y. M.; Pitol, D. L.; Iyomasa, M. M.; Bentley, M. V.; Fonseca, M. J. *J. Pharm. Pharmaceut. Sci.* **2010**, *13*, 274

11. Brietzke, E.; Mansur, R.B.; Zugman, A.; Carvalho, A.F.; Macêdo, D. S.; Cha, D. S.; Abílio, V. C.; McIntyre, R. S. *Med. Hypotheses* **2013**, *80*, 606.

12. Eckert, G. P.; Schiborr, C.; Hagl, S.; Abdel-Kader, R.; Müller, W. E.; Rimbach, G.; Frank, *J. Neurochem. Int.* 2013, *62*, 595.

13. Celik, A.; Eke, D.; Ekinci, S. Y.; Yıldırım, S. *Food Chem. Toxicol.* **2013**, *53*, 249.

14. Lee, G. H.; Lee, S. J.; Jeong, S. W.; Kim, H.; Park, G. Y.; Lee, S. G.; Choi, J. H. *Colloids and Surfaces B: Biointerfaces* **2016**, *143*, 511.

15. Gaysinsky, S.; Davidson, P. M.; Bruce, B. D.; Weiss, J. *J. Food Prot.* **2005**, *68*, 1359.

16. Pralhad, T.; Rajendarkumar, K. *J. Pharm. Biomed. Anal.* **2004**, *4*, 333.

17. Anand, P.; Kunnumakkara, A. B.; Newman, R. A.; Aggarwal, B. B. *Mol. Pharmaceutics* **2007**, *4*, 807.

18. Gosangari, S.; Dyakonov, T. *Pharm. Dev. Technol.* **2013**, *18*, 475.

19. Zhou, N.; Zan, X.; Wang, Z.; Wu, H.; Yin, D.; Liao, C.; Wan, Y. *Carbohydr. Polym.* **2013**, *94*, 420.

20. Ahmed, K.; Li, Y.; McClements, D. J.; Xiao, H. *Food Chem.* **2012**, *132*, 799.

21. Bhawana; Basniwal, R. K.; Buttar, H. S.; Jain, V. K.; Jain, N. *J. Agric. Food Chem.* **2011**, *59*, 2056.

22. Tikekar, R. V.; Pan, Y.; Nitin, N. *Food Res. Int.* **2013**, *51*, 370.

23. Mourtas, S.; Canovi, M.; Zona, C.; Aurilia, D.; Niarakis, A.; Ferla, B. L.; Salmona, M.; Nicotra, F.; Gobbi, M.; Antimisiaris, S. G. *Biomaterials* **2011**, *32*, 1635.

24. Song, Z.; Feng, R.; Sun, M.; Guo, C.; Gao, Y.; Li, L.; Zhai, G. *J. Colloid Interface Sci.* **2011**, *354*, 116.

25. Liu, L.; Sun, L.; Wu, Q.; Guo, W.; Li, L.; Chen, Y.; Li, Y.; Gong, C.; Qian, Z.; Wei, Y. *Int. J. Pharm.* **2013**, *443*, 175.

26. Tapal, A.; Tiku, P. K. *Food Chem.* **2012**, *130*, 960.

27. Bettini, S.; Vergara, D.; Bonsegna, S.; Giotta, L.; Toto, C.; Chieppa, M.; Maffia, M.; Giovinazzo, G.; Valli, L.; Santino, A. *RSC Adv.* **2013**, *3*, 5422.

28. Lin, C.; Lin, H.; Chen, H.; Yu, M.; Lee, M. *Food Chem.* **2009**, *116*, 923.

29. Priprem, A.; Watanatorn, J.; Sutthiparinyanont, S.; Phachonpai, W.; Muchimapura, S. *NanomeDIcine* **2008**, *4*, 70.

30. Zhang, Y.; Yang,Y.; Tang, K.; Hu, X.; Zou, G. *J. Appl. Polym.Sci.* **2008**, 107, 891

31. Weetal, H. H. *Biochim. Biophys. Acta* **1970**, *212* (1), 1.

32. Avnir, D.; Braun, S.; Lev, O.; Ottolenghi, O. *Chem. Mater.* **1994**, *6*, 1605.

33. Shimada, M.; Shoji, N.; Takahashi, A. *Anticancer Res.* **1995**, *15*, 109.

34. Jain, T. K., Roy, I.; Maitra, A. N. *J. Am. Chem. Soc.* **1998**, *120*, 11092.

35. Lal, M.; Levy, L.; Kim, K. S.; He, G. S.; Wang, X.; Min, Y. H.; Pakatchi, S.; Prasad, P. N. *Chem. Mater.* **2000**, *12*, 2632.

36. Roy, I.; Ohulchanskyy, T. Y.; Pudavar, H. E.; Bergey, E. J.; Oseroff, A. R.; Morgan,J.; Dougherty, T. J.; Prasad, P. N. *J. Am. Chem. Soc.* **2003**, *125*, 7860.

37. YilDIrim, A.; Budunoglu, H.; Daglar, B.; Deniz, H.; BayinDIr, M. *ACS Appl. Mater. Interfaces* **2011**, *3*, 1804.

38. J. D. Brassard, J. D.; Sarkar, D. K.; Perron, J. *ACS Appl. Mater. Interfaces.* **2011**, *3*, 3583.

39. Stöber, W.; Fink, A.; Bohn, E. *J. Colloid Interface Sci.* **1968**, *26* (1), 62.

CHAPTER 6

SILICA AND SPIDER SILK-BASED NANOCOMPOSITES SYNTHESIS

6.1 Abstract

This study introduced a simple and environmentally friendly method to synthesize silica and spider silk protein-based nanocomposites. Prior to synthesis of the nanocomposites, spider silk protein and silica precursors were dissolved and mixed in aqueous solution, using microwave technology. Both SEM and AFM images showed that the synthesized fluorinated spider silk-silica nanocomposites were a mixture of two types of spherical NPs with the size < 100 nm and > 300 nm attached to each other. However, methylated spider silk-silica nanocomposites were nanoaggregates with a mixture of irregular-shaped nanospheres with the sizes < 200 nm. Deconvoluted ATR-FTIR spectra confirmed the occurrence of conformational changes in the spider silk proteins during their integration with fluorinated and methylated silica to form the nanocomposites. Total amount of β structures increased by 10% in the spider silk-methylated silica nanocomposites, compared to the spider silk protein, but decreased by 28% in the spider silk-silica nanocomposites. Increased β structures can enhance the strength of the spider silk and overall nanocomposites.

6.2 Introduction

Protein-based composite materials have vast applications in biomedical fields such as immunology, cancer research, and drug delivery. (1-4) These composite materials are also useful in material science areas such as self-assembled materials, quantum dot bioconjugates, sensors, and inorganic materials synthesis. (5-11) Silica particles are widely used in industry, medicine, and nanotechnology (12, 13); and silica-based biomaterials have potential applications in tissue engineering and drug delivery systems. (14) Recombinant spider silk protein (rSSP) is a promising biomaterial with huge potential in textiles, and in the biomedical and manufacturing industry, in the form of fibers, films, hydrogels, lyogels, and adhesives. (15-21) Recently, spider silk-based materials have shown great promise to attach and proliferate fibroblast cells. (22-27)

In the earlier chapters, we have shown that hydrophobic n-propyltrimethoxy silane (nPM) and 3,3,3-trifluoropropyl trimethoxy silane (3F) both can induce the secondary structures of the protein in their hydrolyzed state, and afterward, composite particles consisting of protein and silica can be formed in the condensation process. Thus, we hypothesize that nPM and 3F can induce spider silk proteins in their hydrolyzed state, and nanocomposites consisting of spider silk and silica can be synthesized by condensing the dissolved spider silk and nPM / 3F mix. The objective of this study was to synthesize

spider silk-silica-silica nanocomposites from an aqueous mix of nPM / 3F and spider silk protein.

We have successfully synthesized a new type of spider silk-silica nanocomposites from spider silk and an nPM / 3F-mix aqueous solution. The synthesized spider silk-silica nanocomposites have improved properties due to the controlled growth of nanoscale organic-inorganic interfaces and composite structural features. Our synthesized nanocomposites can be used to optimize the mechanical function and stability of biomaterials. These nanocomposites also can be used in immunology, cancer research, drug delivery devices, and biosensors.

6.3 Experimental procedure

Materials

3,3,3-trifluoropropyl trimethoxy silane (3F, > 95 % purity, MW = 218.3, d = 1.14 g/ml) and n-propyltrimethoxy silane (nPM, > 95 % purity, MW = 164.3, d = 0.94 g/ml) were purchased from Gelest, Inc. (Morrisville, PA). 50 % (w/w) NH_4OH was purchased from Fisher Scientific. Muscovite mica was purchased from SPI supplies for AFM study (PA, USA); and AFM tips were obtained from TED Pella Inc., CA (TAP300AL-G-50). Two different types of rSSP protein, major ampullate silk protein rMaSp1 and major ampullate silk protein rMaSp2, were purified from the milk of transgenic goats through tangential flow filtration, precipitation, and washing.

Synthesis of spider silk-silica nanocomposites

At first, 3F (0.4 M) and nPM (0.4 M) were hydrolyzed at pH 3.0 in aqueous media in separate vials. Two rSSP proteins (rMaSp1and rMaSp2) were mixed in a ratio of 50:50 and added in the H3F and HnPM media separately. These mixed solutions were then microwaved (Haier microwave (700 W)) for 8 seconds for 4 times in a tightly closed glass vial to dissolve the rSSPs. In between every cycle of microwave heating, 30 sec breaks were taken.
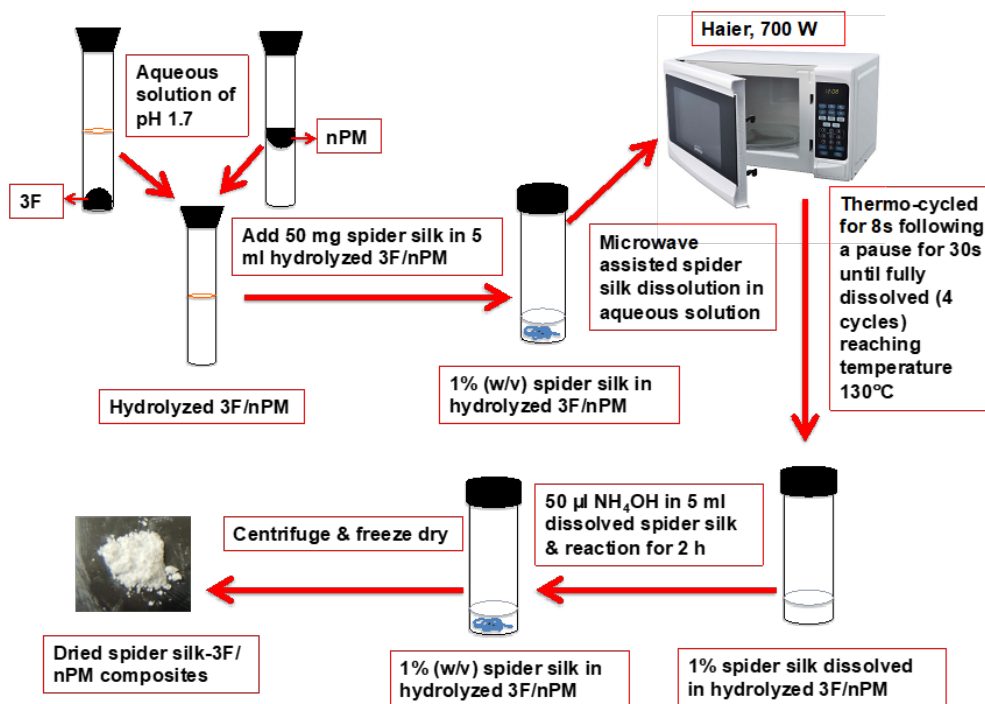
Figure 6-1. Schematic of Experimental procedure of the spider silk and 3F / nPM nanocomposite materials.

Once the temperature reached 130°C, all rSSPs were dissolved in the aqueous silane media. Hot and dissolved rSSPs in silane aqueous solutions were then cooled down to 23°C, using ice water bath. Then, NH_4OH was added to these rSSPs mixed solutions, following the Stöber method, to synthesize silica-spider silk nanocomposite materials. Synthesized composite materials were centrifuged and washed two times in DI water before they were lyophilized overnight. The experimental schematic is shown in Figure 6-1.

Characterization of spider silk-silica nanocomposites

Dried nanocomposite materials were analyzed using image analysis tools such as SEM, and AFM to determine their sizes and shapes. SEM was performed with a FEI Quanta FEG 650 equipped with an Oxford X-Max Energy Dispersive X-ray Spectroscopy (EDS) housed in the Microscopy Core Facility at Utah State University. Samples were imaged with 20 kV accelerating potential without conductive coatings. AFM images were taken using a Nanoscope III Bioscope (Digital Instrument, Inc.) in tapping mode. 100 µl samples were dropped on freshly cleaved mica surfaces, then gently washed with DI water, and air-dried before taking AFM images.

Bonding between spider silk protein (rSSP) and both fluorinated and methylated silica were analyzed by FTIR using a Varian 660-IR with a horizontal single reflection

Pike Technologies MIRacle attenuated total reflectance (ATR) unit, fitted with a ZnSe crystal. 100 µl samples were drop cast on the ZnSe crystal of the ATR platform and air-dried before taking the reading. Readings were taken after averaging 20 scans over the range of 600 cm^{-1} to 1800 cm^{-1}, with a resolution of 1 cm^{-1}. Prior to each reading, a background scan was acquired. The ATR-FTIR spectra were later deconvoluted, to analyze the transformation in the secondary structures of spider silk protein.

6.4 Result and Discussion

Figure 6-2 shows the SEM images of spider silk-silica nanocomposites along with the fluorinated and methylated silica NPs. Spider silk-methylated silica nanocomposites shown in Figure 6-2 (b) were in aggregated or clogged form. These spider silk-methylated silica nanocomposites were built on smaller (<200 nm) nanoparticulates with irregular-shaped spheres (Figure 6-2 (b), compared to the monodispersed methylated NPs (540±50 nm) (Figure 6-2 (a)).
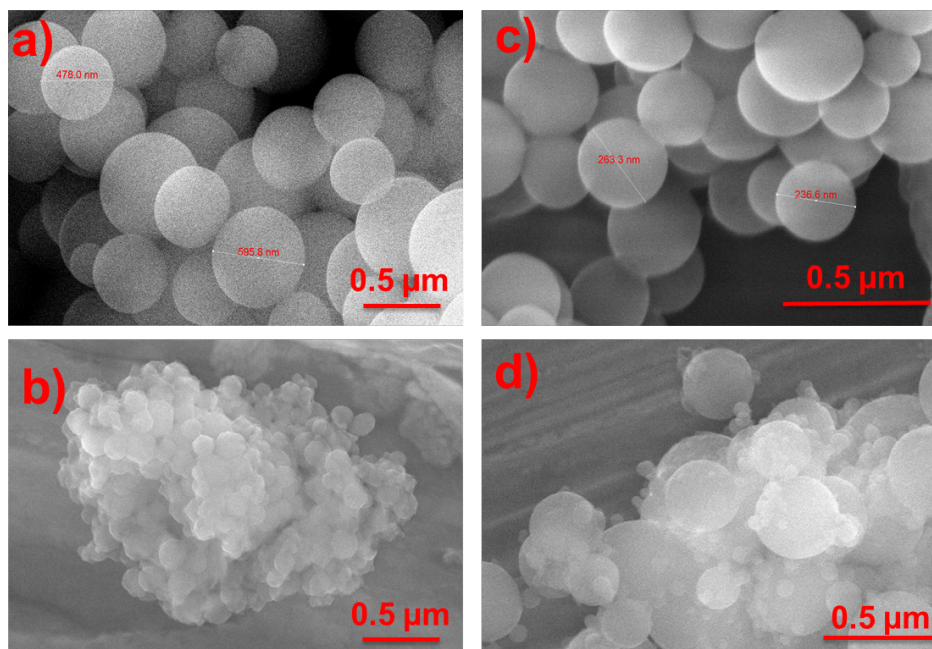
Figure 6-2. SEM images of (a) methylated silica NPs, (b) spider silk-methylated nanocomposites, (c) fluorinated silica NPs, and (d) spider silk-fluorinated nanocomposites.

Spider silk-fluorinated silica nanocomposites (Figure 6-2 (d)) consisted of two types of particles, NPs with size of <100 nm and >300 nm. These bimodal NPs were attached to each other to form the nanocomposites, unlike the fluorinated NPs where NPs were monodispersed with the size of 250±20 nm (Figure 6-2 (c)).
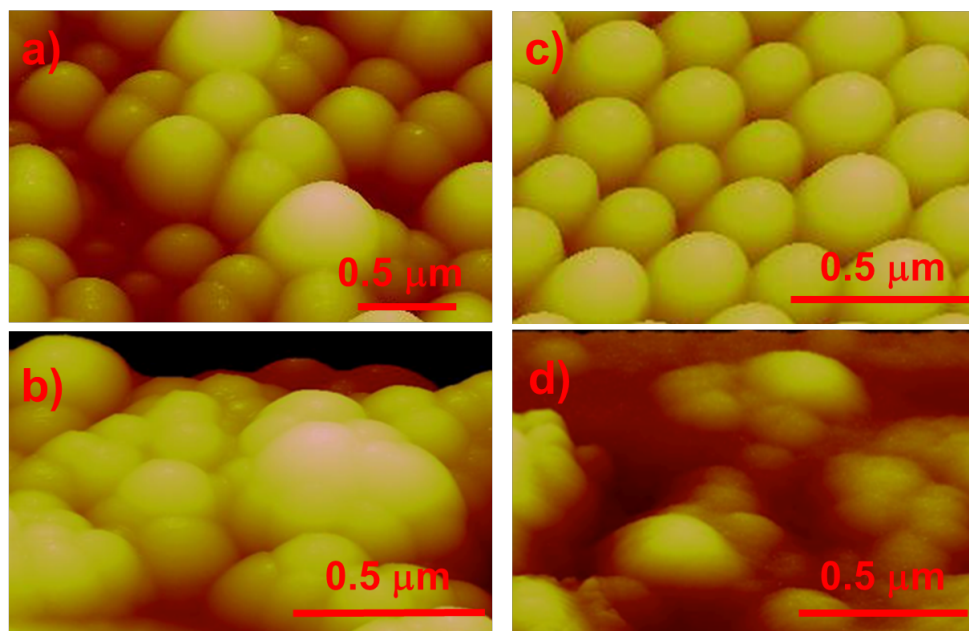
Figure 6-3. AFM images (a) methylated silica NPs, (b) fluorinated silica NPs, (c) spider silk-methylated nanocomposite, and (d) spider silk-fluorinated nanocomposites.

3D images of the nanocomposites obtained from the AFM further confirmed these characteristics of the spider silk-methylated silica nanocomposites (Figure 6-3 (b)) and spider silk-fluorinated nanocomposites (Figure 6-3 (d)), along with the methylated and fluorinated silica NPs in Figure 6-3 (a) and Figure 6-3 (c), respectively.

ATR-FTIR spectra (Figure 6-4) showed some major conformational changes in the amide I zone (1575 cm^{-1} to 1725 cm^{-1}) of spider silk protein within the spider silk-methylated nanocomposites (SS-nPM) and the spider silk-fluorinated nanocomposites (SS-3F).
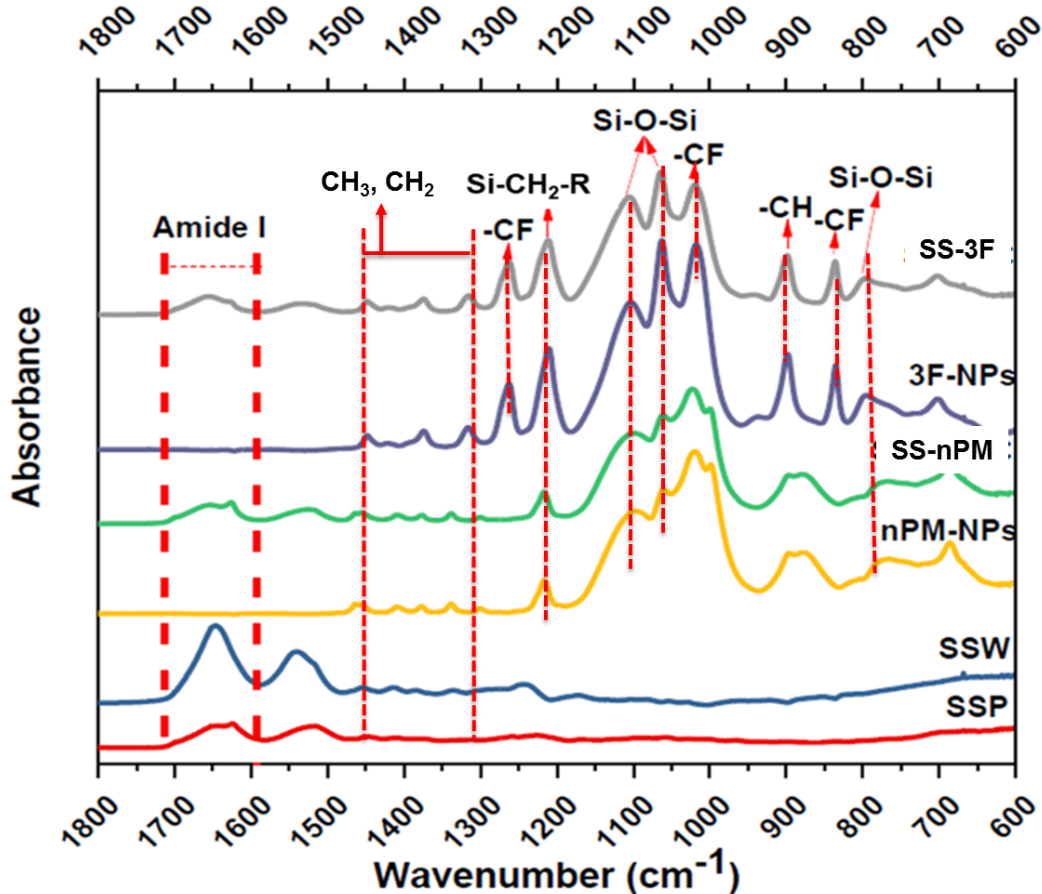
Figure 6-4. ATR-FTIR spectra of methylated silica NPs (nPM-NPs), fluorinated silica NPs (3F-NPs), spider silk-methylated silica nanocomposites (SS-nPM), and spider silk-fluorinated silica nanocomposites (SS-3F). SSP and SSW represent the spectra for the spider silk in powder and spider silk in aqueous states.

Figure 6-4 also includes spectra for methylated silica NPs (nPM-NPs), fluorinated silica NPs (3F-NPs), spider silk in powder (SSP), and aqueous states (SSW). Other than amide I zone, other bending and stretching peaks were shown in the respected spectra. Spectra representing 3F-NPs and SS-3FC, showed –CF peaks at 840 cm^{-1}, 1020 cm^{-1}, and

1260 cm^{-1}. Peaks representing Si-O-Si (800 cm^{-1}, 1060 cm^{-1}, and 1100 cm^{-1}), and Si-CH$_2$-R (1210 cm^{-1}) were visible in all the spectra, SS-nPM, SS-3F, nPM-NPs, and 3F-NPs, confirming the integration of the spider silk in the nanocomposites. Also, the peaks for CH$_3$, CH$_2$ (1320-1450 cm^{-1}) and –CH (900 cm^{-1}) were visible in all the spectra, including SSP and SSW. Later, spectra were deconvoluted, to quantify the transformation in their secondary structures in the nanocomposites in the amide I zone.

The deconvoluted FTIR spectra of SSP, SS-nPM, and SS-3F are shown in Figure 6-5 (a), (b) and (c), respectively. Figure 6-5 (d) shows the quantified secondary structure % in the corresponding spider silk proteins. In SS-3F, β-sheet was reduced by 18 % and β-turn reduced by 10 %, compared to the % of these secondary structures in SSP. However, a new secondary structure, a 3_{10}-helix appeared in SS-3F spectra, and this 3_{10}-helix was 35 % of the total secondary structures available in SS-3F.
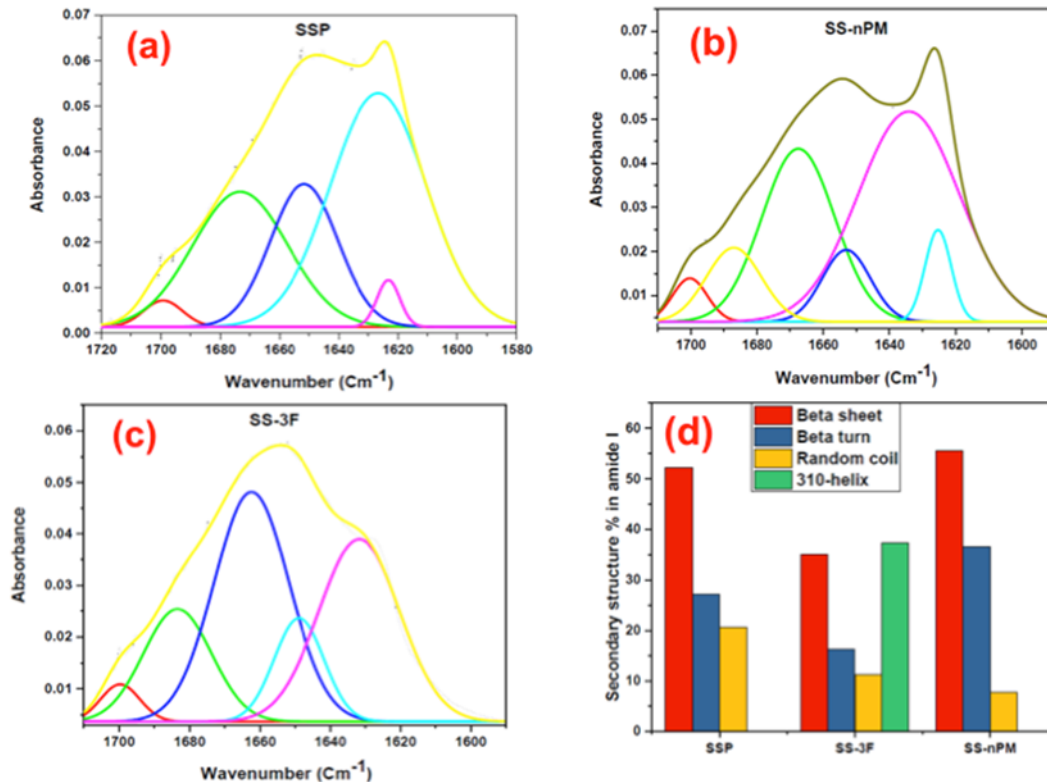
Figure 6-5. Deconvoluted ATR-FTIR spectra of (a) spider silk powder (SSP), (b) spider silk-methylated silica NPs (SS-nPM), (c) spider silk-fluorinated silica NPs (SS-3F), and (d) conformational change in secondary structures of BLG.

An opposite trend was observed in the secondary structures of the spider silk in SS-nPM, where both β structures (sheet and turn) increased. In these nanocomposites, β-sheet increased by 3 % and β-turn increased by 7 %. These patterns of conformational changes in the secondary structures of SSP are consistent with conformational changes observed in BLG protein, described in Chapter 3.

6.5 Conclusion

We successfully synthesized spider silk-fluorinated and methylated nanocomposites. SEM and AFM images showed that the integration of spider silk protein with both fluorinated and methylated silica resulted in non-spherical nanocomposites with distinct morphologies, contrasted with the control images of pure silanes. Strong amide I and II peaks in the ATR-FTIR spectra further confirmed the integration of the spider silk protein in the nanocomposites. Deconvoluted ATR-FTIR spectra showed increased β structures in SS-nPM and decreased β structures in the SS-3F. SS-nPM can be potentially stable against organic solvent, water, and strong acid and bases, due to the assembly of highly stable β-sheets with high mechanical properties. Also, aqueous synthesis of these nanocomposite materials makes them suitable for integration with living tissues. These hybrid silica-protein structures have the potential to exhibit unique biological activities, which will make them suitable for versatile biomedical applications.

6.6 References

1. Albarran, B.; To, R.; Stayton, P. S. *Protein Eng. Des. Selection* **2005**, *18*, 147.

2. Asai, T.; Trinh, R., Ng, P. P.; Penichet, M. L.; Wims, L. A.; Morrison, S. L. *Biomol. Eng.* **2005**, *21*, 145.

3. Icke, C.; Schlott, B.; Ohlenschlager, O.; Hartmann, M.; Guhrs, K. H.; Glusa, E. *Mol. Pharmacol.* **2002**, *62*, 203.

4. Park, E.; Starzyk, R. M.; McGrath, J. P.; Lee, T.; George, J.; Schutz, A. J.; Lynch, P.; Putney, S. D. *J. Drug Targeting* **1998**, *6*, 53.

5. Dubrovsky, T.; Tronin, A.; Dubrovskaya, S.; Guryev, O.; Nicolini, C. *Thin Solid Films* **1996**, *285*, 698.

6. Frey, W.; Meyer, D. E.; Chilkoti, A. *Adv. Mater.* **2003**, *15*, 248.

7. MeDIntz, I. L.; Uyeda, H. T.; Goldman, E. R.; Mattoussi, H. *Nat. Mater.* **2005**, *4*, 435.

8. PaDIlla, J. E.; Colovos, C.; Yeates, T. O. *Proc. Natl. Acad. Sci. U.S.A.* **2001**, *98*, 2217.

9. Paternolli, C.; Ghisellini, P.; Nicolini, C. *Mater. Sci. Eng. C* **2002**, *22*, 155.

10. Sleytr, U. B.; Schuster, B.; Pum, D. *IEEE Eng. Med. Biol. Mag.* **2003**, *22*, 140.

11. Slocik, J. M.; Naik, R. R.; Stone, M. O.; Wright, D. W. *J. Mater. Chem.* **2005**, *15*, 749.

12. Tan, W.; Wang, K.; He, X.; Zhao, X. J.; Drake, T.; Wang, L.; Bagwe, R. P. *Med. Res. Rev.* **2004**, *24*, 621.

13. CoraDIn, T.; Livage, J. *Acc. Chem. Res.* **2007**, *40*, 819.

14. Hardy, J. G.; Torres-Rendon, J. G.; Leal-Egaña, A.; Walther, A. Schlaad, H.; Cölfen, H.; Scheibel, T. R. *Materials* **2016**, *9* (7), 560.

15. Mieszawska, A. J.; Fourligas, N.; GeorgakouDI, I.; Ouhib, N. M.; Belton, D. J.; Perry, C. C.; Kaplan, D. L. *Biomaterials* **2010**, *31* (34), 8902.

16. Teule, F.; AdDIson, B.; Cooper, A. R.; Ayon, J.; Henning, R. W.; Benmore, C. J.; Holland, G. P.; Yarger, J. L.; Lewis, R. V. *Biopolymers* **2012**, *97*, 418.

17. An, B.; Jenkins, J. E.; Sampath, S.; Holland, G. P.; Hinman, M.; Yarger, J. L.; Lewis, R. *Biomacromolecules* **2012**, *13*, 3938.

18. Xia, X. X.; Qian, Z. G.; Ki, C. S.; Park, Y. H.; Kaplan, D. L.; Lee, S. Y. *Proc. Natl. Acad. Sci. U.S.A.* **2010**, *107*, 14059.

19. Minoura, N.; Aiba, S.-I.; Gotoh, Y.; Tsukada, M.; Imai, Y. *J. Biomed. Mater. Res.* **1995**, *29*, 1215.

20. Morgan, A. W.; Roskov, K. E.; Lin-Gibson, S.; Kaplan, D. L.; Becker, M. L.; Simon, C. G. Jr. *Biomaterials* **2008**, *29*, 2556.

21. Sofia, S.; McCarthy, M. B.; Gronowicz, G.; Kaplan, D. L. *J. Biomed. Mater. Res.* **2001**, *54*, 139.

22. Baoyong, L.; Jian, Z.; Denglong, C.; Min, L. *Burns* **2010**, *36*, 891.

23. Hijirida, D. H.; Do, K. G.; Michal, C.; Wong, S.; Zax, D.; Jelinski, L. W. *Biophys. J.* **1996**, *71*, 3442.

24. Gomes, S.; Leonor, I. B.; Mano, J. F.; Reis, R. L.; Kaplan, D. L. *Biomaterials* **2011**, *32*, 4255.

25. Teule, F.; Cooper, A. R.; Furin, W. A.; Bittencourt, D.; Rech, E. L.; Brooks, A.; Lewis, R. V. *Nat. Protoc*. **2009**, *4*, 341.

26. Albertson, A. E.; Teule, F.; Weber, W.; Yarger, J. L.; Lewis, R. V. *J. Mech. Behav. Biomed. Mater.* **2014**, *29*, 225.

27. Gomes, S.; Gallego-Llamas, J.; Leonor, I. B.; Mano, J. F.; Reis, R. L.; Kaplan, D. L. *Macromol. Biosci.* **2013**, *13*, 444.

CHAPTER 7

HYDROPHOBIC SILANE-MODULATED SPIDER SILK FILMS

7.1 Abstract

Hydrophobic silane-modulated spider silk protein-based films were prepared in an aqueous system. Hydrophobicity was higher on the silane-modulated spider silk film surface, as water contact angle increased to 98° from 82° on the unmodulated spider silk film surface. The presence of the methylated functionality in the silane-modulated films was confirmed by ATR-FTIR spectra. The AFM-analyzed images showed that surface roughness was higher on the silane-modulated spider silk films (9.83 nm), compared to the unmodulated spider silk films (5.23 nm), which enhances their applicability in the biomedical field.

7.2 Introduction

Recombinant spider silk protein (rSSP) fibers have a variety of applications in textiles, and in the biomedical and manufacturing industries. (1−10) The extraordinary mechanical strength of rSSP comes from its β-sheet-dominated secondary structures. (11) Along with the production of fibers, significant efforts have been made to investigate the alternative forms of rSSP, such as films, hydrogels, lyogels, and adhesives. (2−4, 12-14) rSSP-based films have been studied for their biomedical applications such as attachment

of fibroblasts, osteoblast-like cells, and skin cells. (7−11, 15) These rSSP films also have shown promise in medical devices, skin grafts, drug delivery devices, and cellular scaffolds. (16-21) Unlike the fibers, films don't need to be woven together after processing, to make the functional products. Thus, spider silk films are cost effective, compared to fiber products. rSSP-based films are produced by simply formulating and pouring a dope, which can easily be modified by changing the formulation to have increased cell attachment, drug release, and mechanical properties. (20, 22-24)

rSSP are insoluble in aqueous solutions, and conventionally they are dissolved in 1,1,1,3,3,3-hexafluoro-2-propanol (HFIP) to generate dopes to create fibers, films, gels, and foams. (25-28) However, HFIP residues carry risk to human health and to the environment; and moreover, HFIP is not a cost-effective way to dissolve rSSP. Recently, a simple microwave method has been introduced to dissolve rSSPs in aqueous solution, replacing HFIP, which is not only cost-effective but also addresses the human health issue as well as environmental concerns. (29)

Alkoxysilanes are often used as the precursor for silicone, a widely used adhesive to bridge inorganic materials with organic molecules. (30) Hydrolyzed nPM (HnPM) have shown their ability to induce the secondary structures of the protein and increase the β-sheets. (31) Thus, we hypothesized that nPM-induced rSSP in aqueous solution can generate spider silk films with higher surface properties. In this study, we attempted to

modulate the secondary structure of rSSP by HnPM in aqueous system and investigate

the possible improvement in surface properties of silane-modulated rSSP films.

7.3 Experimental procedure

Materials

n-propyltrimethoxy silane (nPM, > 95 % purity, MW = 164.3, d = 0.94 g/ml) was

purchased from Gelest, Inc. (Morrisville, PA); and 50 % (w/w) NH_4OH was purchased

from Fisher Scientific. Muscovite mica was purchased from SPI supplies for the AFM

study (PA, USA); and AFM tips were obtained from TED Pella Inc., CA (TAP300AL-G-

50). Two different types of rSSP protein, major ampullate silk protein rMaSp1 and major

ampullate silk protein rMaSp2, were purified from the milk of transgenic goats through

tangential flow filtration, precipitation, and washing.

Forming spider silk films

The mold for the water-based films was made from a polydimethylsiloxane

PDMS (Dow Corning) solution of 10:1 base to initiator, and poured into a 90 mm Petri

dish to an approximately 1 mm thickness. The Petri dish and solution was then placed

into a vacuum chamber for 20 min to remove all bubbles. They were then placed in an

oven at 70 °C to cross-link overnight. The solidified PDMS was removed and cut using a

forceps and a razor blade to four 30 × 7 mm strips. The mold was then thoroughly

cleaned using soap and water, followed by isopropanol (IPA). 5 % (w/v) rSSPs were

dissolved in aqueous solution with or without the presence of HnPM (0.4 M). The

dissolved spider silk solutions were then poured on PDMS structures and dried overnight

at room temperature.

Characterization of silane-modulated spider silk films

The water contact angle was measured with a VCA optima digital contact angle

instrument (AST products, Billerica, MA); on the surface of the films using 10 μl sessile

drops of DI water. AFM images were taken to find the possible change in the silane-

modulated spider silk films, compared to spider silk films. AFM images were taken using

a Nanoscope III Bioscope (Digital Instrument, Inc.) in tapping mode. 100 μl samples

were dropped on freshly cleaved mica surfaces, then gently washed with DI water, and

air-dried before taking AFM images.

Both types of films were analyzed with FTIR, using a Varian 660-IR with a

horizontal single reflection Pike Technologies MIRacle attenuated total reflectance

(ATR) unit, fitted with a ZnSe crystal. 100 μl samples were drop cast on the ZnSe crystal

of the ATR platform, and air-dried before taking the reading. Readings were taken after

averaging 20 scans over the range of 600 cm^{-1} to 1800 cm^{-1} with a resolution of 1 cm^{-1}.

Prior to each reading, a background scan was acquired.

7.4 Result and Discussion

The static water contact angles on rSSP film and nPM-modulated rSSP film are

shown in Figure 7-1 (a) and (b), respectively. Water contact angle on nPM-modulated

rSSPs films was 98±2°, compared to 82±2° on the rSSP films. This increase in contact

angle implies that silane modulation has improved the hydrophobicity of the rSSP films.

The silane modulation increased the % of sheet structures in rSSP, which eventually

improved the hydrophobicity of their films.
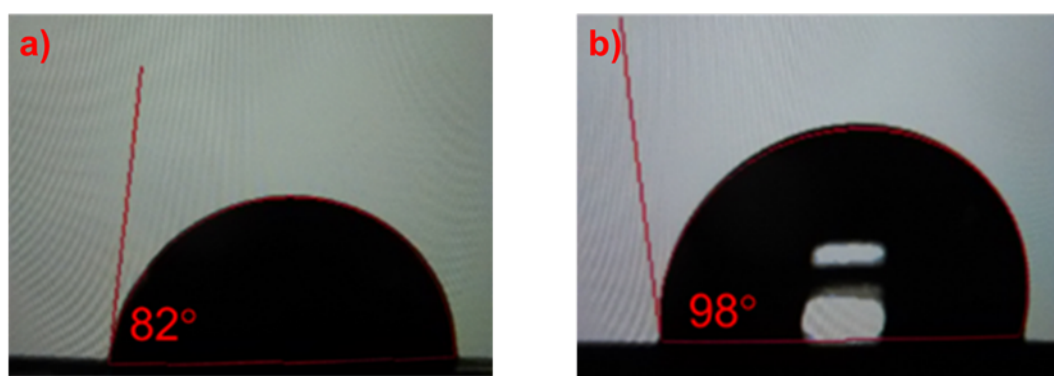
Figure 7-1. Static water contact angle on (a) rSSP film and (b) nPM-modulated rSSP film.

The ATR-FTIR spectrum of nPM-modulated rSSP film showed a shift towards

the β structures (> 1660 cm^{-1}) in the amide I zone (Figure 7-2), compared to the spectrum

of the unmodulated film. Also, the intensity of the peak around 1655-1660 cm^{-1}

increased, which could be due to the increase in sheet structures in rSSP. The increase of

intensity at the CH$_3$- CH$_2$- bending vibration region (1300-1450 cm^{-1}) further confirmed

the silane modulation in the rSSP film.
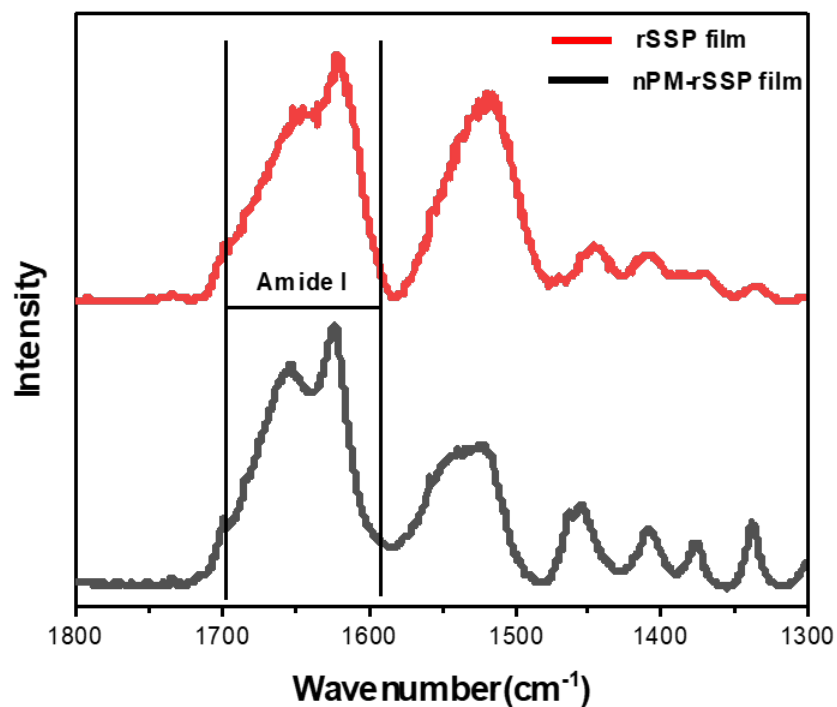
Figure 7-2. ATR-FTIR spectra of rSSP and nPM-modulated rSSP film.

AFM images of rSSP and nPM-modulated rSSP films, along with corresponding height profiles on the surfaces, are shown in Figure 7-3. Silane modulation increased the surface roughness of the film, as RMS roughness values were 5.23 nm and 9.83 nm on the rSSP and on the nPM-modulated rSSP film, respectively. This increase in surface roughness indicates that the adhesive property of the rSSP film was enhanced by the nPM modulation. (32)
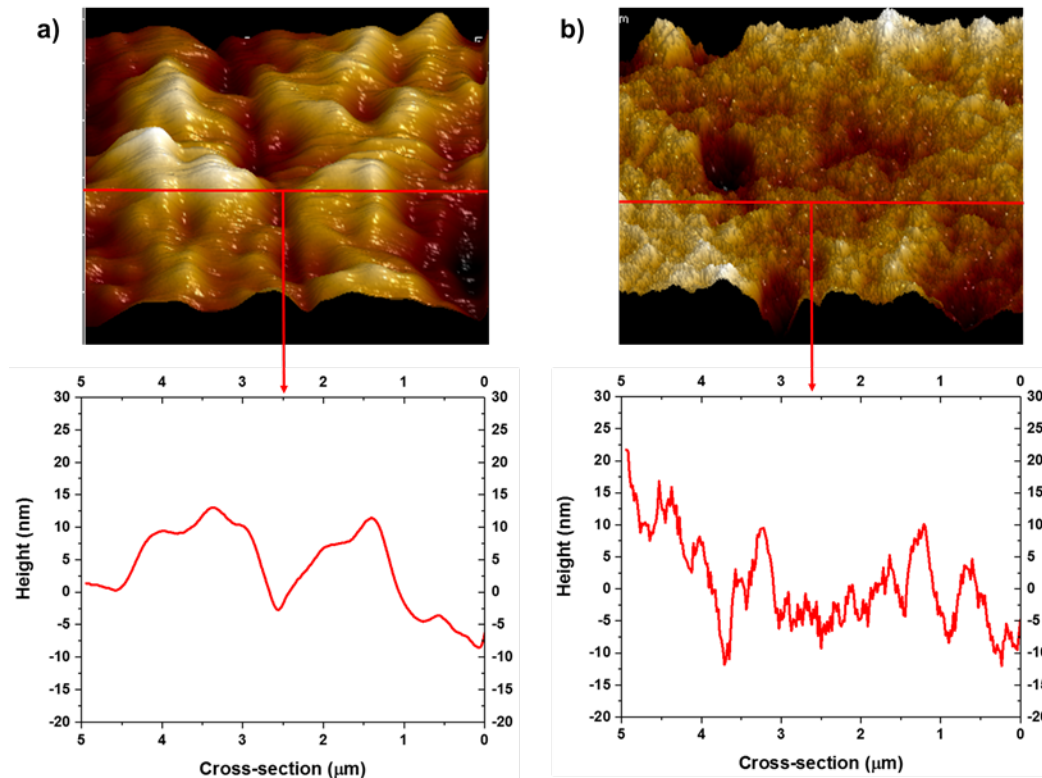
Figure 7-3. AFM images of (a) rSSP films, and (b) nPM-modulated rSSP film, with the corresponding cross-sectional height profiles.

7.5 Conclusion

Hydrophobic silane (nPM) enhanced the surface properties of rSSP-based films by inducing their secondary structures in an aqueous system. Increased hydrophobicity was confirmed, as the water contact angle on the nPM-modulated rSSP film was higher. The increased surface roughness on the silane-modulated films can lead to improving the quality of the rSSP films for various applications, such as adhesion of biological cells on the surface.

7.6 References

1. Lewis, R. V. *Chem. Rev.* **2006**, *106*, 3762.

2. Teule, F.; AdDIson, B.; Cooper, A. R.; Ayon, J.; Henning, R. W.; Benmore, C. J.; Holland, G. P.; Yarger, J. L.; Lewis, R. V. *Biopolymers* **2012**, *97*, 418.

3. An, B.; Jenkins, J. E.; Sampath, S.; Holland, G. P.; Hinman, M.; Yarger, J. L.; Lewis, R. *Biomacromolecules* **2012**, *13*, 3938.

4. Xia, X. X.; Qian, Z.-G.; Ki, C. S.; Park, Y. H.; Kaplan, D. L.; Lee, S. Y. *Proc. Natl. Acad. Sci. U.S.A.* **2010**, *107*, 14059.

5. Holland, G. P.; Creager, M. S.; Jenkins, J. E.; Lewis, R. V.; Yarger, J. L. *J. Am. Chem. Soc.* **2008**, *130*, 9871.

6. Hayashi, C. Y.; Shipley, N. H.; Lewis, R. V. *Int. J. Biol. Macromol.* **1999**, *24*, 271.

7. Minoura, N.; Aiba, S. I.; Gotoh, Y.; Tsukada, M.; Imai, Y. *J. Biomed. Mater. Res.* **1995**, *29*, 1215.

8. Morgan, A. W.; Roskov, K. E.; Lin-Gibson, S.; Kaplan, D. L.; Becker, M. L.; Simon, C. G. Jr. *Biomaterials* **2008**, *29*, 2556.

9. Sofia, S.; McCarthy, M. B.; Gronowicz, G.; Kaplan, D. L. *J. Biomed. Mater. Res.* **2001**, *54*, 139.

10. Baoyong, L.; Jian, Z.; Denglong, C.; Min, L. *Burns* **2010**, *36*, 891.

11. Hijirida, D. H.; Do, K. G.; Michal, C.; Wong, S.; Zax, D.; Jelinski, L. W. *Biophys. J.* **1996**, *71*, 3442.

12. Gomes, S.; Leonor, I. B.; Mano, J. F.; Reis, R. L.; Kaplan, D. L. *Biomaterials* **2011**, *32*, 4255.

13. Teule, F.; Cooper, A. R.; Furin, W. A.; Bittencourt, D.; Rech, E. L.; Brooks, A.; Lewis, R. V. *Nat. Protoc.* **2009**, *4*, 341.

14. Albertson, A. E.; Teule, F.; Weber, W.; Yarger, J. L.; Lewis, R. V. *J. Mech. Behav. Biomed. Mater.* **2014**, *29*, 225.

15. Gomes, S.; Gallego-Llamas, J.; Leonor, I. B.; Mano, J. F.; Reis, R. L.; Kaplan, D. L. *Macromol. Biosci.* **2013**, *13*, 444.

16. Bettinger, C. J.; Bao, Z. *Polym. Int.* **2010**, *59*, 563.

17. Dae-Hyeong Kim, D.; Viventi, J.; Amsden, J. J.; Xiao, J.; Vigeland, L.; Kim, Y.; Blanco, J. A.; Panilaitis, B.; Frechette, E. S.; Contreras, D.; Kaplan, D. L.; Omenetto, F. G.; Huang, K.; Zakin, M. R.; Litt, B.; Rogers, J. A. *Nat. Mater.* **2010**, *9*, 511.

18. Wendt, H.; Hillmer, A.; Reimers, K.; Kuhbier, J. W.; Schafer-Nolte, F.; Allmeling, C.; Kasper, C.; Vogt, P. M. *PLoS One* **2011**, *6*, e21833.

19. Jiang, C.; Wang, X.; Gunawidjaja, R.; Lin, Y. H.; Gupta, M. K.; Kaplan, D. L.; Naik, R. R.; Tsukruk, V. V. *Adv. Funct. Mater.* **2007**, *17*, 2229.

20. Hardy, J. G.; Leal-Egañ a, A.; Scheibel, T. R. *Macromol. Biosci.* **2013**, *13*, 1431.

21. Vendrely, C.; Scheibel, T. *Macromol. Biosci.* **2007**, *7*, 401.

22. Wohlrab, S.; Mueller, S.; Schmidt, A.; Neubauer, S.; Kessler, H.; Leal-Egana, A.; Scheibel, T. *Biomaterials* **2012**, *33*, 6650.

23. Krishnaji, S. T.; Bratzel, G.; Kinahan, M. E.; Kluge, J. A.; Staii, C.; Wong, J. Y.; Buehler, M. J.; Kaplan, D. L. *Adv. Funct. Mater.* **2013**, *23*, 241.

24. Bini, E.; Foo, C. W. P.; Huang, J.; Karageorgiou, V.; Kitchel, B.; Kaplan, D. L. *Biomacromolecules* **2006**, *7*, 3139.

25. Slotta, U.; Tammer, M.; Kremer, F.; Koelsch, P.; Scheibel, T. *Supramol. Chem.* **2006**, *18*, 465.

26. Huemmerich, D.; Slotta, U.; Scheibel, T. *Appl. Phys. A: Mater. Sci. Process.* **2006**, *82*, 219.

27. Krishnaji, S. T.; Huang, W.; Rabotyagova, O.; Kharlampieva, E.; Choi, I.; Tsukruk, V. V.; Naik, R.; Cebe, P.; Kaplan, D. L. *Langmuir* **2011**, *27*, 1000.

28. Hardy, J. G.; Leal-Egañ a, A.; Scheibel, T. R. *Macromol. Biosci.* **2013**, *13*, 1431.

29. Tucker, C. L.; Jones, J. A.; Bringhurst, H. N.; Copeland, C. G.; AdDIson, J. B.; Weber, W. S.; Mou, Q.; Yarger, J. L.; Lewis, R. V. *Biomacromolecules* **2014**, *15*, 3158.

30. Witucki, G. L. *J. Coat. Technol.* **1993**, *65*, 57.

31. Peng, Y.; Turner, N, W.; Britt, D.W. *Colloids Surface B,* **2014**, *119*, 6.

32. Gomes, S.; Numata, K.; Leonor, I. B.; Mano, J. F.; Reis, R. L.; Kaplan, D. L. *Biomacromolecules* **2011**, *12* (5), 1675.

CHAPTER 8

CONCLUSION

This research contributes to the broader understanding of the silane modulation of protein secondary structure and self-assembly for developing nanotherapeutic agents to be used against amyloid-based diseases. The various diseases resulting from protein pathogenesis include such widely known neurological diseases as Alzheimer's, Parkinson's, and ALS, as well as numerous other diseases such as dialysis-related amyloidosis and cataracts. The protein-conformation activity of silanes allows for additional applications in bioprocessing, where they could be applied as artificial chaperones for disaggregation and refolding of recombinant proteins expressed in bacteria and yeast. Multi-level functionality can be imparted in the silane-based NPs, as the present research also shows promise of developing versatile silica-based drug-carrying NPs, which could carry small-molecule therapeutics against amyloid disease in parallel to the activity exhibited by the fluoro-silane nanoparticle carrier.

Toward the development of NP-therapeutics / drug carriers, this research characterized methods to tune the silane sol-gel kinetics under aqueous conditions, to avoid the use of solvents, and to provide a green-chemistry approach to product synthesis. The hydrolysis and condensation study provides detailed understanding of the fluoro- and alkoxysilanes, 3F and nPM, respectively. The formation of monodisperse,

spherical NPs was attainable for 3F, whereas the nPM particles exhibited greater

disparity in size and morphology. The formation of NPs directly from these tri-ethoxy

silanes represents a unique approach to synthesizing functional silane NPs, which

normally proceed via a two-step process in which silica NPs are first created from a tetra-

ethoxy silane precursory (TEOS), followed by surface functionalization with additional

silanes.

Due to the poor solubility of silanes in aqueous solution, established procedures

employ alcohol / water mixtures; however, as shown in this thesis research, an aqueous

synthesis approach can be used by careful selection of pH and silane concentration. The

geometry of the reaction vessel must also be considered, as the silanes form a lens either

at the air / water interface or the bottom of the reaction container for nPM and 3F,

respectively. The ability of the lens to spread and increase the surface area exposed to the

acid solution will influence the hydrolysis reaction rate. Sonication can be employed to

form droplets of silane in the solution, but it does not allow for the in-situ monitoring of

the sol-gel kinetics, as was done here using dynamic light scattering (DLS) and turbidity

scans.

From the hydrolysis and condensation kinetics profiles of 3F and nPM, it was

possible to know exactly when to isolate the polymeric NPs as they evolved for a given

pH, and introduce them to the protein fibrillation reaction, to test their activity. A broader

understanding of the physiological properties of these silane-based NPs is necessary to

optimize their performance toward fibrillation inhibition processes in more complex, e.g. multi-protein, environments.

From the model systems investigated in this research, 3F-based silica NPs showed greater activity against the amyloid fibril inhibition. The research showed that 3F silane chemistry completely inhibited the amyloid formation against the model protein, BLG, as evidenced by an absence of fibrils during AFM imaging. Deconvoluted ATR-FTIR spectra further confirmed the induction of secondary structural motifs in BLG by the NPs. In particular, 3F-BLG interaction reduced β-sheet content as the silane and BLG were heated under conditions that normally induced BLG fibrillation. This reduction of β-sheet content is particularly relevant to amyloid assembly that frequently occurs through self-assembly of protein monomers via exposed β-sheet motifs.

Molecular docking studies further confirmed the interaction between silanol and BLG as mediated by hydrogen bonding, involving an unreacted silanol group as a hydrogen bond donor. The importance of a free silanol moiety in conjunction with the tri-fluoro or methyl groups of 3F and nPM, respectively, highlights the multi-valent interaction of these silanes with the protein, in order to influence the protein secondary structure and fibrillation propensity.

Additional applications of the 3F and nPM particles were also investigated in this thesis. In particular, NP assembly on surfaces to form super-hydrophobic coatings was

demonstrated through water contact angle analysis. NP synthesis in a very facile and environmentally friendly way is an outcome of this research.

In summary, the completed research has demonstrated a unique assembly of tri-functional silanes to form NPs, which is in contrast to the two-step methods commonly employed. This fluoro-functionality, in conjunction with the unreacted silanol group, interacted through hydrogen bonding with BLG, inhibiting its fibrillation. In contrast, the alkyl-presenting silane NPs did not demonstrate significant anti-fibrillation activity. Ongoing work is investigating the generality of this NP-protein interaction. Loading of these silica NPs with additional small-molecule therapeutics is feasible, as was demonstrated using curcumin and quercetin, thus providing a multi-functional NP that has inherent biological activity and ability to deliver and release additional therapies. Surface modification with the NPs is a final application to construct superhydrophobic coatings.

Our extended study on the applications of the fluorinated and methylated polymeric NPs against the spider silk protein produced enhanced characteristics of their films. Our study also showed that these polymeric particles can create new nanocomposites of silica-spider silk protein, which have potential in biomaterials applications where the silane not only imparts hydrophobic character to the resulting composite, but also tunes the secondary structure of the resulting composite. Future work

will explore methods to optimize bulk mechanical properties as well as the observed surface property changes reported here.

From the engineering perspective, this research offers several engineering aspects:

1. Downstream processing applications, such as disaggregation of recombinant spider silk proteins that overexpressed and form inclusion bodies.

2. Materials science applications as superhydrophobic nanoparticle surface modifying agents.

3. Nanocomposite materials: hybrid silica-protein structures are formed that may exhibit unique biological activity.

4. The one-step aqueous synthesis process is an economically and environmentally viable approach to scaling this technology for superhydrophobic nanoparticle production.

CHAPTER 9

FUTURE WORK

AMYLOID FIBRILS-MESOPOROUS SILICA-BASED HYBRID MEMBRANE FOR

PURIFYING ARSENIC-CONTAMINATED WATER

Introduction

Arsenic is one of the most harmful water pollutants and a major environmental

concern. Dissolved arsenic in ground water affects the health of millions of people all

around the world. (1-2) The human body gets exposed to arsenic through consumption of

contaminated water, which leads to arsenicosis. (3) In natural ground water and surface

water, arsenic is found as neutrally charged arsenite (As (III)) and negatively charged

arsenate (As (V)) oxyanions, depending on pH, redox potential (Eh), and existence of

other chemical species. (4) Several technologies have been explored for removing arsenic

from contaminated water, such as oxidation / precipitation, (5) coagulation, (6)

membrane, (7, 8) ion- exchange, (9, 10) and sorbent technologies. (11-13) A recent study

showed that low-cost milk protein β-lactoglobulin (BLG)-based amyloid fibrils are

highly efficient against arsenic species, along with various heavy metal ions and nuclear

wastes, where amyloid fibrils interact with water pollutants via strong supramolecular metal-ligand bonding. (14) The major challenges to use the BLG amyloid fibrils in the water-purifying membrane are their water-impervious characteristics. One way to overcome this issue is to create a porous amyloid fibril-based hybrid membrane system, through which the targeted aqueous media can easily pass. In general, incorporation of amyloid fibrils with porous hydrophilic materials to create a hybrid membrane will be an ideal system for addressing this issue.

In a hybrid membrane system, efficiency of these fibrils to interact with the target pollutants in the water system will depend on their exposed surface area. Tuning the right amount of fibrils with appropriate hydrophilic porous materials can provide the optimum available reactive surface area for pollutants to interact with amino acids of the protein. A comprehensive study on developing a hybrid membrane system by integrating various types of amyloid fibrils and suitable support materials could lead to creating a highly efficient membrane for purifying contaminated water.

Mesoporous silica particles (MSP) are widely used for various purposes such as supports for adsorption, catalysis, chemical separations, biotechnology devices, carrier for drugs, and components in nanocomposite materials, due to their chemical and thermal stability and easy functionalization properties. (15-20) In the last few years, we have investigated the formation of the amyloid fibrils of different proteins such as BLG, lysozyme (LYS), and spider silk protein (SSP), using conventional heating systems and

microwave system. We also have investigated the interaction of silica-based NPs with the amyloid fibrils, and formation of composite materials, which we have presented at several national and regional conferences. (21-24) Our findings suggest that highly efficient hybrid membrane systems can be achieved by incorporating amyloid fibrils with silica-based particles, which could be used to remove the pollutants from contaminated water.

In a hydrophilic MSP and amyloid fibril hybrid membrane system, the particle surface properties control the curvature of the amyloid fibrils attached on it, which eventually determines the availability of the fibrils to the targeted pollutants. Here, we are proposing an experimental investigation of developing hybrid membrane systems by incorporating amyloid fibrils and MSP, and use them to purify arsenic-contaminated water.

Amyloid fibrils bond with water pollutants like arsenic through the amino acids present in the associated protein monomer. The amino acid number and type in the used protein will dictate the pollutant-fibril interactions. Since BLG, LYS, and SSP all consist of different types and numbers of amino acids, their fibrils should behave distinctively on bonding with arsenic species. These proteins are distinct in their surface charges at neutral pH, which also could affect their interaction with the silica particles. Therefore, the protein types and the surface charge of the silica particles (SP) will decide the success

of the hybrid membrane formation and their efficiency to remove pollutants like arsenic. Objectives of the proposed research are:

1. To develop a hybrid composite membrane using negatively charged MSP and amyloid fibrils of three types of protein such as BLG, LYS, and SSP having negative, positive, and negative surface charges on their surfaces respectively at neutral pH

2. Use these hybrid membranes to investigate their efficiency to remove the arsenic species (As (III) and As (V)) from the contaminated water.

Experimental method

Amyloid fibril formation

BLG and LYS will be fibrillated in an acidic aqueous system (pH 2.0) by heating at 90°C for 5 h for BLG and 60°C for 5 h for LYS in glass vials. For SSP, fibrillation will be performed using microwave pulse technique, where SSP will be dissolved and fibrillated in aqueous media at neutral pH by microwaving samples in tightly closed glass vials for 10 seconds, which will increase the temperature up to 130°C, and then resting for 1 min; then again 10 seconds of microwaving; and this cycle will be repeated 5 times. The fibrillation process will be stopped using an ice bath. AFM will be used to confirm the fibril formation. Figure 9-1 shows the schematic of the fibril formation of different proteins.
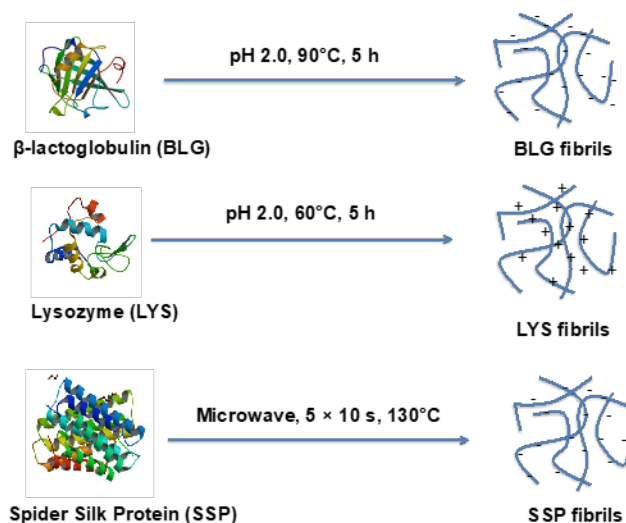
Figure 9-1. Schematic of the fibril formation process of BLG, LYS, and SSP.

MSP synthesis

MSP will be synthesized following a modified Stöber method, as described in

Figure 9-2. Appropriate mole ratio of ETOH, water, CTAB

(Cetyltrimethylammonium bromide), and TEOS (Tetraethylorthosilicate) will be heated

at 80°C together for 2 h, to generate silica particles with CTAB integrated inside. After

centrifugation, the silica particles will be washed with ETOH, and then CTAB will be

removed by adding a HCl and ETOH mix solution and heating at 60°C for 6 h. Thus, we

will obtain negatively charged MSP, which we will collect after centrifugation and

ETOH wash. To achieve positively charged MSP, we will add APTES ((3-Aminopropyl)

triethoxysilane) in the negatively charged MSP in ETOH solution; and heating at 80°C

for 12 h will give us positively charged MSP. After centrifugation and ETOH wash, we

will obtain MSP, and SEM images will be taken to confirm the sizes and porosities of the
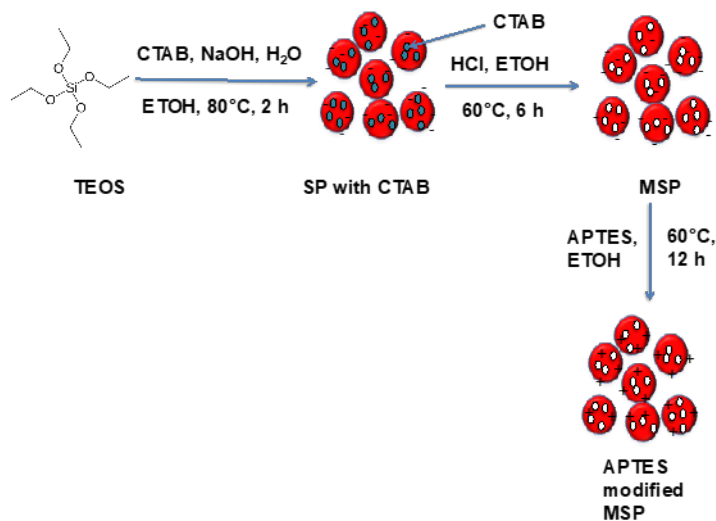
overnight freeze-dried samples.

Figure 9-2. Synthesis of MSP.

Interacting MSP with amyloid fibrils

Dried MSP with three different sizes from two types will be added to the amyloid

fibrils of BLG, LYS, and SSP protein-containing solutions, as shown in Figure 9-3.

Depending on the surface properties and size of the fibrils and MSP, the interaction will
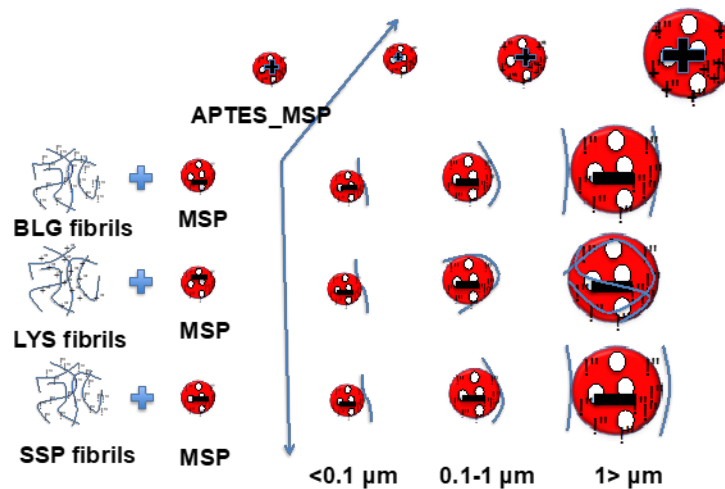
vary.

Figure 9-3. Schematic of the possible interactions of amyloid fibril and MSP.

These mixed solutions of MSP and amyloid fibrils will be passed through a cellulose filter using vacuum filtration. (Figure 9-4) This cellulose filter will hold the hybrid membrane consisting of amyloid fibrils and MSP.
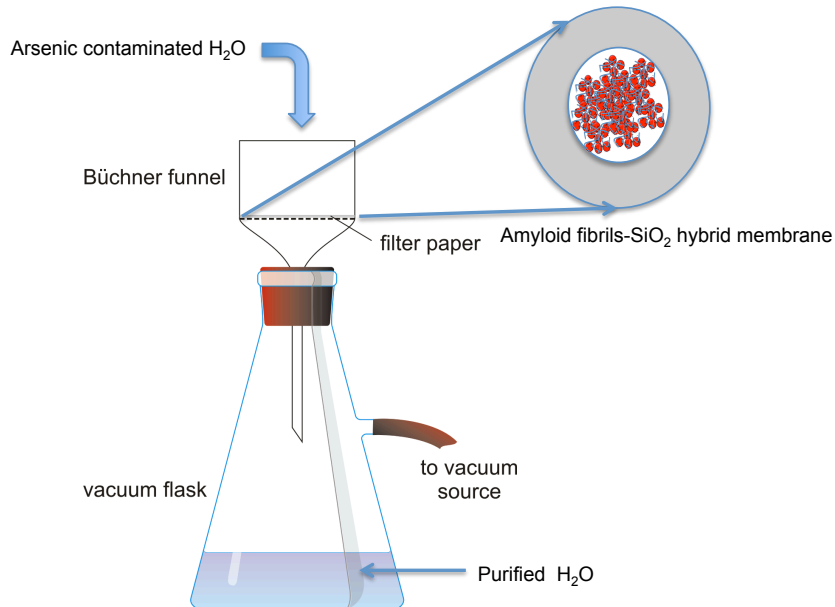
Figure 9-4. Water purification using hybrid membranes in a vacuum filter system.

Purification of arsenic-contaminated water

In the final step, pollutant water containing As (III) and As (V) will be passed through the hybrid membranes, using a vacuum pump, so the arsenic gets trapped in the membrane system, and purified water is stored in the flask. (Figure 9-4) The quantity of the As (III) and As (V) amount in the aqueous system will be measured using AAS (atomic adsorption spectroscopy).

Expected results

We have already generated amyloid fibrils of BLG, LYS, and SSP. In Figure 9-5, an AFM image shows the BLG-based amyloid fibrils with different sizes ranging from <1

µm to >5 µm. We have also synthesized silica-based particles, as shown in Figure 9-6, where an SEM image shows the silica particles with different sizes, ranging from 0.1 µm to 0.5 µm.
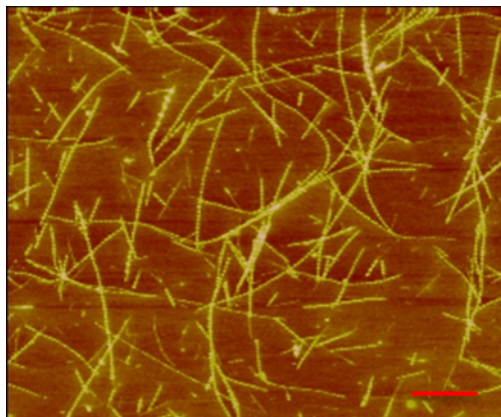

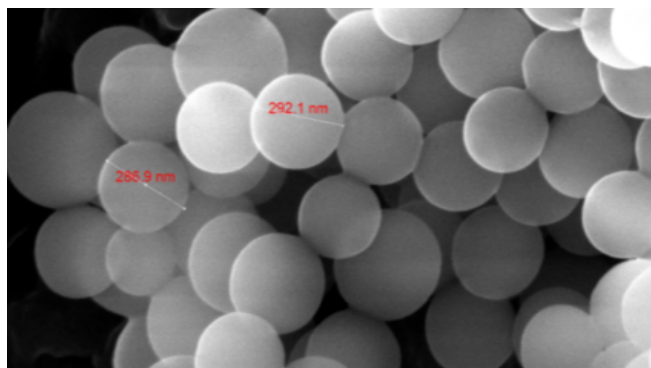Figure 9-5. AFM image of amyloid fibrils of BLG (bar is 2μm).

Figure 9-6. SEM image of silica particles.

Following the conventional Stöber method, MSP with different sizes will be synthesized. Incorporating amyloid fibrils and these MSPs will give us the optimum

hybrid membrane system, where arsenic-contaminated water will be purified. In this hybrid membrane system, we are expecting both As (III) and As (V) to be removed below 10 ppb in the purified aqueous body. Along with As (III) and As (V), other common water pollutants such as chromium, phosphates, etc. will also be removed from the contaminated water, to establish the efficiency of our developed membrane system.

References

1. Smedley, P. L.; Kinniburgh, D. G. *Appl. Geochem.* **2002**, *17*, 517.

2. Karim, M. *Water Res.* **2000**, *34*, 304.

3. Jain, C. K.; Ali, I. *Water Res.* **2000**, *34*, 4304.

4. Ferguson, J. F.; Gavis, J. *Water Res.* **1972**, *6*, 1259.

5. Lihua, S.; Ruiping, L.; Shengji, X.; Yanling, Y.; Guibai, L. *Desalination* **2009**, *243*, 122.

6. Balasubramanian, N.; Kojima, T.; Srinivasakannan, C. *Chem. Eng. J.* **2009**, *155*, 76.

7. Waypa, J.; Elimelech, M.; Hering, *J. Am. Water Works Assoc.* **1997**, *89*, 102.

8. Iqbal, J.; Kim, H.; Yang, J.; Baek, K.; Yang, J. *Chemosphere* **2007**, *66*, 970.

9. An, B.; Steinwinder, T. R.; Zhao, D. *Water Res.* **2005**, *39*, 4993.

10. Kim, J.; Benjamin, M. M. *Water Res.* **2004**, *38*, 2053.

11. Cumbal, L.; SenGupta, A. K. *Environ. Sci. Technol.* **2005**, *39*, 6508.

12. Kanel, S. R.; Manning, B.; Laurent Charlet, L.; Choi, H. *Environ. Sci. Technol.* **2005**, *39* (5), 1291.

13. Kanel, K. R.; Grenèche, J.; Choi, H. *Environ. Sci. Technol.* **2006**, *40* (6), 2045.

14. Bolisetty, S.; Mezzenga, R. *Nat. Nanotechnology* **2016**, *11* (4), 365.

15. Corma, A. *Chem. Rev.* **1997**, *97*, 2373.

16. Sayari, A; HamouDI, S. *Chem. Mater.* **2001**, *13*, 3151.

17. Ying, J. Y.; Mehnert, C. P.; Michael S.; Wong, M. S. *Chem., Int. Ed.* **1999**, *38*, 56.

18. Liu, X.; Li, J.; Zhou, L.; Huang, D.; Zhou, Y. *Chem. Phys. Lett.* **2005**, *415*, 198.

19. Grün, M.; Kurganov, A. A.; Schacht, S.; Schüth, F.; Unger, K. K. *J. Chromatogr. A* **1996**, *740*, 1.

20. Raja, R.; Thomas, J. M. *J. Mol. Catal. A: Chem.* **2002**, *181*, 3.

21. GiasudDIn A. B. M.; David W Britt, D. W. "Inhibition of amyloid fibrillation of β-Lactoglobulin by hydrolyzed hydrophobic alkoxy- and fluoro- silanes", *251th ACS meeting and exposition*, June, 2016.

22. GiasudDIn A. B. M.; David W Britt, D. W. "Amyloid fibrillation inhibition by hydrolyzed alkyl- and fluoro-silane monomers", *UBEC 2016, 11th Annual Utah Bioengineering Conference*, December, 2016.

23. GiasudDIn A. B. M.; David W Britt, D. W. "One-pot aqueous synthesis of hydrophobic silica nanoparticles for non-polar small molecule delivery", *UBEC 2016, 11th Annual Utah Bioengineering Conference*, December, 2016.

24. GiasudDIn A. B. M.; Harris, T. I.; Lewis, R. V.; Britt, D. W. "Aqueous synthesis of silica-spider silk nano-composite materials" *IBE Annual Meeting*, March, 2017

25. GiasudDIn, A. B. M.; Kanel, S. R.; Choi, H. *Environ. Sci. Technol.* **2007**, *41* (6), 2022.

ABUL BASHAR MOHAMMAD GIASUDDIN

Utah State University, 4105 Old Mail Hill. Logan, UT 84322-4105

Contact: shameematuga@gmail.com, Phone: (435) 709-8432

Education:

Ph.D. Biological Engineering, Utah State University, USA

M.Sc. Environmental Engineering, University of Georgia, USA

M.Sc. Environmental Science & Engineering, GIST, South Korea

B.Sc. Civil Engineering, BUET, Bangladesh

Peer reviewed publication:

GiasudDIn, A.B.M., Kanel, S.R. and Choi, H., Adsorption of Humic Acid onto Nanoscale Zerovalent Iron and its Effect on Arsenic Removal, **Environ. Sci. Technol.** 2007; 41(6); 2022-2027

Patents:

GiasudDIn, A.B.M., Kanel, S.R., Choi, H, Method of synthesizing air-stable zero-valent iron nanoparticles at room temperature and application. USPTO Patent Application 2008009105; 04-17-2008

Conferences and proceeDIngs:

1. **GiasudDIn, A.B.M.,** and Britt, D. W., Inhibition of amyloid fibrillation of β-Lactoglobulin by hydrolyzed hydrophobic alkoxy- and fluoro- silanes. **251st ACS National Meeting**, San DIego, CA, 2016

2. **GiasudDIn, A.B.M.,** and Britt, D. W., Evolution of polymeric nanoparticles formation during condensation of hydrophobic alkoxysilanes in an organic solvent free sol-gel method. **250th ACS National Meeting**, Boston, MA, 2015

3. **GiasudDIn, A.B.M.,** Locklin, J., Ray, C., Aggregation behavior of water soluble CdSe Quantum Dots in aquatic system, DIvision of Colloid & Surface Chemistry, **237th ACS National Meeting,** Salt Lake City, UT, 2009

4. **GiasudDIn, A.B.M.,** Kanel, S. R., Locklin, J., Ray, C., Removal of methyl parathion using Iron Nanoparticles. **236th ACS National Meeting**, Philadelphia, PA, 2008 (Travel Grant Award)

Honors and awards:

1. Technology fellowship for undergraduate study (1998-2002)

2. Korea Government Fellowship (KRF) (2004- 2006)

3. Engineering Graduate Assistantship (UGA) (2007-2011)

4. Graduate Assistantship (USU) (2012-2017)

Research skills:

1. Protein-nanoparticles interactions

2. Organic, inorganic nanoparticles synthesis

3. Surface characterization of micro and nano structures

4. Water treatment using nanoparticles

5. Algae based water treatment

Instruments and techniques:

AFM, SEM, ATR-FTIR, DLS, Zeta potential, Atomic absorption spectroscopy (AAS), UV-vis, HPLC, IC, Fluoro-spectroscopy, Turbiscan LAB, TGA

Computer and software:

OriginPro, SigmaPlot, Microsoft Word, R Statistical Software, MATLAB, SolidWorks, AutoDock